7-15-2019

The Dynamic Roles of Red Blood Cell in Microcirculation

Sitong Zhou
sz4796@rit.edu

Recommended Citation

Zhou, Sitong, "The Dynamic Roles of Red Blood Cell in Microcirculation" (2019). Thesis. Rochester Institute of Technology. Accessed from

R·I·T

The Dynamic Roles of Red Blood Cell in Microcirculation

by

Sitong Zhou

A dissertation submitted in partial fulfillment of the requirements
for the degree of Doctorate of Philosophy in Microsystems Engineering

Microsystems Engineering Program
Kate Gleason College of Engineering

Rochester Institute of Technology
Rochester, New York
July 15th, 2019

The Dynamic Roles of Red Blood Cell in Microcirculation
by
Sitong Zhou

Committee Approval:

We, the undersigned committee members, certify that we have advised and/or supervised the candidate on the work described in this dissertation. We further certify that we have reviewed the dissertation manuscript and approve it in partial fulfillment of the requirements of the degree of Doctor of Philosophy in Microsystems Engineering.

Dr. Jiandi Wan Date
Assistant Professor, Chemical Engineering

Dr. Steven W. Day Date
Associate Professor, Biomedical Engineering

Dr. Michael Schrlau Date
Associate Professor, Mechanical Engineering

Dr. Blanca Lapizco-Encinas Date
Associate Professor, Biomedical Engineering

Certified by:

Dr. Bruce Smith Date
Director, Microsystems Engineering Program

ABSTRACT

Kate Gleason College of Engineering
Rochester Institute of Technology

Degree: Doctor of Philosophy **Program**: Microsystems Engineering

Authors Name: Sitong Zhou

Advisors Name: Jiandi Wan

Dissertation Title: The Dynamic Roles of Red Blood Cell in Microcirculation

Erythrocytes (otherwise known as red blood cells (RBCs)), are the most common cell type in the body. They are responsible for oxygen (O_2) transportation as well as carbon dioxide (CO_2) exchange. Different from most cells, red cells have no nuclei in mammals due to the enucleation during the maturation. The structure of erythrocytes was shown to have a phospholipid bilayer membrane, membrane proteins and cell skeleton. It provides the stability that RBCs need for the circulation in the body systems. Also, this well-established structure makes it possible for them to accomplish ion and gas exchange, which therefore keeps the osmolality and pressure stable for extracellular and intracellular environment. Although a great variety of red cell characteristics have been investigated, the mechanism and kinetics of RBCs under certain environmental stimulation have not been well studied. In this work, we studied the development of cell membrane by testing the deformability change of erythrocytes during maturation. With the design of our microfluidic channels in *ex vivo* experiments, we then learned that RBC can work not only as O_2 transporter but also as oxygen sensor itself. When oxygen level decrease, TBC membrane becomes softer and leads to blood flow increase eventually. We then investigated the mechanism of RBC membrane change on a molecular level to study the mechanism of RBC deformability change under hypoxia. We matched our findings in both *in vivo* and *ex vivo* experiments. Via *in vivo* experiments, we could even connect cerebral circulation to neuroactivity. Furthermore, the behavior of RBCs under hypoxia and in shear flow, such as the ATP release, was studied as well via *ex vivo* experiments. In the study, we focused on the mechanosensitive channel Piezo1 on RBC membrane and found the connection between this ion channel and RBC ATP release.

Acknowledgement

To my late grandfather, Guiheng Na, who had always been there through good and bad times with his caring heart. Thank you and I miss you every moment.

To my wonderful parents, Zhengzheng Zhou and Meiling Na, thanks for being my world, thanks for guiding me, thanks for comforting me, thanks for trying your best to support and understand me. I love you.

I would like to thank my Microsystems Engineering Program at RIT, especially Dr. Bruce Smith and Lisa Zimmerman for all the help and support. Thanks to my amazing lab mates and my mentor, Dr. Jiandi Wan, without you these five years would have been much more difficult. Great thanks to Jim DeCourcey and Mike Giannetto for being the world's best helpers, you make our work not only efficient but also fun and exciting.

I would also like to acknowledge our collaborators from University of Rochester, Purdue University, Scripps Research Institute and Johns Hopkins University. Special thanks to Dr. Maiken Nedergaard from U of R for giving me the opportunity to learn about the amazing *in vivo* experiments. I was also really lucky to learn from Wei Song and Ning Kang to do all the fantastic surgeries.

Thanks to all my friends and families for tolerating me when I was being ridiculous, for being patient with me and constantly cheering me on. I want to give a shout-out to Sean Corcoran, Paige Buchholz and Zach Buchholz, thanks for taking the cross-country road trip with me. Because of you, I can be brave and courageous to start the new chapter at University of California, Davis.

Thanks to everyone for ever being part of my colorful life, including my goofiest dog, Polymer.

Thank you, for making Rochester, NY my home away from home.

CONTENTS

1. INTRODUCTION

1.1. Maturation and circulation of erythrocytes

RBCs comprise the most common cell type in the body transporting oxygen and carbon dioxide [1-3]. It was recognized that mature RBCs in mammals do not contain nucleus [1]. Research has shown the presence of two distinct populations of erythrocytes, primitive and definitive [2]. Figure 1-1 shows the overview of both primitive and definitive erythropoiesis [1], in which orthochromatic erythroblasts (OrthoE) enucleate to form a pyrenocyte that containing a condensed nucleus. After enucleation, it develops into a reticulocyte (Retic), which eventually matures into an RBC.

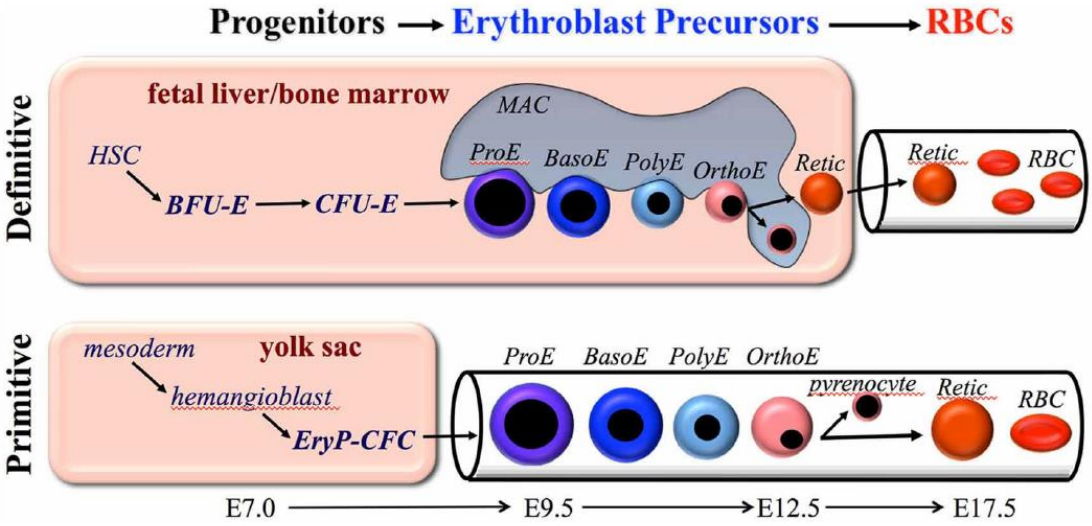

Figure 1-1. Scheme of development of primitive and definitive erythropoiesis. The first blood cells in mammalian emerge within yolk sac, as known as primitive erythroblasts, while definitive cells occur in fetal live as well as postnatal bone marrow. [1]

Unlike the definitive erythropoiesis, which is observed in the fetal liver and the postnatal bone marrow, primitive erythroblasts are only found in the embryo [4-6], which are essential to the regeneration of erythrocytes and fetal development. The primitive erythroid lineage arises in the yolk sac, and pools of immature erythroblasts in "blood islands" are first apparent at the embryonic day of 7.25–7.5 (which is marked as E7.0–7.5) [4]. The number of primitive erythroid cells increases significantly within a vascular plexus at E8.0 [4, 7]. Different from definitive cells that enter the circulation after maturation, these large, immature, nucleated primitive cells move into the distal region of yolk sac and enter circulation beginning at E8.25, with the onset of cardiac contractions [3-10]. Primitive erythroblasts experience shear stresses in the fetal bloodstream as they travel through the embryonic microvasculature that has a diameter from 4 μm to 60 μm [11]. With the ability to squeeze through capillaries, the structure, composition and deformability of the cytoskeletal network in erythrocytes are well established.

1.2. Structure of RBC membrane and cytoskeleton

Mature RBC is biconcave-shaped, it composes of three major structural elements: lipid bilayer, integral proteins and cytoskeleton [12]. The lipid bilayer is primarily composed of phospholipids and cholesterol with permeability barrier for external environment and red cell cytoplasm exchange. It comprises about 50 to 60% mass of red blood cells, and phospholipids and cholesterol are almost equal amount [12]. The integral proteins are embedded in the membrane. RBC membrane proteins can be classified into transmembrane and peripheral proteins [13]. Common transmembrane proteins include glycoprotein band 3, glycophorins, and protein 4.2 and so on. And there are peripheral membrane proteins including spectrin and ankyrin, etc. [12].

The RBC membrane skeleton is on the inner side of the cell membrane and it provides the structural integrity to the cell. The major components include spectrin, actin, ankyrin, and protein 4.1, etc. Spectrin is the most abundant in RBC membrane skeleton, consisting two subunits, α and β [12]. Together with erythrocyte membrane, the proteins and cytoskeleton provide the unique deformability and stability of red blood cells [12].

1.3. Blood flow dynamics

Fluid comes from Latin word meaning “to flow”. A fluid is usually defined as a substance that can flow, such as gas and liquid [14]. Besides pressure, density and temperature, etc., viscosity is one of the most important variables that characterizes specific fluid mechanical behavior. Viscosity is defined as the quantitative measure of a fluid’s resistance to flow [14]. For some common fluids as water or oil, there is a linear relation between the shear stress applied and resulting strain rate, as shown in Figure 1-2 [14]:

$$\tau \propto \frac{\delta\theta}{\delta t} \tag{1}$$

For Newtonian fluid, the viscosity remains constant under certain temperature and it has nothing to do with the applied shear stress, which follows the equation:

$$\tau = \mu \frac{d\theta}{dt} \tag{2}$$

in which μ is the viscosity coefficient [14] (Figure 1-3). On the contrary, if the viscosity of the fluid changes over different applied shear stress, the fluid is then called non-Newtonian fluid.

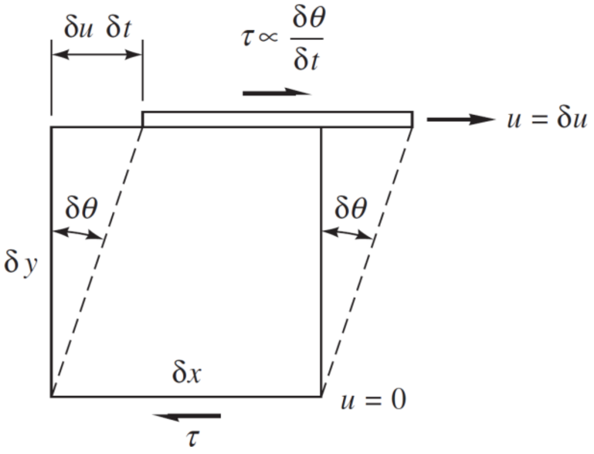

Figure 1-2. Shear stress causes continuous shear deformation in a fluid with a shear rate at *δθ/δ*t. [14]

For the fluids with viscosities that increase with increasing strain rate, they are classified as shear-thickening fluids, which is also named *dilatant* [14]. On the contrary, shear-thinning fluid, however, has less resistance while the shear rate increases. It is called *pseudoplastic* [14]. Blood is known as pseudoplastic (shear-thinning) fluid, and the viscosity of normal whole blood as a function of shear strain rate has been previously investigated (Figure 1-4) [15]. Noted that in Cho's study [15], all the measurements were conducted when hematocrit was in the range of 33% to 45%. Figure 1-4 [15] summarized the experimental results from different work with different symbols, while the lines were the predictions from a numerical simulation of various models [15]. From Figure 1-4 we can tell that within a great range of shear rate change, blood viscosity decreases when shear rate is getting higher.

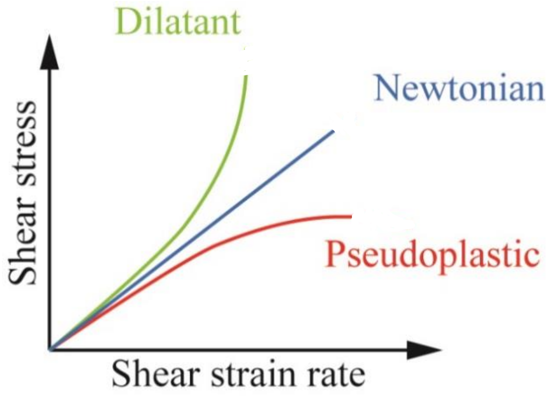

Figure 1-3. Relationship between shear stress and shear strain rate for both Newtonian (blue line) fluids (viscosity is constant at same temperature and pressure, when applied shear changes) and non-Newtonian fluids (viscosity changes when shear rate varies). Red line shows pseudoplastic fluid with decreasing viscosity when shear strain rate is higher. Contrarily, dilatant fluid's viscosity increases with increasing shear strain rate (in green).

It was also shown that whole blood viscosity can be affected by a lot of factors including hematocrit, male or female, temperature, cholesterol level, and even smoking status, etc. [15]. Hematocrit has been shown to be the factor of changing blood viscosity.

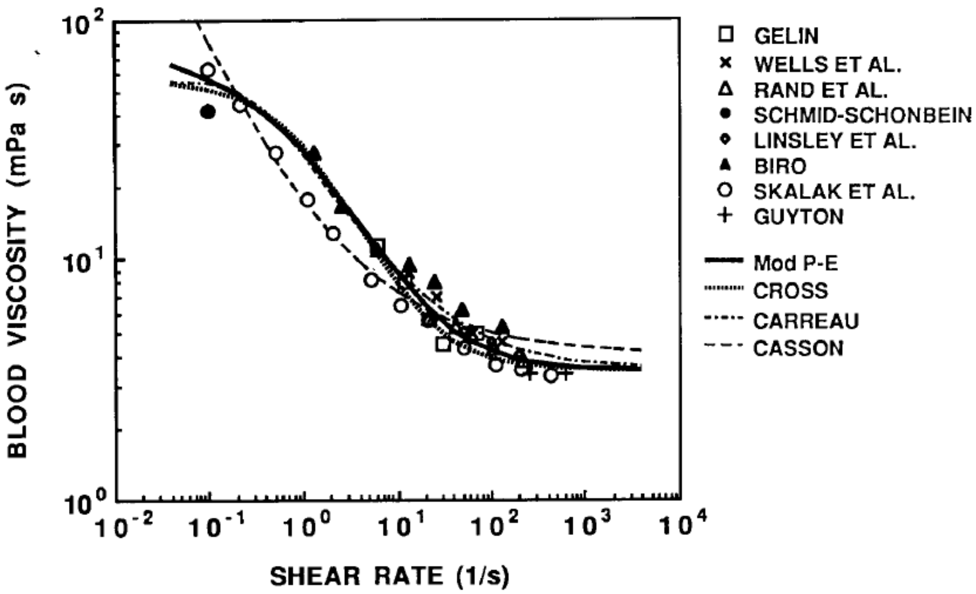

Figure 1-4. Blood viscosity changes over the change of shear rate. Hematocrit was in the range of 33% to 45% for all the measurements. All the symbols represented the viscosity data measured experimentally by different studies, while the dashed lines and solid lines showed the predictions from different models. [15]

Generally, the higher hematocrit would end with greater blood viscosity, and the relationship can be expressed by the polynomial equation

$$\eta = 1.4175 + 5.878H - 15.98H^2 + 31.964H^3 \tag{3}$$

in which η is the viscosity of blood in Poise, while H is the hematocrit (%) divided by 100 [15]. And normally blood hematocrit is about 40%.

Due to the large surface-to-volume ratio of RBCs, they have high stretch ability and also it was investigated that the membrane of erythrocytes can have tank tread-like motion in shear flow [16-18]. With the elasticity of cell membrane and the tank treading motion of RBCs, deformability is a critical characteristic of RBCs and it involves a variety of physiological process, such as cation transport [19], ATP release [20, 21], etc. Among all the functions, oxygen transportation of RBCs [22, 23] is most known with oxygen binding with hemoglobin (Hb) inside erythrocytes. RBC is the major supplier of oxygen, delivering oxygen from lungs to all the tissues in the body.

1.4. Goals, tasks and content of work

In this study, the dynamic roles of RBCs in microcirculation was investigated in multiple perspectives.

Object 1 Role of RBC in cerebral circulation in the process of functional hyperemia: *In vivo* and *ex vivo* experiments were performed to verify that RBC played an important role in regulating blood flow velocity when oxygen level changed. It was found that RBC can not only work as O_2 transporter but also O_2 sensor as they became more deformable under hypoxia.

Object 2 Assessment of the mechanism of how O_2 mediated RBC membrane deformability: To study erythrocyte response under hypoxia, RBCs from transgenic mice were used to study the process of RBC membrane modification under hypoxic condition. With both *in vivo* and *ex vivo* experiments, it can be demonstrated that the membrane protein interactions were the key of how RBCs became more deformable when O_2 decreased.

Object 3 Evaluation of the role of mechanosensitive channel Piezo1 on ATP release from RBCs: to study the behavior of RBC under hypoxia and in shear flow, we focused on ATP release from RBC. Since ion channel Piezo1 was known to be activated under shear stress, *ex vivo* experiments were conducted to investigate how Piezo1 can affect ATP release by regulating calcium influx in RBCs.

Object 4 Investigation of the importance of maturation stage to RBC membrane deformability: To understand the importance of certain cell membrane protein development, RBC deformability at different maturation stages was tested via *ex vivo* experiments to provide further understanding of the role of RBC in microcirculation in the embryo stage.

2. ERYTHROCYTES ARE OXYGEN-SENSING REGULATORS OF THE CEREBRAL MICROCIRCULATION

Energy production in the brain depends almost exclusively on oxidative metabolism. Neurons have small energy reserves and require a continuous supply of oxygen (O_2). It is therefore not surprising that one of the hallmarks of normal brain function is the tight coupling between cerebral blood flow and neuronal activity. Since capillaries are embedded in the O_2-consuming neuropil, we here examined whether activity-dependent dips in O_2 tension drive capillary hyperemia. *In vivo* analyses showed that transient dips in tissue O_2 tension elicit capillary hyperemia. *Ex vivo* experiments revealed that RBCs themselves act as O_2 sensors that autonomously regulate their own deformability and thereby flow velocity through capillaries in response to physiological decreases in O_2 tension. This observation has broad implications for understanding how local changes in blood flow are coupled to synaptic transmission.

2.1. Introduction

Neurovascular coupling involves synaptic activity linking to local changes in cerebral blood flow [24, 25]. The mechanisms by which neural activity triggers hyperemia have been extensively studied because neurovascular coupling forms the basis for functional brain imaging. In addition, defects in neurovascular coupling may contribute to cognitive decline in neurodegenerative diseases, such as Alzheimer disease, as well as in hypertension and stroke [26].

Functional hyperemia can be mediated by a number of compounds, many of which are byproducts of neural activity, including adenosine, nitric oxide (NO), potassium ions (K^+), and carbon dioxide (CO_2) [24]. In addition, functional hyperemia is preceded by a transient decrease in tissue oxygenation [27-29]. Since recent reports have documented that functional hyperemia is initiated in micro vessels embedded in the O_2-consuming neuropil. The present study investigated whether RBCs can work as O_2 sensor and whether the initial dip in tissue O_2 tension drives brain capillary hyperemia. [30]

2.2. Experimental methods

2.2.1. Animals and surgical preparation

C57BL6 mice (25–30 g, 8–12 weeks old, The Jackson Laboratory) of either sex were utilized. Mice were prepared for *in vivo* imaging as described previously [31-34]. All experimental procedures were approved by the University Committee on Animal Resources at the University of Rochester and effort was taken to minimize the number of animals used. Anesthesia was induced in experimental animals with 3.0% isoflurane in room air and maintained at 1.5-2.0% during surgical preparation. Depth of anesthesia was monitored by toe-pinch, or blood pressure. Body temperature was maintained by a water perfused thermal pad (Gaymar T/Pump) set at 37°C. A custom-made metal plate was glued to the skull and a 2-3 mm diameter cranial window was made over the hindlimb cortex for imaging (stereotaxic coordinates: 0.5–3 mm lateral; −1.5 to +1 mm anterior of bregma). Agarose (0.8% in artificial CSF (aCSF), 37˚C) was applied and a glass coverslip was sealed to the metal plate [31, 33]. In hindlimb stimulation experiments, mice were intubated and mechanically ventilated with a small animal ventilator (SAAR-830) in series with an isoflurane vaporizer, and a femoral artery was cannulated for blood gas and blood pressure measurements. Blood gas parameters were maintained within physiologic limits for all experiments. In habituated mice that were allowed to awaken after surgery and prior to imaging, only a cranial window was prepared [32, 34].

2.2.2. Physiological manipulation

In hindlimb stimulation experiments, anesthesia was reduced to 1% isoflurane immediately prior to experimentation. Blood pressure was continuously monitored to assess depth of anesthesia. Hindlimb stimulation was delivered using 2 ms square-wave pulses at an intensity of 0.5-1.0 mA (ISO-flex, A.M.P.I.) in a 2 s 10 Hz train, controlled by a Master-8 and captured with Clampex 9.0 [35]. Stimulus intensity was titrated in each animal to avoid increases in mean arterial blood pressure in response to sensory stimulation.

In O_2 scavenging experiments, 0.001-1.0 M sodium sulfite was dissolved in water containing 100 μM Alexa Fluor 594, loaded into glass micropipettes with tip diameters of

2-3 μm, and puffed onto vessels for 100 ms at 10 psi, controlled by a Picospritzer III. In the O_2 scavenging experiments, mice were habituated to restraint tubes prior to the experiment and allowed to awaken from anesthesia before experimental manipulations [32, 34].

2.2.3. Microfluidic device and RBC imaging

Microfluidic chips were fabricated with polydimethylsiloxane (PDMS) using standard soft photolithography techniques [17, 36, 37]. The widths of the introduction and constriction segments of the capillary channel were 78 μm and 5 μm (Figure 2-2A), respectively. The channel height was 7 μm as measured with a surface profilometer (KLA Tencor P2). The microfluidic device was connected via a short polyethylene (PE 20) tube to an RBC reservoir where a constant pressure (1.6 psi) was applied by using a gas regulator (Omega, DPG1001B) with a precision of 0.1 psi.

To colorimetrically quantify the O_2 partial pressure (PO_2) in the capillary channel, 25 μM of tris(2,2'-bipyridyl)dichlororuthenium(II) hexahydrate (Sigma-Aldrich) was prepared in N_2-bubbled or air-saturated deionized (DI) water. The dye solution was injected into the microfluidic device, which was immersed in a customized glass chamber filled with H_2O or sulfite solution.

To create an O_2 sink, sodium sulfite (Sigma-Aldrich, 0.01, 0.1, 1.0, 1.5, or 2.0 M) was added to the chamber. The change in fluorescence intensity of the O_2 indicator flowing through the microfluidic device at 1.6 psi exposed to 0.0, 0.01, 0.1, 1.0, 1.5, and 2.0 M sodium sulfite ($NaSO_3$) was measured using a RatioMaster system (Photon Technology

International) and converted to a PO_2 value using the Stern-Volmer equation, $I_0 - I = 1 + PO_2 \times K_q$, in which I_0 is the maximum of the fluorescence intensity and K_q is the quenching constant. Because PO_2 in N_2-bubbled dye (after bubbling for 16 hours) and air-saturated dye was 34 mmHg and 174 mmHg, respectively (measured and calibrated using a World Precision Instruments dissolved O_2 meter and a Bayer RAPIDLab 248 blood gas analyzer), these values of I_0 and K_q were used to calculate PO_2 in microfluidic channels, $I_0 = 21129.5$ and $K_q = 0.00262501$.

Human RBCs were collected from healthy donors and prepared on the day of use. The RBCs were separated from plasma by centrifuging 3 mL of blood at 500 rcf at 20°C for 1.5 minutes. The supernatant was removed by aspiration. The packed RBCs were resuspended and washed three times in PBS buffer. The RBCs were then diluted with a PBS solution (3%, v/v) that in some experiments had been bubbled with N_2 overnight. The resuspended RBCs were introduced into the microfluidic channel. Apyrase (40 U/mL), L-NAME (3 mM), CNQX (200 μM), or diamide (200 μM) was added to the PBS in some experiments. In some experiments, potassium channel inhibitors (4-aminopyridine (4-AP, 1 mM), charybdotoxin (100 nM), or iberiotoxin (100 nM)) were used to treat RBCs for 5 to 10 minutes before the RBCs were introduced into the microfluidic channel.

To measure RBC velocity during exposure to various PO_2 conditions (sodium sulfite at 0.0, 0.01, 0.1, and 1.0 M), RBCs were injected into the device and pushed through the constriction channel at a constant pressure of 1.6 psi using a gas regulator (Omega DPG1001B) with a precision of 0.1 psi. The movements of single RBCs in the introduction and constriction segments of the channel were recorded using a high-speed video camera (Phantom Miro M120, 1900 frames per second) mounted on an inverted microscope (Leica

DMI 6000B). The velocities of RBCs were obtained by analyzing the video using Phantom Camera Control software. The velocity of RBCs moving through the 1 mm-long introduction channel was 4.6061 mm/s ± 0.8358 mm/s. Prior to entering the constriction channel where RBC velocity and deformation were quantified, RBCs had been exposed to the O_2 sink for approximately 217 ms while flowing through the introduction channel.

To determine the deformability of RBCs under various O_2 tensions, we utilized a microfluidic device with a constriction channel of 20 μm in width and 100 μm in length. The deformation of RBCs flowing through the constriction channel was recorded using a high-speed video camera. The change in length (D_L) and thickness (D_W) of RBCs flowing through the constriction channel was obtained by analyzing the videos using Phantom Camera Control software. The normalized elongation index (D_L/D_W) was used to characterize the deformation of RBCs in flow. Deformation of RBCs treated with diamide (200 μM) or potassium channel inhibitors (4-AP (1 mM), charybdotoxin (100 nM), or iberiotoxin (100 nM)) was also examined.

2.2.4. Intrinsic optical signal and two-photon imaging

Intrinsic optical signals (IOS) were captured at 52 frames per second with a 12-bit INFINITY2-1M CCD camera by custom-made MATLAB software as previously described [35]. A green (570 nm) light filter was used to image total changes in blood volume [38]. Two-photon imaging was performed using a custom-built microscope attached to a MaiTai HP Ti:Sapphire laser (Spectra Physics), a scan box controlled by FluoView software (FV300, Olympus), and a 20x objective (0.9 NA, Olympus). Intravascular fluorescein isothiocyanate-dextran (FITC-dextran) and intra-micropipette

Alexa Fluor 594 were excited at 820 nm. Midline arteriole and capillary RBC flow velocities within the activated hindlimb cortex identified by IOS were captured with line scans (scan rate ~1 kHz) placed along the length of the vessel. Vessel diameters were captured with line scans placed perpendicular to the axis of blood flow [39].

2.2.5. Two-photon image analysis

RBC velocities (= $\Delta x/\Delta t$, mm/s) were calculated from parallel-to-flow line scan images using the contrast between FITC-dextran-labeled plasma and unlabeled RBCs, using a modified version of the LS-PIV algorithm in MATLAB described elsewhere [40].

Vessel lumen diameters were calculated from perpendicular-to-flow line scan images using the contrast between the unlabeled tissue outside blood vessel lumens, unlabeled RBCs, and FITC-dextran-labeled plasma. As areas outside the capillary lumen were black, RBCs grey, and plasma white, capillary/vessel edges were determined by fitting sigmoidal curves to each edge and the diameter taken to be full width at half-maximum. This method provides increased accuracy due to subpixel resolution and robustness to artifacts as compared to simply setting a fixed threshold.

2.3. Results and discussions

To identify the brain region activated by hindlimb stimulation, the exposed cortex was visualized using IOS and high-speed two-photon line scan, which gives the information of RBC velocity in both arterioles and capillaries in the contralateral sensory cortex of lightly sedated mice (Figure 2-1A) [35, 39].

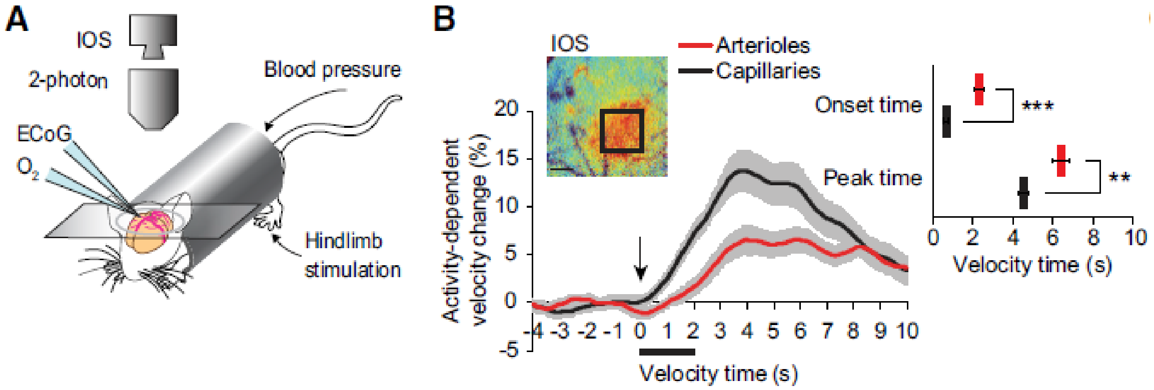

Figure 2-1. PO_2 Dips Are Necessary to Elicit Capillary Hyperemia. (A) Experimental setup for assessing functional hyperemia elicited by sensory stimulation. Arterial blood pressure was monitored through a femoral artery catheter while the other hindlimb was stimulated. Through a cranial window, intrinsic optical signaling (IOS) was used to identify the cortical region of functional hyperemia. LFP and O_2 sensor microelectrodes were placed in close proximity (10–20 µm) to one another within the activated region. During hindlimb stimulation, blood vessels in the activated contralateral hindlimb cortex were imaged using two-photon laser scanning microscopy. (B) Time-course plot of hindlimb stimulation-evoked RBC velocity changes in cortical arterioles (red) and capillaries (black). Inset: IOS imaging (shown as a pseudocolor image) was used to identify the location of the activated hindlimb cortex in all experiments. Scale bar, 300 mm. Evoked RBC velocity increases began in capillaries (0.67 ± 0.15 s) prior to arterioles (2.33 ± 0.22 s). n = 61–65, 25 mice. [30]

Only cortical arterioles and capillaries located in the cortical region that exhibited the largest activity-dependent increase in IOS were analyzed. A comparison of the onset time of stimulation-induced elevation in RBC velocity revealed that capillary RBC velocities (0.67 ± 0.15 s, n = 65, 25 mice) increased prior to RBC velocities of upstream arterioles (2.33 ± 0.22 s, n = 61, 25 mice) (Figure 2-1B), which is consistent with conclusions drawn by a prior study on vascular diameters [41]. The results of capillary diameter change (not shown) further proved that activity-dependent increases in capillary RBC velocities occur prior to both dilations of and RBC velocity increases in upstream arterioles, indicating that capillary hyperemia occurs before arterial hyperemia.

The observation that microinjection of O_2 scavengers induced pericyte- and vasoactive mediator-independent capillary hyperemia led us to hypothesize that O_2 tension itself, independent of the neurovascular unit, can control RBC deformation and thus RBC flow through capillaries. To test this idea in the absence of the neurovascular unit, we turned to an *ex vivo* assessment of the effect of oxygenation on RBC flow through an artificial capillary. We employed a microfluidic device in which isolated human RBCs pass through a narrow flow channel (Figure 2-2A) [17, 37, 42, 43]. This approach allowed an evaluation of RBC velocity in the absence of the cellular components of the neurovascular unit.

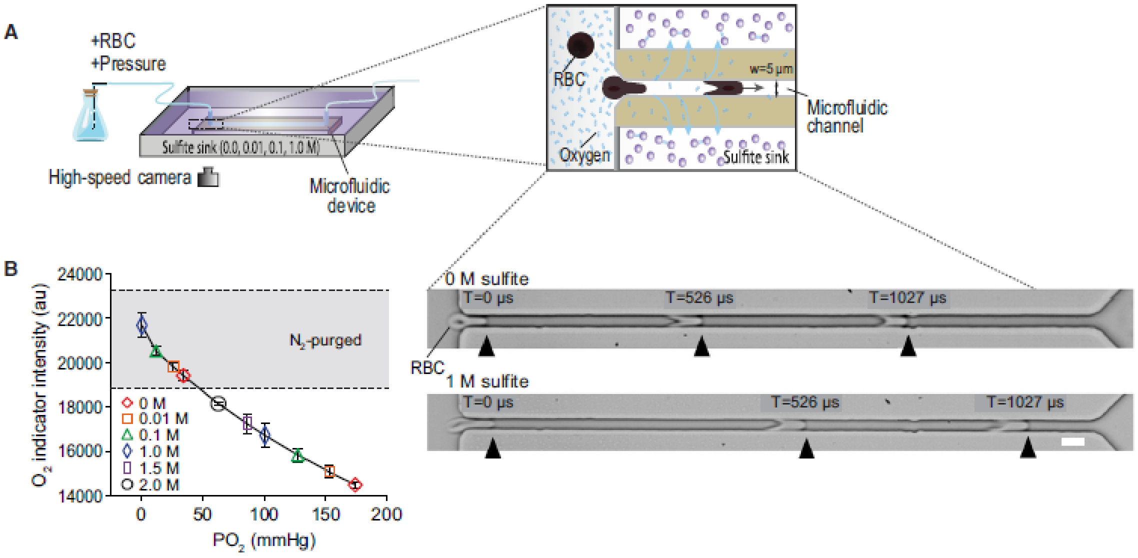

Figure 2-2. *Ex vivo* experiments of velocity measurement under hypoxia. (A) A diagram of the experimental setup for *ex vivo* analysis of the effect of PO_2 on RBC flow velocity. Human RBCs were added to the bath containing PBS and forced to flow through a microfluidic device containing a narrow channel by applying a constant pressure (1.6 psi). The microfluidic device was submerged in an O_2 sink (chamber containing H_2O with 0.0, 0.01, 0.1, or 1.0 M sodium sulfite). PO_2 in the microfluidic channel was successively lowered by increasing the concentration of sulfite in the O_2 sink (0.0–1.0 M). RBC motion was captured by a high-speed camera. (B) Left: colorimetrically quantify PO_2 in the capillary channel. The change in fluorescence intensity of the O_2 indicator dye solution flowing through the microfluidic device was measured during exposure to 0.0, 0.01, 0.1, 1.0, 1.5, and 2.0 M sodium sulfite solution and converted to PO_2. Right: images comparing RBC flow within an O_2 sink containing 0 or 1 M sulfite. Images of flowing RBCs captured by the high-speed camera at sequential time points are superimposed. Error bar: 5 µm.

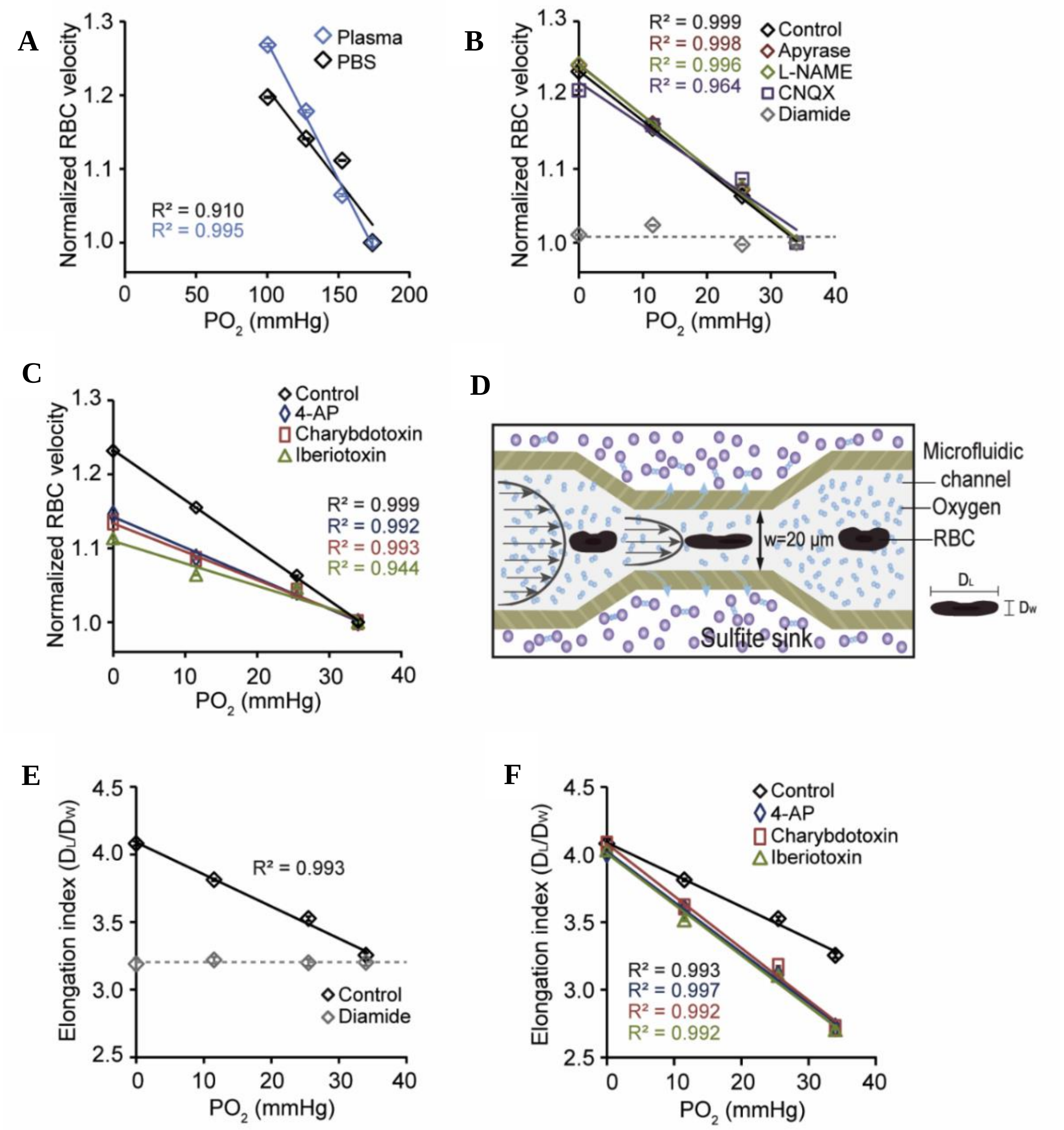

Figure 2-3. (A) Lowering PO_2 in the microfluidic channel caused an increase in RBC velocity. (B) Dephosphorylation of extracellular ATP or inhibition of NOS and AMPA receptors did not alter RBC velocity increases in response to lowering surrounding PO_2. When diamide was added to stiffen RBC membranes, lowering PO_2 failed to increase RBC velocity compared to controls. (C) In the presence of the potassium channel inhibitors the sensitivity of RBC velocity to the change in PO_2 was reduced. (D) A schematic of the experimental setup for *ex vivo* analysis of the effect of PO_2 on RBC deformability. (E) The elongation index (D_L/D_W) of RBCs changed over O_2 level change. (F) Elongation indexes (D_L/D_W) of control RBCs and RBCs treated with potassium inhibitors at different O_2 tensions.

Since the capillary lumen is considerably smaller than RBC diameters, RBC deformability is a major determinant of the speed by which the RBC passes through a capillary [44]. The microfluidic device made of PDMS was submerged in a chamber containing sodium sulfite, an O_2 scavenger. Since PDMS is O_2, but not H_2O, permeable the chamber functioned as a sink for O_2 (Figure 2-2A). A colorimetric calibration, based on adding the O_2-sensing dye tris(2,2'-bipyridyl)dichlororuthenium(II) hexahydrate to deionized (DI) water showed that PO_2 in the flow channel was an inverse function of the sulfite concentration (0 to 2 M) (Figure 2-2B). Remarkably, the velocity of RBCs flowing through the channel increased as a function of O_2 depletion, indicating that brief deoxygenation alone can affect the mechanical properties of RBCs (Figures 2-2B and 2-3A). The O_2-dependent increase in RBC velocity was observed when RBCs were resuspended in either plasma or PBS (Figure 2-3A). We focused on the effects of relatively lower PO_2. In these experiments, the PBS was first purged with N_2 until the PO_2 reached 34 mmHg, approximating normal brain PO_2 [45]. Similar to above, RBCs were driven through a microfluidic chamber immersed in a sulfite sink (0 to 1M) and colorimetrically calibrated (Figure 2-2B). This analysis showed that at a relatively lower range of O_2 tension, RBC velocities became more sensitive to surrounding changes in PO_2 ($p < 0.001$, t test with Bonferroni test, compared to PBS without N_2 purging and plasma) (Figures 2-3A and 2-3B). Interestingly, however, increasing the O_2 from 21% to 100% (or from PO_2 ~160 mmHg to ~760 mmHg) failed to alter RBC velocity in the microfluidic capillary (1.000 normalized velocity in 21% versus 0.998 normalized velocity in 100% O_2, n = 9–

19, $p > 0.05$, t test), consistent with the notion that at super physiologic PO_2, hemoglobin continues to be maximally saturated with O_2 and RBCs reach the limit of their ability to bind additional O_2 and respond with velocity changes.

We also found that the PO_2-elicited increase in RBC flow velocity was not a result of direct ATP or NO release. Exposing RBCs to the ATP-degrading enzyme apyrase (40 U/mL) or the NO synthase inhibitor L-NAME (3 mM) did not affect PO_2-induced elevations in RBC velocity (Figure 2-3B), in accordance with the *in vivo* observation that L-NAME failed to suppress capillary hyperemia (data not shown). In addition, CNQX had no effect on PO_2-induced increases in RBC velocity through the microfluidic channel (Figure 2-3B). When RBCs were treated with K^+ channel inhibitors (4-AP [non-selective voltage-dependent K^+ channel blocker, 1 mM], charybdotoxin [Ca^{2+}-activated voltage-gated K^+ channel blocker, 100 nM], or iberiotoxin [large-conductance Ca^{2+}-activated K^+ channel blocker, 100 nM]), however, the sensitivity of RBC velocity to PO_2 changes decreased (Figure 2-3C), suggesting that K^+ flux across the membrane plays a role in the velocity of RBC flow in capillaries. As a negative control, RBCs were treated with diamide, which stiffens the RBC membrane by crosslinking the cytoskeletal spectrin network [17]. The flow velocity of diamide exposed RBCs was unaffected by PO_2, supporting the notion that the PO_2-induced increase in RBC flow velocity is due to increased deformability of the RBC membrane (Figure 2-3B). To directly test whether RBC deformability is controlled by PO_2, we assessed the shear-induced deformability of RBCs flowing in a relatively large-sized microfluidic channel containing a segment of constriction (width = 20 µm) (Figure 2-3D).

The shear induced deformability of RBCs was characterized by the elongation index D_L/D_W, where D_L and D_W represented the length and thickness of an RBC flowing through the constriction, respectively. We found that the elongation of RBCs in response to shear stress increased as PO_2 decreased, demonstrating that RBCs are more flexible in lower PO_2 conditions (Figure 2-3E). The dependence of RBC deformability on PO_2 was significantly diminished when diamide was added (Figure 2-3E). RBCs treated with the K^+ channel blockers 4-AP (1 mM), charybdotoxin (100 nM), or iberiotoxin (100 nM) also exhibited reduced sensitivity to PO_2 changes compared to controls (Figure 2-3F). These data show that lowering PO_2 increases RBC deformability and thereby the velocity by which RBCs pass through a narrow *ex vivo* capillary lacking endothelial cells, pericytes, and astrocytes. Exposure to K^+ channel inhibitors reduced the deformability of RBCs and thus the potency by which PO_2 increased RBC flow velocity. This latter observation is consistent with prior studies documenting that a decrease in cell volume mediated by K^+ efflux and water loss may play a role in permitting RBC deformation during the shear stress associated with squeezing through a narrow capillary [43].

2.4. Conclusion

Functional hyperemia is an integrated response that tightly couples O_2 consumption with O_2 supply. Here we show that both spontaneous and activity-induced dips in tissue PO_2 drive the earliest phase of capillary hyperemia. Furthermore, PO_2 directly controls the velocity by which RBCs transit through a narrow channel in a microfluidic device. Thus, RBCs may themselves serve as autonomous regulators of capillary perfusion that operate independently of the neurovascular unit and the release of vasoactive molecules. The idea that erythrocytes—the major suppliers of O_2—function not only as O_2 carriers but also as O_2 sensors and regulators of capillary blood flow provides a simple, yet swift and precise, mechanism for controlling the cerebral microcirculation.

3. OXYGEN TENSION–MEDIATED ERYTHROCYTE MEMBRANE INTERACTIONS REGULATE CEREBRAL CAPILLARY HYPEREMIA

We demonstrated previously that cerebral functional hyperemia is initiated in brain capillaries and RBCs act as act as oxygen sensors to increase their deformability and flow velocity in response to local oxygen tension (PO_2) drop in the brain [30]. However, it remains unclear how RBC membrane mechanics change in response to PO_2 drop and how RBC deformability relates quantitatively to RBC velocity in capillaries. Here, we combined *ex vivo* microfluidic approaches with *in vivo* two-photon imaging techniques and studied mechanistically PO_2-regulated RBC dynamics in capillary using transgenic mice with modified deoxyHb-band 3 interaction. In particular, we showed that 1) the capillary velocity and shear-induced elongation of RBCs from transgenic mice with either increased or decreased deoxyHb-band 3 interaction lose the sensitivity to local PO_2 change in microfluidics; 2) chemical modification of deoxyHb-band 3 interaction in human and wild type mice RBCs also can manipulate the PO_2-regulated capillary velocity and shear-induced elongation in microfluidics; 3) *in vivo* capillary velocity of RBCs in transgenic mice with modified deoxyHb-band 3 interaction showed impaired responses to PO_2 changes; 4) RBC velocity and tank-treading frequency depend on the duration of PO_2 exposure and a lubrication model relates RBC membrane tension to velocity in capillary.[46]

3.1. Introduction

Thinking, reading, writing, or throwing a baseball are all activities in which neural activity is coupled with local elevation in cerebral blood flow (CBF). The mechanisms by which neural activity triggers hyperemia have been extensively studied, in part, because neurovascular coupling forms the basis for functional brain imaging [47, 48]. Defects in neurovascular coupling are also believed to contribute to cognitive decline in neurodegenerative conditions such as Alzheimer disease, as well as in hypertension and stroke [26]. Despite the uncontested tight linkage between neural activity and cerebrovascular responses, the question of what drives functional hyperemia is still unclear.

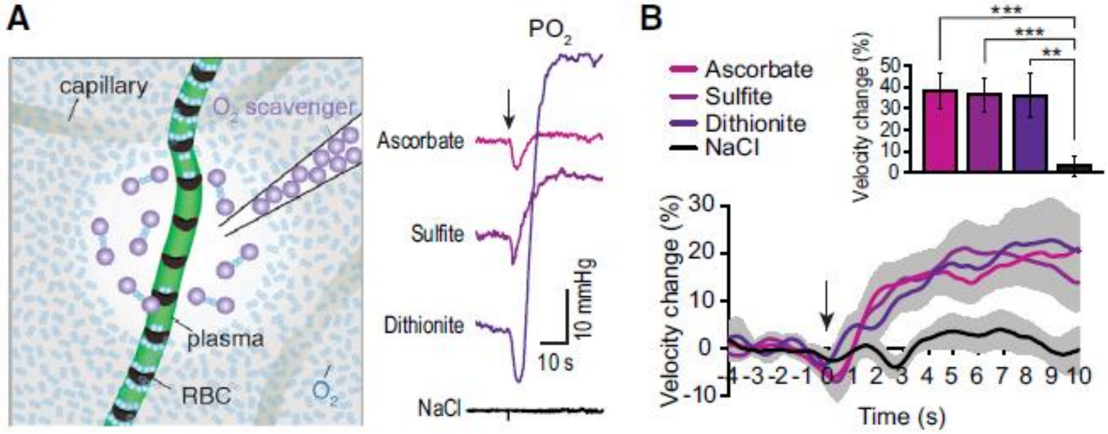

Figure 3-1. PO_2 dips can trigger capillary hyperemia. (A) Left panel is the scheme of the experimental setup to puff O_2 scavenger around the capillary and study the local effect. The right panel is the results of local O_2 dip after applying O_2 scavenger. (B) RBC velocity increase in the capillary after microinjection of O_2 scavenger. [30]

Most recently, it has emerged that functional hyperemia is initiated in the smallest blood vessels in brain, capillaries, where activity-driven decreases in tissue oxygen tension (PO_2) directly increase the velocity of RBCs measured both *in vivo* and *ex vivo*, as shown in Figure 3-1 [30]. Analysis in microfluidic chambers, in which RBC velocity can be studied in the absence of the neurovascular unit, shows that changes in PO_2 can directly trigger an increase in RBC flow velocity by increasing RBC deformability, thus decreasing vascular resistance [30]. As such, RBCs are active players in capillary hyperemia, and promptly increase O_2 delivery in response to activity-induced local changes in PO_2. Such RBC mediated capillary hyperemia thus provides a simple yet robust mechanism for swift and precise local increases in capillary flow in response to the ever-changing patterns of neural activity within the central nervous system (CNS). These observations, however, also prompt a new line of questions. For example, what is the molecular mechanism that regulates RBCs' responses to the change of PO_2? How quantitatively does the RBC capillary velocity relate to its deformability? What is the dynamics of PO_2-regulated RBC capillary velocity?

Previous studies have shown that PO_2 is a potent regulator of multiple RBC activities including glucose metabolism [49, 50], cation transport [19], ATP release [20, 21] and cytoskeletal organization [21, 51-53]. In particular, the reversible binding of deoxygenated hemoglobin (deoxyHb) with band 3 has been postulated to be critical in many of these processes because the cytoplasmic domain of band 3 contains the only known hemoglobin (Hb) binding site on the RBC membrane and Hb-band 3 interaction is strongly O_2-dependent [54-56]. As indicated in Figure 3-2 [51], increased deoxyHb-band 3 interaction at decreased PO_2, for example, reduces the band 3-ankyrin interaction on the

RBC membrane, resulting in a mildly weakened membrane [51]. Whether and how such changes will affect RBC deformability and velocity in capillary, however, is unclear. Here, we hypothesize that deoxyHb-band 3 interaction during RBC deoxygenation induces the displacement of ankyrin from band 3, which leads to a more deformable RBC membrane and thus an increased capillary velocity.

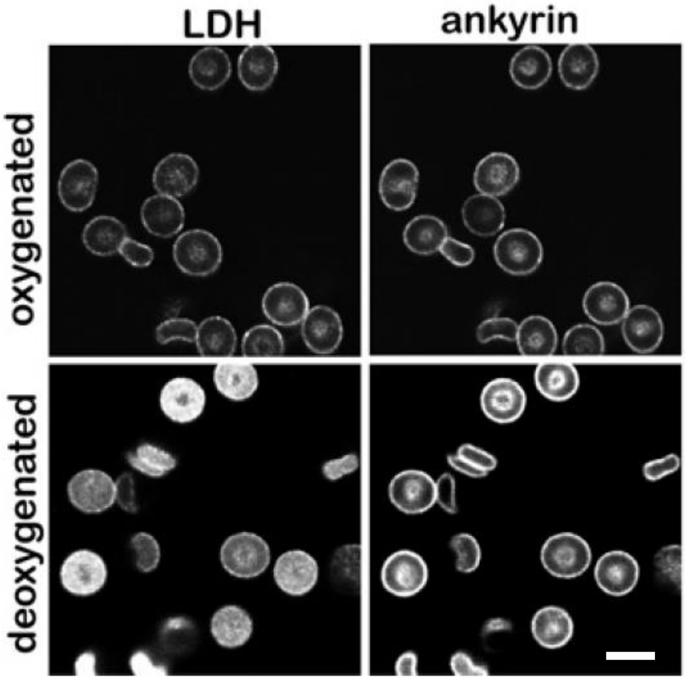

Figure 3-2. The accessibility of ankyrin increases with the deoxygenation of human RBCs. The right-hand panel indicates that the intensity increased after deoxygenation of stained human RBCs, showing the increased accessibility of ankyrin, which proves the decreased interactions between ankyrin and band 3. Error bar: 10 µm. [51]

To test the hypothesis, we have combined *ex vivo* microfluidic approach and *in vivo* two photon laser scanning microscopy to measure RBC deformability and capillary velocity at controlled PO_2. Results from wild type mice and transgenic mice that have modified RBC deoxyHb-band 3 interactions are obtained. Additionally, we show pharmacological manipulations of the deoxyHb-band 3/band 3-ankyrin interaction in RBCs from wild type mice and human to control the capillary RBC velocity and deformability in response to reduced PO_2. Lastly, the dynamics of PO_2-regulated RBC capillary velocity are investigated and a critical PO_2 exposure time is proposed.

3.2 Experimental methods

3.2.1 Animals and surgical preparation

Three strains of transgenic mice (mRBC-subst 1-35, mRBC-del 1-11, and mRBC-del 12-23) were kindly provided by the David Bodine lab from NIH. Wild type mice (mRBC-WT, C57BL/6J) were purchased from the Jaskson Lab. Anesthesia was induced in experimental animals with 3.0% isoflurane in room air and maintained at 1.5-2.0% during surgical preparation. Depth of anesthesia was monitored by toe-pinch, or blood pressure. Body temperature was maintained by a water perfused thermal pad (Gaymar T/Pump) set at 37°C. A custom-made metal plate was glued to the skull and a 2-3 mm diameter cranial window was made over the hindlimb cortex for imaging (stereotaxic coordinates: 2 mm lateral; 2 mm anterior of bregma). Agarose (0.8% in artificial CSF (aCSF), 37˚C) was applied and a glass coverslip was sealed to the metal plate [31, 33].

All experimental procedures were approved by the University Committee on Animal Resources at the University of Rochester and effort was taken to minimize the number of animals used.

3.2.2 RBC preparation and treatment

Whole blood was extracted from healthy human donors or wild type and transgenic mice and prepared on the day of use. RBCs were separated from plasma by centrifuging 1 mL of whole blood at 500 g at 20°C for 1.5 minutes. The supernatant was removed by aspiration. The packed RBCs were resuspended and washed three times in PBS buffer. The RBCs were then diluted with a PBS solution (3%, v/v) that in some experiments had been bubbled with N_2 overnight. Note that for mRBCs, PBS was prepared as follow: 152 mM NaCl, 2.7 mM KCl, 8.1 mM Na_2HPO_4, 1.47 KH_2PO_4, and 10 mM glucose, pH = 7.4, Osmolality: 340 mOsm/Kg; For human RBCs, PBS was used as purchased from ThermoFisher Scientific (pH = 7.2, Osmolality: 280-320 mOsm/Kg, Catalog # 20012027). PEP (phosphoenolpyruvate) and Pi (inorganic phosphate) solutions were prepared in PBS as follow [57]: PEP solution (PEP 50 mM, Mannitol 28.8 mM, glucose 50 mM, NaCl 20 mM and adenine 1 mM) and Pi solution (sodium phosphate 50 mM, Mannitol 28.8 mM, glucose 50 mM, NaCl 20 mM and adenine 1 mM). The pH of the solutions was adjusted to 6.0. Packed RBCs were suspended into either PEP or Pi solution and incubated for one hour at 37˚C and then washed twice with PBS [57]. To determine the concentration of 2,3-DPG in RBCs, UV-testing was conducted following the manufacturing protocol of Sigma Kit (Sigma-Aldrich, catalog # 10148334001). In pervanadate treatment, packed RBCs were suspended in PBS with 0.5 mM sodium orthovanadate and 150 mM H_2O_2. After incubated at 37˚C for 30 mins, RBCs were washed three times using PBS and resuspended in a fresh PBS with glucose for 180 mins to obtain 100% phosphorylation of band 3 and ankyrin.

3.2.3 Microfluidic device and RBC imaging

Microfluidic devices were fabricated with PDMS using standard soft photolithography techniques [17, 36, 37]. The microfluidic device was connected via a short polyethylene (PE 20) tube to an RBC reservoir where a constant pressure (1.6 psi) was applied by using a gas regulator (Omega, DPG1001B) with a precision of 0.1 psi. To control PO_2 inside the channel, the entire microfluidic device was immersed in a customized glass chamber filled with an aqueous solution containing 0, 0.01, 0.1, or 1.0M of sodium sulfite (Sigma-Aldrich) and the PO_2 inside the was equilibrated with the surrounding environment for 20 mins before experiments.

PO_2 calibration in microfluidics: To colorimetrically quantify PO_2 in the microfluidic channel, 25 μM of tris(2,2'-bipyridyl)dichlororuthenium(II) hexahydrate (an O_2 indicator, Sigma-Aldrich) was prepared in N_2-bubbled or air-saturated deionized (DI) water and injected into the microfluidic device at a constant pressure (1.6 psi). The change in fluorescence intensity of the O_2 indicator flowing through the microfluidic device was measured using a RatioMaster system (Photon Technology International) and converted to a PO_2 value using the Stern-Volmer equation, $I_0 / I = 1 + PO_2 \times K_q$, in which I_0 is the maximum of the fluorescence intensity and K_q is the quenching constant. To calculate I_0 and K_q, we used PO_2 of 34 mmHg and 174 mmHg respectively in N_2-bubbled dye solution (after bubbling for 16 hours) and air-saturated dye solution, which was measured and calibrated using a World Precision Instruments dissolved O_2 meter and a Bayer RAPIDLab 248 blood gas analyzer. These values of I_0 and K_q were then used to calculate PO_2 in microfluidic channels.

RBC velocity and deformability measurement as a function of PO_2: To measure mRBC velocity, we injected mRBCs into a microfluidic device with a constriction of w_c = 3 µm and h = 4 µm at a constant pressure of 1.6 psi. The movements of mRBCs in the constriction were recorded by a high-speed video camera (Phantom Miro M120, 1900 frames per second) mounted on an inverted microscope (Leica DMI 6000B). The recorded videos were analyzed using Phantom Camera Control software and imagingJ and mRBC velocity was calculated assuming a steady flow condition. To determine the deformability of mRBCs, we utilized a microfluidic device with a constriction of w_c = 10 µm and h = 7.4 µm. The deformation of mRBCs flowing through the constriction was recorded using the high-speed camera and characterized by the change of elongation index D_L / D_W, where D_L and D_W is the length and thickness of mRBC respectively.

Table 3-1. Dimensions of microfluidic channels in use for human RBC measurement

Channel type (for human RBC)	**Overall height**	**Width of constrction**
Velocity measurement	7 µm	5 µm
Deformability measurement	30 µm	20 µm

To examine human RBC velocity and deformation as a function of PO_2, we used the same approach as described above expect that a microfluidic device with a constriction of w_c = 5 µm and h = 7 µm and w_c = 20 µm and h = 30 µm was used respectively for the hman RBC velocity and deformation meaasurement. To study the effect of total exposure time of reduced PO_2 on RBC velocity, we used microfluidic devices with different lengths of channel before the constriction (100, 500, 1000, 1500, 3000, 5000, 7000 and 9000 µm) to control the total exposure time. In this case, the PO_2 was controlled at 0 and 34 mmHg.

The data was then fitted using an exponential function $y = y_0 + Aexp(\frac{-(x-x_0)}{\tau})$ where τ is the characteristic exponential time constant.

RBC tank-treading frequency measurement: A microfluidic channel containing a constriction (w_c = 20 μm and h = 38 μm) was used to measure tank-treading frequency of human RBCs. The microfluidic device was immersed in a sulfite sink with different concentrations of sodium sulfite (0, 0.01, 0.1, to 1 M). The length of the channel before constriction was varied from 600, 4200 to 12000 μm to obtain a total exposure time of 18 ± 4, 192 ± 30, and 377 ± 11 ms respectively. 1 mL human RBCs suspension in PBS (1.5 % v/v) was mixed with 10 μL 1 μm polystyrene microspheres (0.5 % w/v in PBS, Polybead, Polysciences, Inc.) and injected into the microfluidic channel. Dextran (Sigma-Aldrich, Leuconostoc spp. Mr 450,000-650,000) was added to increase the viscosity of RBC suspension from 1.36 mPa·s, 2.61 mPa·s, to 4.66 mPa·s as measured by a rheometer (Discovery HR-2 Hybrid Rheometer, TA Instrument). The rotation of the microbead on RBCs was recorded using a high-speed camera and the tank-treading frequency was calculated as 1/the time for the microbead moving along with the membrane for one revolution.

3.2.4 *In vivo* two-photon imaging

Two-photon imaging was performed using a Thorlab two-photon setup attached to a MaiTai HP Ti: Sapphire laser (Spectra Physics). A 20× objective (0.9 NA, Olympus) was used. Intravascular fluorescein isothiocyanate-dextran (FITC-dextran) (2.5% in saline) is injected from the tail of the mouse and excited at 820 nm. To prepare the sulfite puffing solution, 0.01M or 1M sodium sulfite was dissolved in 10 mM HEPES (with a drop of HCl to adjust pH to 7.3) containing 100 μM Alexa Fluor 594 and loaded into a glass micropipette with a tip diameter of 2-3 μm. The puffing micropipette was then carefully loaded into a capillary bed in the cerebral cortex and the sulfite solution was puffed at 10 psi (~20 ms) controlled by a Picospritzer III. Capillary RBC velocity was captured with line scans (scan rate ~1 kHz) placed along the length of the capillary. RBC velocities (= $\Delta x/\Delta t$, mm/s) were calculated from parallel-to-flow line scan images using the contrast between FITC-dextran-labeled plasma and unlabeled RBCs, using a modified version of the LS-PIV algorithm in MATLAB described elsewhere [40].

Parameter Estimation: A zero-phase running average filter (window size ~1 s) was used to smooth raw velocity data after outliers (raw data points > 3 standard deviations (SDs) from mean of trace) were removed. Onset of the evoked response was estimated by fitting a line to the slope between 20% and 80% to the peak of the response and calculating the time of the line's *x*-intercept [58] (Figure 3-3). The 5-10 seconds immediately prior to puffing stimulation was considered baseline, and responses occurring within 20 seconds after the start of stimulation were analyzed. For the purpose of plotting pooled traces, data were interpolated at 10 ms intervals in order to line up the time axes.

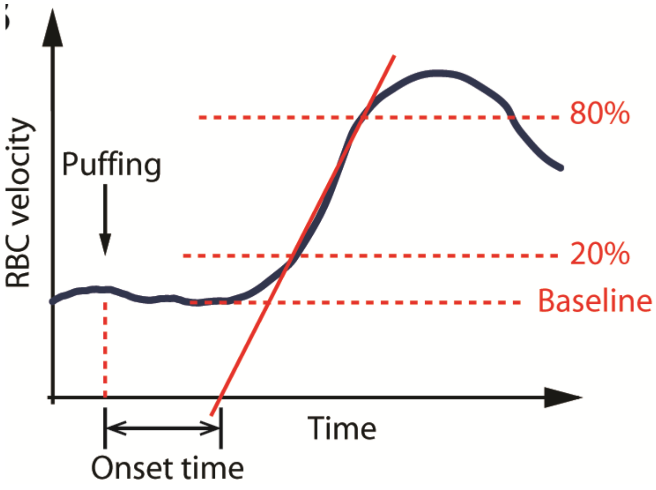

Figure 3-3. Scheme showing the calculation of onset time of velocity increase in the *in vivo* puffing experiments.

3.3 Results and discusstion

3.3.1 PO_2-regulated RBC velocity in capillary is mediated by deoxyHb-band 3 interaction.

To explore the roles of deoxyHb-band 3 interaction in PO_2-regulated RBC capillary velocity, we examined *ex vivo* RBC velocity in a microfluidic capillary using RBCs from three transgenic mice that contained “humanized” band 3 (Figure 3-4B) [21]. The first strain of mouse had RBCs that the NH_2-terminal residues 1-45 on the cytoplasmic domain of band 3 was replaced by the homologous sequence (residues 1-35) of human band 3 (mRBC-subst 1-35) [53], including the deoxyHb-band 3 binding site (residues 12-23). RBCs from the second strain of mouse had the same “humanized” band 3 except that the deoxyHb-band 3 binding site was deleted (mRBC-del 12-23). As a result, deoxyHb-band 3 interaction was diminished or significantly weakened. RBCs from the third strain also had the same “humanized” band 3 but a homologous sequence (1-MEELQDDYEDM-11) adjacent to residues 12-23 of band 3 was removed (mRBC-del 1-11). Residues 1-11 are known to inhibit band 3 interaction with deoxyHb, removal of residues 1-11 thus enchances band 3-deoxyHb interaction [53]. RBCs from these three strains of mouse together with wild type mouse RBCs (mRBC-WT) were used to examine RBC velocity as a function of PO_2 in microfluidics (Figure 3-4C). Particularly, RBCs were dispersed into a PBS buffer that was purged by N_2 overnight. The RBC suspension was then injected at a constant pressure (1.6 psi) into a PDMS microfluidic device containing a constriction capillary (w_c = 3 μm; h = 4 μm). The entire microfluidic device was immersed in a sulfite sink containing varied concentrations of sodium sulfite (an O_2 scavenger) to control PO_2 inside the microfluidic capillary. The motion of RBCs as a function of PO_2 in the constriction was then recorded by a high speed camera (Figure 3-4D). The results showed that the velocity of mRBC-WT and mRBC-subst 1-35 increased linearly as the decrease of PO_2 (Figure 3-4E) (mRBC-WT: n = 146 cells, 3 subjects, 3 trials, RBC velocity [mm/s] = -0.132 × PO_2 [mmHg] + 26.455, R^2 = 0.979; mRBC-subst 1-35: n =149 cells, 3 subjects, 3 trials, RBC velocity [mm/s] = -0.151 × PO_2 [mmHg] + 28.913, R^2 = 0.995), consistent with previous findings in human RBCs. The sensitivity of RBC velocity to PO_2 changes (slope of the fitting curve) was not signficantly different between mRBC-WT and mRBC-subst 1-35. The velocity of mRBC-subst 1-35, however, was significantly higher than that of mRBC-WT at each PO_2 level (Figure 3-3B). When RBCs with enhanced (mRBC-del 1-11) or weakened (mRBC-del 12-23) deoxyHb-band 3 interaction were used, the dependence of RBC velocity on PO_2 was completely diminished (Figure 3-5A). In addition, the average velocity of mRBC-del 12-23 was signficantly lower than that of mRBC-del 1-11 (Figure 3-5C), showing that reduced band 3-deoxyHb interaction could lead to decreased RBC capillary velocity. These sets of data thus demonstrate that modification of deoxyHb-band 3 interaction affects not only the magnitute of PO$_2$-regulated RBC capillary velocity but also the sensitivity of RBC velocity to PO$_2$ changes.

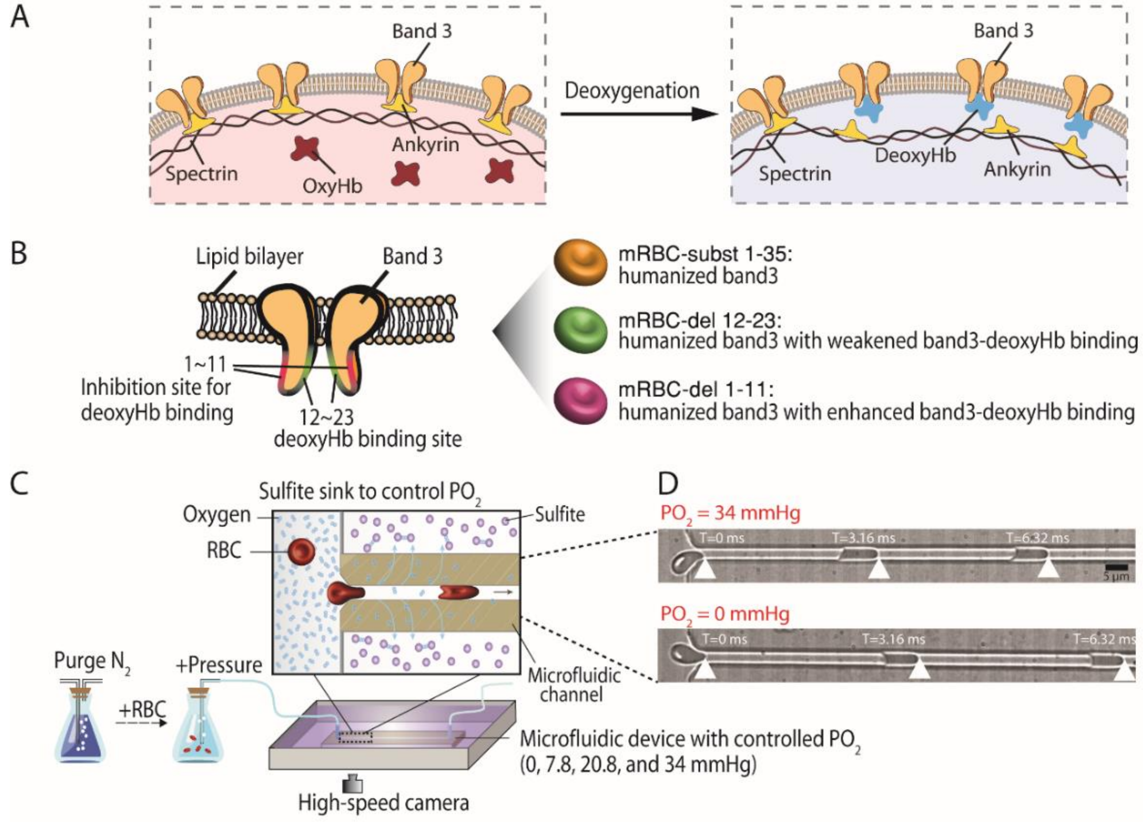

Figure 3-4. PO$_2$-regulated RBC velocity in capillary is mediated by deoxyHb-band 3 interaction. (A) Scheme of the band 3-Hb interaction during deoxygenation. (B) Schematics of transgenic mRBCs with modified deoxyHb-band 3 interaction. (C) Setup for *ex vivo* analysis of PO$_2$-regulated RBC velocity in capillary. (D) Time-lapse images showed that mRBCs flow faster at reduced PO$_2$. Scale bar: 5 µm.

We next examined whether deoxyHb-band 3 interaction also regulated RBC deformability. Figure 3-5D showed the microfluidic setup where a relatively wide constriction (w_c = 10 µm, h = 7.4 µm) was used to mesure shear-induced elongation of RBCs. PO$_2$ in the constriction was controlled by the sulfite sink and calibrated as described above. Shear-induced RBC elongation was characterized by using the elongation index, D_l /D_w, where D_l and D_w were, respectively, the length and thickness of an RBC flowing through the constriction. As shown in Figure 3-5E, elongation index of mRBC-WT and mRBC-subst 1-35 increased linearly as the decrease of PO_2, indicating that RBC deformability increases at lower PO_2 when deoxyHb-band 3 interaction is not compomised (mRBC-WT: n =209 cells, 3 subjects, 3 trials, D_l/D_w = -0.0228 × PO_2 [mmHg] + 2.7548, R^2 = 0.998; mRBC-subst 1-35: n = 195 cells, 3 subjects, 3 trials, D_l/D_w = -0.0137 × PO_2 [mmHg] + 2.6545, R^2 = 0.994).

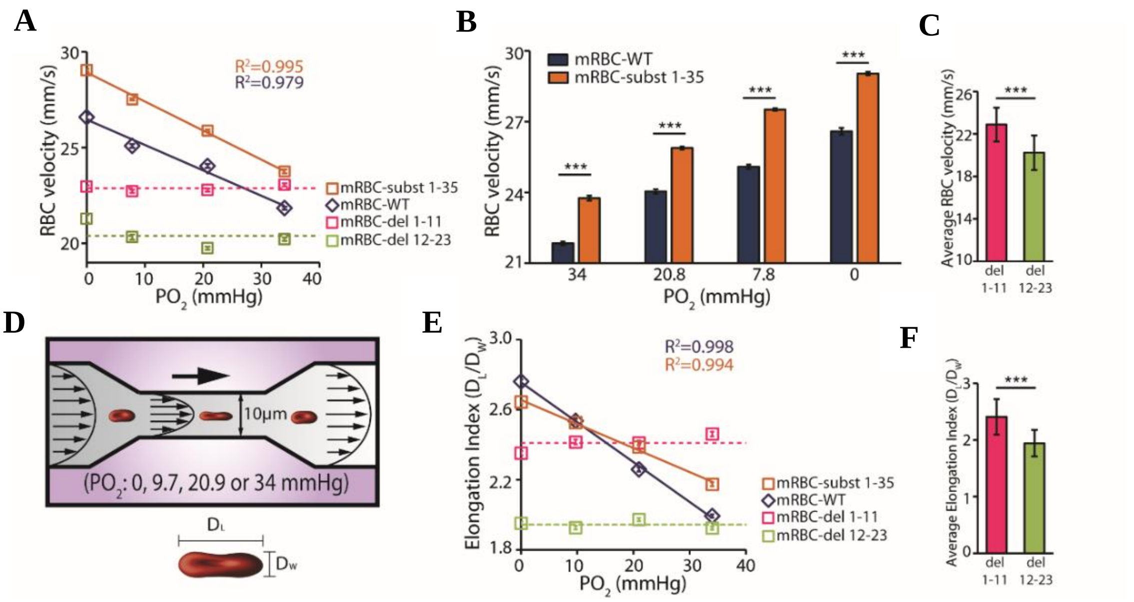

Figure 3-5. Results showing PO_2-regulated RBC velocity in capillary is mediated by deoxyHb-band 3 interaction. (A) mRBC velocity in capillary as a function of PO_2. (B) The velocity of mRBC-WT is significantly lower than that of mRBC-subst 1-35. (C) The velocity of mRBC-del 1-11 and mRBC-del 12-23 is not sensitive to surrounding PO_2 changes. (D) A schematic of the setup for *ex vivo* analysis of RBC deformability. (E) The elongation index (D_l/D_w) of mRBC increased linearly as the decrease of PO_2. (F) The D_l/D_w of mRBC and was not sensitive to PO_2 changes and remains relatively constant.

When RBCs with modified deoxyHb-band 3 interaction were used (mRBC-del 12-23 and mRBC-del 1-11), the elongation index of these RBCs was not dependent on PO_2 and the average elongation index of mRBC-del 12-23 was signficantly smaller than that of mRBC-del 1-11 (Figure 3-5B). These data of PO_2-regulated RBC deformability as a function of deoxyHb-band 3 interaction are consistent with the results of PO_2-regulated RBC capillary velocity and suggest that RBC deformability correlate tightly to RBC capillary velocity.

3.3.2 Transgenic mice with modified deoxyHb-band 3 interaction exhibit PO_2-independent capillary hyperemia *in vivo*

Although *ex vivo* microfluidic experiments demonstrated that the dependence of RBC capillary velocity on PO_2 could be manipulated by altering RBC band 3-deoxyHb interactions, it remained unclear whether band 3-deoxyHb interaction also contributed to PO_2-regulated RBC capillary velocity *in vivo*. To address this question, we used a laser scan two-photon microscope to measure *in vivo* RBC capillary velocity as a function of tissue PO_2 in the cerebral cortex of wild type mice (mRBC-WT) and transgenic mice (mRBC-subst 1-35, mRBC-del 1-11, and mRBC-del 12-23).

Under the guidance of two-photon imaging, we microinjected a sodium sulfite solution to the hindlimb cortex of a mouse brain to control local tissue PO_2 near capillaries (Figure 3-6A). Microinjection of sulfite triggered a rapid decrease in local tissue PO_2 and such PO_2 dips increased as the increase of sulfite concentration (Figure 3-6B).

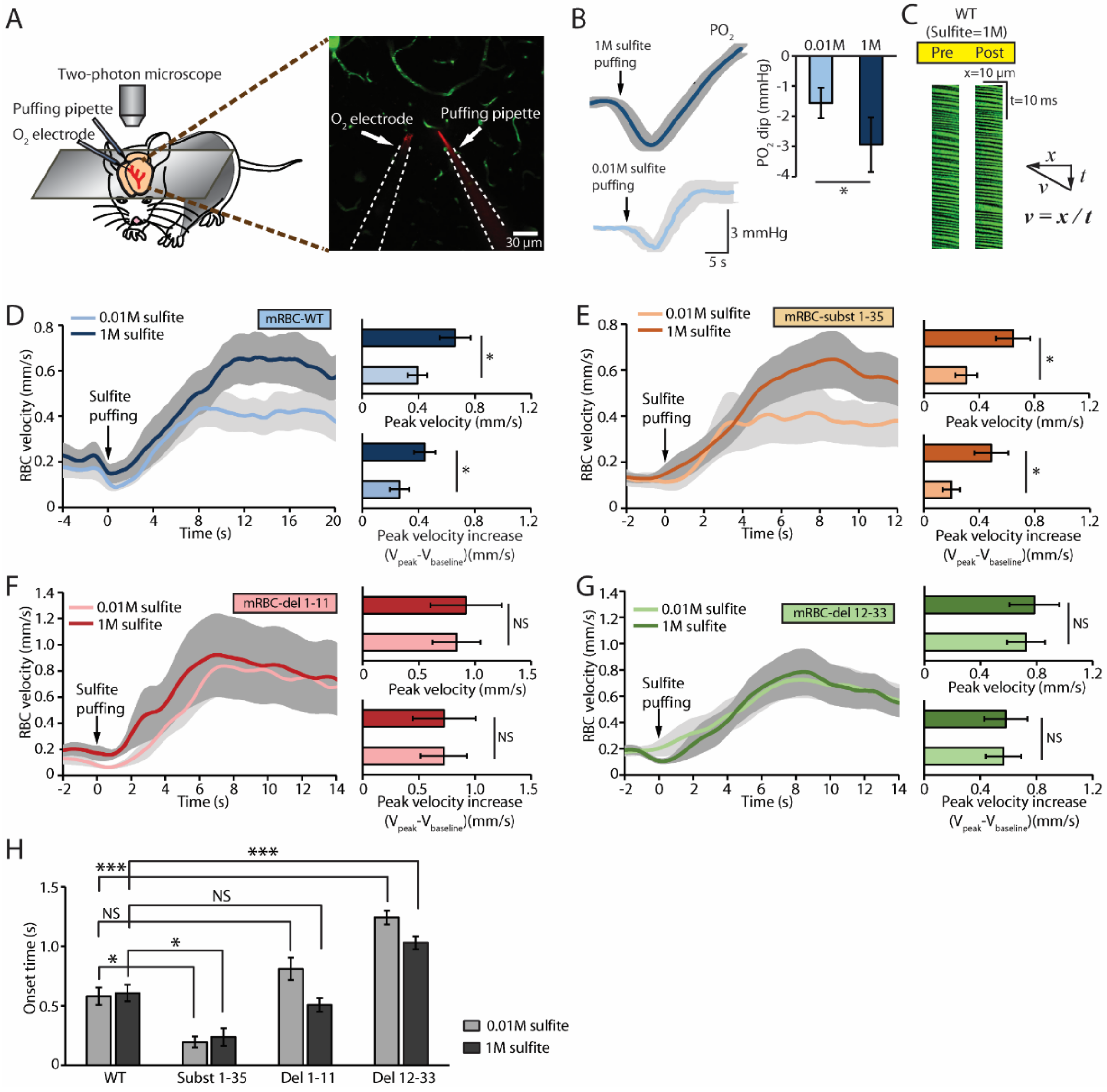

Figure 3-6. Transgenic mice with modified deoxyHb-band 3 interaction exhibit PO_2-independent capillary hyperemia *in vivo*. (A) Setup for *in vivo* assessing cerebral capillary hyperemia and tissue PO_2 upon locally applied O_2 scavenger in the mouse cerebral cortex. Scale bar: 30 µm. (B) Local changes of PO_2 are dose-dependent on the concentration of microinjected sulfite. (C) Typical images of the two-photon linescan of a capillary before and afer the microinjection of sulfite. (D) Time-course plot of RBC capillary velocity increase after microinjection of sulfite for mRBC-WT and transgenic mice (E) subst 1-35, (F) del 1-11, and (G) del 12-23. (H) The onset time of increase of RBC capillary velocity after sulfite puffing.

Note that the bi-phasic pattern of PO_2 response to sulfite puffing, e.g., an initial transient dip followed by a delayed long-lasting overshoot, was similar to previously observed activity-dependent PO_2 responses [30]. We then measured RBC velocity in capillaries as a function of local tissue PO_2 changes using a two-photon linescan. A typical linescan image acquired in mRBC-WT with longitudinal linescan before and after sulfite puffing was shown in Figure 3-6C, where x represents the scanning distance and t is time. Each RBC in the linescan image appeared as a black stripe and the slope of the stripe was velocity, v. Upon sulfite puffing, RBC capillary velocity increased. In mRBC-WT and mRBC-subst 1-35 mice, the peak velocity and the increase of peak velocity relative to baseline induced by 1M sulfite puffing were significantly higher than that by 0.01M sulfite puffing (Figure 3-6D and 3-6E), showing that *in vivo* RBC capillary velocity is regulated by local PO_2 changes. In mRBC-del 1-11 mice (Figure 3-6F) and mRBC-del 12-33 mice (Figure 3-6G) where band 3-deoxyHb interaction was respectively enhanced and weakened, however, the peak velocity and increase of peak velocity after sulfite puffing did not change as the increase of sulfite concentration, suggesting that local PO_2 changes fail to regulate RBC capillary velocity. These *in vivo* results are consistent with our *ex vivo* findings and highlight again the regulatory roles of deoxyHb-band 3 interaction in PO_2-dependent RBC capillary velocity. In addition, we further noticed that, upon sulfite puffing, the onset time of RBC velocity increase was significantly shorter in mRBC-subst 1-35 mice comparing to mRBC-WT mice (Figure 3-6H), suggesting that mouse RBCs with "huamnized" band 3 have a faster response time to PO_2 changes than WT mouse RBCs. The onset time of RBC velocity increase in mRBC-del 12-33 and mRBC-del 1-11 mice was respectively longer and comparable to that in mRBC-WT mice.

3.3.3 Biochemical modulation of deoxyHb-band 3 interaction in wild type RBCs regulates PO_2-dependent RBC velocity in capillary

To further evaluate the roles of deoxyHb- band 3 interaction in PO_2-regulated RBC capillary velocity, we utilized phosphoenolpyruvic acid (PEP), sodium phosphate (Pi) and pervanadate treatments to manipulate deoxyHb-band 3/band 3-cytoskeleton interactions in wild type mouse RBCs and human RBCs (Figure 3-7A). RBCs treated with PEP and Pi have increased and decreased intracellular concentration of 2,3-diphosphoglyceric acid (2,3-DPG), respectively. Because 2,3-DPG binds preferably to deoxyHb [59, 60], increase of 2,3-DPG, e.g., via PEP treatment, reduces the amount of deoxyHb available to bind band 3. In contrast, decrease of 2,3-DPG via Pi treatment increases the amount of deoxyHb available to bind band 3 [61].

Such change of the amount of deoxyHb is expected to alter the quantity of deoxyHb-band 3 association and its assoicated kinetic process, and consequently affects the magnitude of RBC capillary velocity and its sensitivity to PO_2 changes. Indeed, when both human RBCs and wild type mouse RBCs were treated with PEP and Pi and tested as a function of PO_2 in a microfluidic capillary, the sensitivity of RBC velocity to PO_2 changes (slope of the fitting curve) was significantly reduced after PEP and Pi treatments (Figure 3-7B and 3-7C). Velocity of hRBC-WT decreased linearly with the increase of PO_2 (hRBC-WT: n= 71 RBCs, 3 subjects, 3 trials, RBC velocity [mm/s] = $-0.451 \times PO_2$ [mmHg] + 82.074, $R^2 = 0.999$). After pervanadate treatment (hRBC-Pervanadate), RBC velocity was not sensitive to PO_2 changes and remained constant at 79.56 ± 0.28 mm/s (n = 198 RBCs, 4 subjects, 4 trials). RBC treated with Pi solution (hRBC-Pi) flew faster than that treated with PEP solution (hRBC-PEP).

The sensitivity of RBC velocity to PO_2 changes (as indicated by the slope) was reduced for both cases (hRBC-Pi: n= 174 RBCs, 4 subjects, 4 trials, RBC velocity [mm/s] = -0.068× PO_2 [mmHg] + 79.332, R^2 = 0.947; hRBC-PEP: n= 167 RBCs, 4 subjects, 4 trials, RBC velocity [mm/s] = -0.065× PO_2 [mmHg] + 74.198, R^2 = 0.906). The elongation index of hRBC-WT decreased linearly with the increase of PO_2 (hRBC-WT: n =239 RBCs, 3 subjects, 3 trials, D_l/D_w = -0.0236 × PO_2 [mmHg] + 4.0001, R^2 = 0.934). After pervanadate treatment (hRBC-Pervanadate), RBC deformation was not sensitive to PO_2 changes and remained constant at 4.08 ± 0.02 mm/s (n = 216 RBCs, 3 subjects, 3 trials). RBC treated with Pi solution (hRBC-Pi) was more deformation than that treated with PEP solution (hRBC-PEP). RBC deformation was less sensitivity to PO_2 changes for both cases (hRBC-PEP: n=144 RBCs, 3 subjects, 3 trials, D_l/D_w = -0.0102 × PO_2 [mmHg] + 3.6698, R^2 = 0.997; hRBC-Pi: n= 132 RBCs, 3 subjects, 3 trials, D_l/D_w = -0.0143 × PO_2 [mmHg] + 4.142, R^2 = 0.947). In addition, the velocity of RBCs treated with PEP was significantly lower than that of RBCs treated with Pi at each PO_2 level.

Furthermore, when RBCs were treated with pervanadate, which directly triggers tyrosine phosphorylation of band 3 and induces the disassociation of band 3 from its ankyrin linkage to the spectrin-actin skeleton without PO_2-dependent deoxyHb-band 3 interaction [62, 63], the dependence of RBC velocity on PO_2 was completely diminished (Figure 3-7B and 3-7C). The velocity of RBCs treated with pervanadate was also significantly higher than that of RBCs treated with PEP at most PO_2 levels. When RBC deformability (in terms of elongation index) as a function of PO_2 was further examined after PEP, Pi and pervanadate treatments, the sensitivity of RBC deformation to PO_2 changes was significantly reduced after PEP and Pi treatments and diminished after pervanadate treatment (Figure 3-7D and 3-7E). The dependence of RBC velocity on PO_2 for wild type mRBC (mRBC-WT) (mRBC-WT: n = 146 RBCs, 3 subjects, 3 trials, RBC velocity [mm/s] = -0.132 × PO_2 [mmHg] + 26.455, $R^2 = 0.979$) was diminished after pervanadate treatment (mRBC-Pervanadate, velocity is constant at 23.74 ± 0.13 mm/s, n = 138 RBCs, 3 subjects, 3 trials). The sensitivity of RBC capillary velocity to PO_2 changes was reduced after Pi and PEP treatments (mRBC-PEP: n = 146 RBCs, 3 subjects, 3 trials, RBC velocity [mm/s] = -0.071 × PO_2 [mmHg] + 22.557, $R^2 = 0.885$; mRBC-Pi: n = 159 RBCs, 3 subjects, 3 trials, RBC velocity [mm/s] = -0.11 × PO_2 [mmHg] + 28.296, $R^2 = 0.938$). The dependence of RBC defomration on PO_2 in mRBC-WT (mRBC-WT: n = 207, D_l/D_w = -0.0228 × PO_2 [mmHg] + 2.7548, $R^2 = 0.998$) was diminished after pervanadate treatment (D_l/D_w is constant at 2.44 ± 0.03, n= 216 RBCs, 3 subjects, 3 trials).

The sensitivity of RBC deformation to PO_2 changes was also reduced after Pi and PEP treatments (mRBC-PEP: n = 120 RBCs, 3 subjects, 3 trials, D_l/D_w = -0.0107 × PO_2 [mmHg] + 2.4383, $R^2 = 0.989$; mRBC-Pi: n = 125 RBCs, 3 subjects, 3 trials, D_l/D_w = -0.005 × PO_2 [mmHg] + 2.8088, $R^2 = 0.988$). The magnitude of elongation index at each PO_2 level was lower for RBCs treated PEP comparing with RBCs treated with Pi and pervanadate. Such similar trend of RBC deformability as a function of PO_2 as the observed PO_2-regulated RBC capillary velocity in wild type mouse RBCs and human RBCs highlights again the tight correlation between RBC deformability and RBC capillary velocity. Importantly, the data further suggests that PO_2-dependent RBC deformability and capillary velocity can be manipulated by controlling intracellular 2,3-DPG concentration and band 3 phosphorylation, which in turn regulates deoxyHb-band 3 and band 3-cytoskeletal interactions.

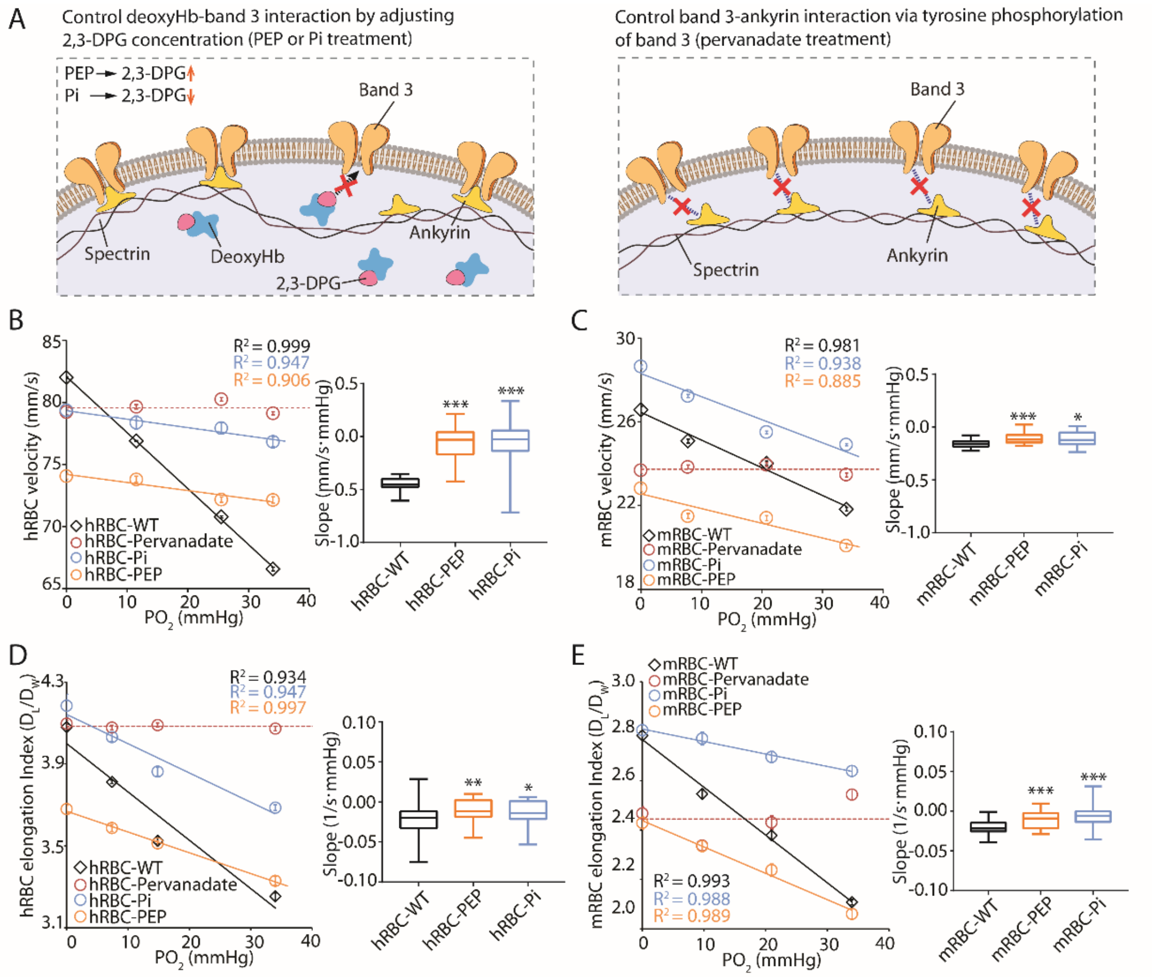

Figure 3-7. Biochemical modulation of band 3-deoxyHb interaction regulates PO$_2$-dependent RBC velocity in capillary. (A) Schematics of the biochemical approaches used to modulate band 3-deoxyHb and band 3-cytoskeletal interactions. Left: Band 3-deoxyHb interaction is manipulated by increasing or decreasing intracellular concentration of 2,3-DPG, which competes the deoxyHb binding site in band 3. Right: Tyrosine phosphorylation of band 3 (via pervanadate treatment) promotes dissociation of band 3 from the spectrin-actin skeleton. (B) Velocity of human RBCs in a microfluidic capillary (w_c = 5 µm, h = 7 µm) as a function of PO$_2$. (C) Deformation of human RBCs measured by the elongation index (D_l/D_w) in a microfluidic constriction (w_c = 20 µm, l_c = 100 µm, h = 30 µm) as a function of PO$_2$. (D) Velocity of murine RBCs in a microfluidic capillary (w_c = 3 µm, h = 4.5 µm) as a function of PO$_2$. (E) Deformation of murine RBCs measured by the elongation index (D_l/D_w) in a microfluidic constriction (w_c = 10 µm, l_c = 100 µm, h = 7.35 µm) as a function of PO$_2$.

3.3.4 Dynamics of PO_2-regulated RBC velocity in capillary

Although the results from both *ex vivo* and *in vivo* experiments have shown that deoxyHb-band 3 and band 3-cytoskeletal interactions contribute to PO_2-regulated RBC capillary velocity and deformability, the underlying mechanisms are elusive and several fundamental questions remain. For example, what is the evidence of RBC membrane detachment during deoxygenation? Does the duration of reduced PO_2 matter? How quantitatively does RBC capillary velocity relate to its deformability and why do RBCs with a higher deformability flow faster in capillary?

To answer these questions, we first examined the RBC membrane detachment during deoxygenation by measuring the change of RBC tank-treading frequency as a function of PO_2. Tank-treading motion of a RBC, which normally occurs in a shear flow, refers to the rotation of the RBC membrane around the cell body. The frequency of such motion is mainly determined by the applied shear rate, viscosity of the suspending solution, and the membrane-cytoskeletal interaction. Therefore, at a constant shear rate and medium vicosity, RBCs with disrupted membrane-cytoskeletal interactions are expected to have an increased tank-treading frequency. Figure 3-8A showed the microfluidic setup where a microfluidic channel with a constriction (w_c = 20 µm and h = 38 µm) was used to induce RBC tank-treading motion in flow. Human RBCs attached with microspheres (1 µm, polystyrene) were injected to the microfluidic channel and the tank-treading frequency (f (s^{-1})), which is the inverse of the orbital period (the time for the microbead moving along with the RBC membrane for one revolution), was measured using a high-speed camera. In addition, we varied the length of the channel prior to constriction to achieve the exposure time of reduced PO_2, t_{total}, at 18 ± 4 ms, 192 ± 30 ms and 377 ± 11 ms, respectively. PO_2

inside the channel was calibrated as described previously. As shown in Figure 3-8B, the normalized tank-treading frequency, $f\,(s^{-1}) / f\,(s^{-1})_{34\ \mathrm{mmHg}}$, where $f\,(s^{-1})_{34\ \mathrm{mmHg}}$ is the tank-treading frequency at $PO_2 = 34$ mmHg, was independent on PO_2 changes when t_{total} was 18 ± 4 ms. However, when t_{total} was increased to 192 ± 30 ms and 377 ± 11 ms, $f\,(s^{-1}) / f\,(s^{-1})_{34\ \mathrm{mmHg}}$ increased linearly with the decrease of PO_2. When t_{total} = 192 ± 30 ms, tank treading frequency changed linearly with PO_2 and was more sensitivity to PO_2 changes when the viscosity was higher (Table 3-2).(η = 1.36 mPa·s: n = 80 RBCs, 3 subjects, 3 trials, $f / f_{34\mathrm{mmHg}} = -0.0043 \times PO_2\ (\mathrm{mmHg}) + 1.1326$, $R^2 = 0.839$; η = 2.61 mPa·s: n = 116 RBCs, 3 subjects, 3 trials, $f / f_{34\mathrm{mmHg}} = -0.0062 \times PO_2\ (\mathrm{mmHg}) + 1.2036$, $R^2 = 0.959$; η = 4.66 mPa·s: n = 120 RBCs, 3 subjects, 3 trials, $f / f_{34\mathrm{mmHg}} = -0.0115 \times PO_2\ (\mathrm{mmHg}) + 1.3509$, $R^2 = 0.874$). The same trend was applied when t_{total} was increased to 377 ± 11 ms (η = 1.36 mPa·s: n = 129 RBCs, 3 subjects, 3 trials, $f / f_{34\mathrm{mmHg}} = -0.0072 \times PO_2\ (\mathrm{mmHg}) + 1.2253$, $R^2 = 0.894$; η = 2.61 mPa·s: n = 160 RBCs, 3 subjects, 3 trials, $f / f_{34\mathrm{mmHg}} = -0.0117 \times PO_2\ (\mathrm{mmHg}) + 1.3677$, $R^2 = 0.920$; η = 4.66 mPa·s: n = 120 RBCs, 3 subjects, 3 trials, $f / f_{34\mathrm{mmHg}} = -0.0141 \times PO_2\ (\mathrm{mmHg}) + 1.4461$, $R^2 = 0.924$).

Table 3-2. Dimensions of microfluidic channels in use for human RBC measurement

Exposure time	**Viscosity**	**Fitting correlations**
t_{total} = 192 ± 30 ms	1.36 mPa·s	$f / f_{34\mathrm{mmHg}} = -0.0043 \times PO_2\ (\mathrm{mmHg}) + 1.1326$
t_{total} = 192 ± 30 ms	2.61 mPa·s	$f / f_{34\mathrm{mmHg}} = -0.0062 \times PO_2\ (\mathrm{mmHg}) + 1.2036$
t_{total} = 192 ± 30 ms	4.66 mPa·s	$f / f_{34\mathrm{mmHg}} = -0.0115 \times PO_2\ (\mathrm{mmHg}) + 1.3509$

Exposure time	**Viscosity**	**Fitting correlations**
t_{total} = 377 ± 11 ms	1.36 mPa·s	$f / f_{34\mathrm{mmHg}} = -0.0072 \times PO_2\ (\mathrm{mmHg}) + 1.2253$
t_{total} = 377 ± 11 ms	2.61 mPa·s	$f / f_{34\mathrm{mmHg}} = -0.0117 \times PO_2\ (\mathrm{mmHg}) + 1.3677$
t_{total} = 377 ± 11 ms	4.66 mPa·s	$f / f_{34\mathrm{mmHg}} = -0.0141 \times PO_2\ (\mathrm{mmHg}) + 1.4461$

The sensitivity of the tank-treading frequency to PO_2 changes was also increased as the increase of t_{total} and medium viscosity (Figure 3-8C), strongly suggesting the disrupted membrane-cytoskeletal interaction during sustained deoxygnation. Furthermore, at each PO_2 levels, RBC tank-treading frequency increased as the increase of the viscosity of the RBC susepension, consistent with previous literature findings [16]. The results demonstrate a PO_2-regulated RBC tank-treading motion that depends on both the exposure time of reduced PO_2 and medium viscosity and thus support evidently the disrupted RBC membrane-cytoskeletal interaction during deoxygenation.

To further test whether PO_2-regulated RBC capillary velocity is also affected by the duration of reduced PO_2, we measured RBC capillary velocity using another series of microfluidic capillaries with controlled t_{total}. The results as shown in Figure 3-8D demonstrated that the normalized RBC velocity, $v_{0\mathrm{mmHg}}/v_{34\ \mathrm{mmHg}}$ where $v_{0\mathrm{mmHg}}$ and $v_{34\ \mathrm{mmHg}}$ were the RBC velocity at PO_2 = 0 mmHg and PO_2 = 34 mmHg, respectively, was independent on t_{total} for transgenic mice with modified band 3-deoxyHb interaction (mRBC-del 1-11 and mRBC-del 12-23). In contrast, the normalized RBC velocity of human RBCs (hRBC-WT), transgenic mouse RBCs with “humanized” band 3 (mRBC-subst 1-35), and wild type mouse RBCs (mRBC-WT) increased with the increase of t_{total} and reached a maximum when t_{total} was about 351.3 ± 25 ms, 913.4 ± 63 ms and 955.1 ± 57 ms, respectively. Beyond such threshold of t_{total}, RBC capillary velocity became independent of PO_2 changes. These data thus show that not only does the t_{total} affect PO_2-

regulated RBC capillary velocity and but also the existence of a critical t_{total} beyond which RBC capillary velocity is independent on PO_2 changes. Furthermore, the smaller critical t_{total} of human RBCs and mouse RBCs with humanized band 3 (mRBC-subst 1-35) comparing to that of wild type mouse RBCs implies a fast response time of human RBCs to PO_2 changes, which is further evidenced by the shortest *in vivo* onset time of RBC capillary velocity increase in mRBC-subst 1-35 (Figure 3-6H).

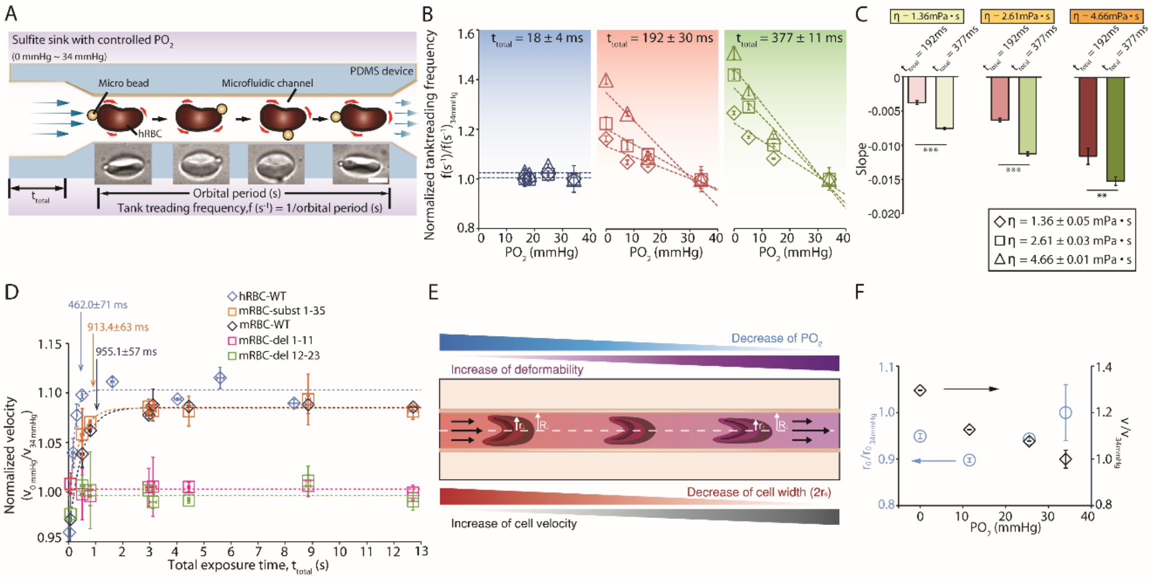

Figure 3-8. Dynamics of PO_2-regulated RBC velocity in capillary. (A) Schematics of experimental setup for *ex vivo* analysis of RBC tank treading frequency at reduced PO_2. (B) Effect of total exposure time of reduced PO_2 (t_{total}) on tank treading frequency of human RBCs, f (s^{-1}). Dextran was added to increase the viscosity of RBC suspension (1.36 mPa·s, 2.61 mPa·s, and 4.66 mPa·s). (C) Magnitude of slope comparison under different viscosities. (D) Effect of total exposure time of reduced PO_2 (t_{total}) on RBC velocity in microfluidic capillary. (E) Schematics of the relation between PO_2, RBC deformability, and capillary velocity. RBCs are more deformable at reduced PO_2 and thus have a smaller cell width ($2r_0$) when flowing in a capillary with a diameter of $2R_0$. As a result, the gap distance between the surface of RBC and the capillary wall (R_0-r_0) increases, leading to a high RBC velocity. (F) Experimental measured changes of RBC width r_0 and RBC velocity v as a function of PO_2.

Last, we evaluate the correlation between RBC capillary velocity and RBC deformability by analyzing the changes of the RBC width r_0 in capillary as a function of PO_2 (Figure 3-8E). According to the classical Bretherton scaling for a long bubble flowing in a microchannel, the normalized gap distance between the channel wall and the surface of the bubble, $(R_0 - r_{0\ bubble})/R_0$ where R_0 and $r_{0\ bubble}$ is the radius of the channel and the bubble respectively, is proportional to $Ca^{2/3}$ where $Ca = \frac{\mu v}{\sigma}$ is the capillary number, μ is viscosity, v is velocity and σ is surface tension. In the case of RBCs, if we assume the membrane tension E on RBCs is uniform, Ca can be expressed as $Ca = \frac{\mu v}{E}$. Thus, a more deformable RBC membrane with a small E, e.g., at reduced PO_2, will lead to a large Ca, and consequently an increased gap distance. Given the channel radius R_0 is constant, increased gap distance implies a decreased RBC width r_0 in the channel. Indeed, when we measured the change of cell width as a function of PO_2, the normalized cell width, $r_0 / r_{0\ 34mmHg}$, where $r_{0\ 34mmHg}$ is the cell width at PO_2 = 34 mmHg decreased as the decrease of PO_2 (Figure 3-8F), supporting the proposed Bretherton model. Furthermore, such increase of gap distance due to increased RBC deformability would reduce the shear stress acting on RBCs and consequently result in an increased RBC capillary velocity at a constant pressur drop. We calculated the shear stress using lubrication approximation and showed that the non-dimensional form of RBC capillary velocity can be written as

$$\overline{v_0} = v_0 \frac{\mu}{R_0^2}\left(-\frac{dp}{dx}\right)^{-1} = \left(\frac{r_0}{R_0}\right)^2 ln\frac{R_0}{r_0} - \frac{1}{4}\left[1 - \left(\frac{r_0}{R_0}\right)^2\right],$$

which only depends on the ratio of r_0/R_0. Therefore, it is likely that, with the decrease of PO_2, RBCs become more deformabile due to the deoxyHb-band 3 and band 3-cytoskeletal interactions, resulting in a decreaed cell width inside the capillary, which in turn increases the gap distance between the cell and the channel wall and consequently inceases its capillary velocity.

3.3.5 Discussion

Recent studies have revealed that functional hyperemia is initiated in capillary [64, 65] and RBCs themselves can act as oxygen-sensing regulators to control capillary RBC velocity in response to local PO_2 changes. However, the underlying mechanisms of how PO_2 could modulate RBC velocity in capillary are not clear. Experimental findings presented here implied that deoxyHb-band 3 interaction in RBCs is the molecular switch that responds to local PO_2 changes and controls RBC deformability and consequently RBC capillary velocity. DeoxyHb-band 3 interaction occurs at reduced PO_2 and causes a transient rupture of the band 3-ankyrin bridge between the RBC membrane and spectrin/actin cytoskeleton, resulting in weakened membrane-cytoskeletal interactions during deoxygenation [21, 51-53]. Such compromised interactions are expected to lead to increased RBC deformability and capillary velocity. Evidently, we showed that 1) while *ex vivo* capillary velocity and deformation of RBCs from WT mice exhibited a linear relation with local PO_2 changes, RBCs from transgenic mice that had enhanced or weakened deoxyHb-band 3 interaction showed PO_2-independennt changes of capillary velocity and deformation. RBCs with enhanced deoxyHb-band 3 interaction showed higher capillary velocity and deformability comparing to RBCs that had weakened deoxyHb-band 3 interaction. 2) Consistent with *ex vivo* results, *in vivo* cerebral capillary hyperemia in WT mice but not transgenic mice that had RBCs with enhanced or weakened deoxyHb-band 3 interaction was dependent on local PO_2 changes. 3) RBCs from WT mice and human treated biochemically to modify the deoxyHb-band 3 and band 3-ankyrin interactions showed corresponding PO_2-regulated capillary velocity and deformation. 4) RBC membrane tank-treading frequency increased linearly with the decrease of PO_2 and the longer the PO_2 exposure time, the higher the tank-treading frequency was, highlighting the occurrence of membrane-cytoskeletal detachment during deoxygenation. Collectively, these sets of data indicate that, in response to local PO_2 changes, RBCs can modulate membrane-cytoskeletal interactions via deoxyHb-band 3 association, and consequently control RBC deformability and capillary velocity.

It is important to note that there is a significant amount of Hb (~ 270, 000, 000 copies) but a limited number of band 3 (~1,200,000 copies) per RBC. As a result, only ~ 0.4% Hb will be available to bind band 3 during deoxygenation and thus deoxyHb-band 3 interaction will unlikely affect the O_2 delivery in RBCs. Furthermore, because deoxygenation starts to occur near the cell membrane when PO_2 decreases, Hbs that are in close proximity to the cell membrane will be deoxygenated first and bind band 3. Considering a simplified one-step binding reaction between of deoxyHb and band 3, the equilibrium binding constant, K_e, is determined by the ratio of the on-rate constant k_{on} and the off-rate constant k_{off}, $K_e = {k_{on}}/{k_{off}}$. In the case of mRBC-del 1-11 where deoxyHb-band 3 interaction is enhanced by deleting the inhibitory residues 1-11 on band 3, K_e increases due to the decrease of k_{off}. In contrast, K_e decreases due to the decrease of k_{on} in mRBC-del 12-23 where deoxyHb-band 3 interaction is weakened by deleting the deoxyHb binding site (residues 12-23) on band 3. Because deoxyHb sterically displaces ankyrin upon binding to band 3, the stronger the deoxyHb-band 3 interaction is (e.g., larger K_e), the more likely the band 3-ankryin bridge is disrupted, and consequently RBCs become more deformable.

In addition, we note that RBC deformability and capillary velocity are independent of PO_2 when deoxyHb-band 3 interaction is either weakened by deleting the deoxyHb binding residues 12-23 or enchanced by deleting the inhibitory residues 1-11 on band 3. It is understandable that RBC's deformability and capillary velocity do not respond to PO_2 changes when the deoxyHb binding site on band 3 is deleted, but why there are no PO_2-dependent responses even when the deoxyHb-band 3 interaction is enhanced? As discussed previously, the amount of deoxyHb that binds to band 3 only counts ~0.4% of the entire intracellular Hb and most of them likely come from Hbs that are close to the cell membrane during deoxygenation. Thus, such a small amount of Hb will require tiny decrease of PO_2 to become deoxygenated and then bind to band 3. In the case of WT RBCs, the binding rate at this early stage is slow due to the presence of the inhibitory residues 1-11 on band 3. With the further decrease of PO_2, more and more deoxyHb are available and the binding rate increases accordingly, exhibiting a PO_2 dependent deoxyHb-band 3 interaction and thus the observed PO_2-regulated RBC deformability and capillary velocity. In the case of enhanced deoxyHb-band 3 interaction where the inhibitory residues 1-11 on band 3 are deleted, however, the deoxyHb-band 3 binding at the initial stage of deoxygenation is fast and strong and deoxyHb produced from further PO_2 decrease do not contribute to the binding process anymore, and thus present PO_2-independet RBC responses. RBCs treated with PEP with decreased amount of deoxyHb available to bind band 3 highlight again the decreased rate constant (kinetics) such that the sensitivity to PO2 changes decreases. Similarly, when such regulation was reduced in Pi treated RBCs, deoxyHb near the cell mebrane can bind band 3 readly duing deoxygnation and thus also decrease the sensitivity to PO_2 changes.

Indeed, the fact that there is a critical RBC response time in WT RBCs beyond which RBC capillary velocity do not depend on PO_2 anymore further highlights the discussed kinetic process: when the deoxygenation process is close to complete (~400 ms), the deoxyHb-band 3 interaction reaches an equilibrium and thus RBC capillary velocity does not change with PO_2. Note that the 1s of RBC response time to PO_2 changes is close to RBC capillary transit time in the brain, further emphasizing the regulatory roles of RBC in control its velocity in capillary. In addition, human RBCs have the shortest response time to PO_2 changes, followed by RBCs from transgenic mice with humanized band 3 (mRBC-subst 1-35), and then WT mouse RBC, suggesting species-specific deoxyHb-band 3 interaction. Lastly, it should be noted that volume changes of RBCs will affect the measured RBC velocity and thus RBC volume was assumed to be constant during the capillary velocity measurement. However, it is known that PO_2 can also regulate cation flux in RBCs and thus controls RBC volume. In addition, the mechanosensing ion channels on RBCs, Piezo1 will be activated due to the significant deformation in capillary and plays a role in regulating ion flux and cell volume. Thus, it is likely that deoxyHb-band 3 interaction mediated RBC capillary velocity contributes partially to the observed PO_2-regulated RBC capillary velocity and other factors that regulate RBC volume also exist.

3.4 Conclusion

In summary, we demonstrate that RBCs are the active players in regulating capillary hyperemia by controlling the band 3-deoxygen interaction/band 3-ankyrin interaction at different PO_2 levels. Such red cell properties change at different PO_2 levels leads to red cell deformation and capillary velocity change, which facilitate capillary hyperemia. The results suggest a novel yet effect approach to manipulate functional hyperemia by controlling red cell properties, without the input from neuron, astrocyte or the unit. A possible therapeutic approach to treat neurodegenerative disease, stroke, etc.

4. PIEZO1 REGULATES MECHANO-TRANSDUCTIVE RELEASE OF ATP FROM HUMAN RBCS

Piezo proteins (Piezo1 and Piezo2) are recently identified mechanically activated cation channels in eukaryotic cells and associated with physiological responses to touch, pressure, and stretch. In particular, human RBCs express Piezo1 on their membranes, and mutations of Piezo1 have been linked to hereditary xerocytosis. However, physiological functions of Piezo1 on normal RBCs remain poorly understood. Here, we show that Piezo1 regulates mechanotransductive release of ATP from human RBCs by controlling the shear-induced calcium (Ca^{2+}) influx. We find that, in human RBCs treated with Piezo1 inhibitors or having mutant Piezo1 channels, the amounts of shear-induced ATP release and Ca^{2+} influx decrease significantly. Remarkably, a critical extracellular Ca^{2+} concentration is required to trigger significant ATP release, but membrane-associated ATP pools in RBCs also contribute to the release of ATP. Our results show how Piezo1 channels are likely to function in normal RBCs and suggest a previously unidentified mechanotransductive pathway in ATP release. Thus, we anticipate that the study will impact broadly on the research of red cells, cellular mechanosensing, and clinical studies related to red cell disorders and vascular disease.

4.1 Introduction

Mechanical stress-induced deformation of human RBCs plays important pathophysiological roles in oxygen delivery, blood rheology, transfusion, and malaria [66-69]. Recent studies show that, in response to shear-induced stretch, RBCs release ATP [17, 70-73], suggesting the existence of mechanotransductive pathways in RBCs. Most importantly, RBCs participate in vascular signaling through the mechanotransductive release of ATP and contribute to the control of microvascular tone [22, 23]. The released ATP from RBCs, for example, binds and activates the purinergic G coupled protein receptors (P_{2Y} receptors) on vascular endothelial cells and induces the synthesis and release of nitric oxide [74, 75], a well-known vasodilator as illustrated in Figure 4-1 [91]. Moreover, impaired release of ATP from RBCs has been linked to diseases, such as type II diabetes and cystic fibrosis [76, 77]. Given that RBCs experience shear stresses continuously during the circulation cycle and that the released ATP plays a central role in vascular pathophysiology, understanding of the mechanotransductive release of ATP from RBCs will provide not only fundamental insights to the roles of RBCs in vascular homeostasis but also, potential therapeutic strategies for red cell dysfunction and vascular disease.

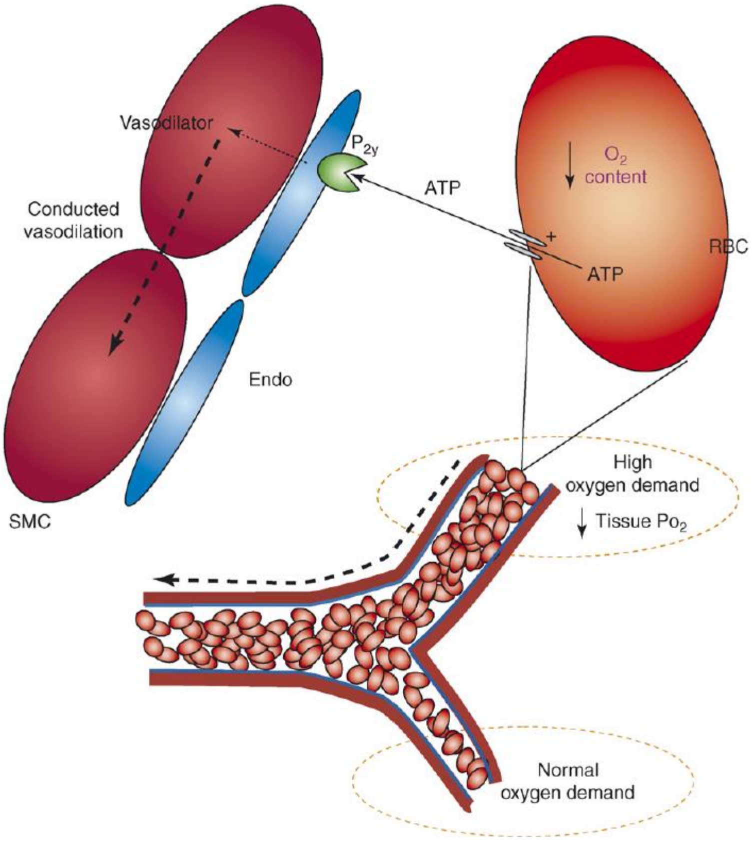

Figure 4-1. Illustration showing the entrance of RBCs into tissues. RBCs provide oxygen supply as well as ATP. As long as P_{2Y} receptors bind with ATP, vasodilation occurs. [91]

Previous studies have shown that the addition of chemicals that stiffen RBC membranes decreases the amount of ATP released [17, 78], indicating that deformation of the cell membrane is a necessary trigger. In addition, biological mediators, such as cystic fibrosis transmembrane conductance regulator (CFTR) and pannexin-1 hemichannels, are involved in the release pathways of mechanotransductive ATP release from RBCs [17, 76, 79, 80]. Inhibition of CFTR leads to an impaired ATP release from deformed RBCs [76]. Recent studies, including our previous findings, suggest that interactions between membrane-associated actin and CFTR play important roles in the mechanotransductive ATP release from RBCs [17, 79]. Pannexin-1, however, is a channel-forming protein and has been suggested as a mechanosensing ATP release channel [80]. Under osmotic stress, for example, ATP released from RBCs was attenuated by carbenoxolone, a highly effective pannexin channel blocker, suggesting that pannexin-1 might be one of the conductance channels responsible for the mechanotransductive release of ATP (Figure 4-2) [80]. Although progress has been made in understanding mechanotransductive ATP release from RBCs, many questions remain about the signal transduction pathways. For example, how does mechanical force transduce signals to ATP release channels? Are there any stretch-activated ion channels on RBCs that may sense mechanical forces and activate ATP release? If so, are there any secondary messengers that could be generated by mechanical stimuli and regulate ATP release?

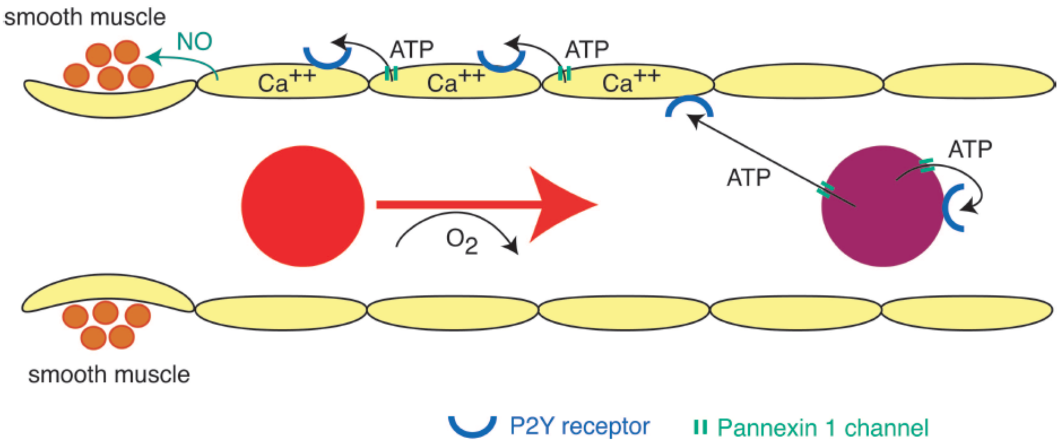

Figure 4-2. Scheme depicting a possible path way of blood flow regulation through pannexin 1 channels. [80]

Piezo proteins (Piezo1 and Pizeo2) are recently identified mechanically activated cation channels in mammals [58, 81] and can be fully activated without involvement of additional proteins [81, 82]. Piezo-induced cationic currents were first observed in the Neuro2A mouse cell line, but subsequent studies have shown that Piezo proteins are able to mediate mechanically activated cationic currents in a variety of cell types, including endothelial cells [83, 84] and neuronal stem cells [85]. In particular, mature RBCs and erythroid progenitor cells express Piezo1 on their membranes [86], and mutations in the Piezo1 channels on mature RBCs are associated with hereditary xerocytosis (HX) [87, 88], a disease that is characterized by RBC dehydration and hemolytic anemia. To date, however, the physiological roles of Piezo1 in healthy RBCs remain poorly understood [88], and whether Piezo1 participates in the mechanotransductive release of ATP from RBCs is completely unknown. We hypothesize that Piezo1 controls shear-induced Ca^{2+} influx in RBCs and participates in the regulation of mechanotransductive release of ATP from RBCs. To test the hypothesis, we have implemented a microfluidic approach to control the shear-induced deformation of RBCs in flow and identify the regulatory roles of Piezo1 in shear-induced ATP release and Ca^{2+} influx in RBCs. Additionally, we show the correlation between stretch-evoked Ca^{2+} influx and ATP release from RBCs and reveal a threshold concentration of extracellular Ca^{2+} necessary for triggering shear-induced ATP release. Lastly, functional roles of membraneassociated ATP pools and potential ATP release channels in the shear-induced ATP release are investigated, and a model of mechanotransductive ATP release from RBCs is proposed.

4.2 Experimental methods

4.2.1 Microfluidic fabrication and experimental setup

Microfluidic devices were fabricated out of PDMS (Slygard 184) using the standard soft lithography technique. Three-inch silicon wafers (University Wafers) were patterned using epoxy-based negative photoresist (SU-8) (Microchem) photoresist, and then, PDMS (10:1 curing ratio) was cast on the wafer molds. For each experiment, 1.0 mL 10% (vol/vol) RBCs suspension was loaded into a syringe (Hamilton), which is connected to a polyethylene (PE 20) tube by a syringe needle (27 gauge). The other end of the tube was inserted into the inlet of microfluidic devices. The syringe was placed onto a syringe pump (Harvard Apparatus Phd Ultra; Harvard Apparatus), and suspension was flowed at a rate of 3.0 µl/min.

4.2.2 RBC preparation

Human RBCs were drawn from healthy donors and used on the same day of experiments. To treat RBCs with Piezo1 inhibitors, 10% (vol/vol) RBCs were incubated with 10 µM GsMTx4 (Peptides International, Inc.), 30 µM Gd^{3+} (Sigma), or ruthenium red (Sigma) in physiological salt solution (PSS) at 37 °C for 30 min. To inhibit CFTR and/or pannexin-1 channels on RBCs, 10% (vol/vol) RBCs were incubated with 50 µM glibenclamide and/or carbenoxolone at 37 °C for 30 min. Glibenclamide (Sigma) was prepared by following the protocol in ref. [76] and diluted from a 10 mM stock solution to 50 µM in PSS. Carbenoxolone was diluted from 1.0 mM stock solution to 50 µM in PSS. All treated cells were washed with a PBS solution three times and resuspended into the luciferase-luciferin (LL) solution for ATP measurements. RBCs with FAM38A mutations of Piezo1 channels were obtained from patients with HX at the University of Rochester Medical Center under a material transfer agreement.

4.2.3 LL solution preparation

PSS was prepared with 4.7 mM KCl, 2.0 mM $CaCl_2$, 1.2 mM $MgSO_4$, 140.5 mM NaCl, 21 mM Tris (hydroxymethyl)aminomethane, 11.1 mM dextrose, and 1 mg/ml BSA. The pH of the solution was adjusted to 7.4. D-luciferin and firefly luciferase were purchased from Sigma. LL solution was prepared by adding 1.7 mg D-luciferin and 100 μl firefly luciferase (1.0 mg/ml in PSS) into 5.0 ml PSS. PSS with different Ca^{2+} concentrations was prepared by dissolving a proper amount of $CaCl_2$. The resulting solution was then titrated using 100 mM EDTA. Calcium concentration at the equivalence point was calculated using the Ca^{2+}-EDTA binding constant $K_d = 10^{10.65}$ assuming 1:1 binding of Ca^{2+}: EDTA (Y^{4-}). The fraction of EDTA (Y^{4-}) is used as 3.8×10^{-4} at pH 7. Calcium-free buffer was obtained by preparing PSS without adding $CaCl_2$ and including 1.5 mM EDTA. A Ca^{2+}-free firefly luciferase solution (1.0 mg/ml) was prepared by using calcium-free PSS. ATP-sodium salt solution was prepared in 100 μM stock solution using DI water, and then, the stock was diluted into PSS to generate specific concentrations for calibration experiments. Both LL and ATP-sodium salt solutions were prepared on the day of use. All chemicals, proteins, and enzymes were purchased from Sigma without additional purification.

4.2.4 RBC deformability measurements

To measure the deformability of RBCs, we diluted RBCs at ~1.0% (v/v) in PSS and flowed the solution through another microfluidic constriction channel. The constriction channel dimensions used for cell deformability were 20 μm in width, 100 μm in length, and 30 μm in height. The cells were injected at a flow rate of 3.0 μl/min, and high-speed videos are captured with a high-speed camera (Phantom M120; Vision Research). The videos were recorded at 1,900 frames per second with a resolution of 1,216 × 700. The videos were analyzed using Image J to determine the lengths of cells in pixels.

4.2.5 ATP measurement

We used a microfluidic channel with a constriction for shear-induced ATP measurement. The width of the channel before and after the constriction is 100 μm; the constriction is 20-μm wide (w_c) and 800-μm long (l_c). The height of the channel is uniformly 30 μm. Bioluminescent light was measured at different positions along the microfluidic channel by using a 63× oil objective on a microscope (Leica DMI 6000B; Leica). This objective has lower magnification than the one that we used in previous studies, resulting in a larger field of view. This large field of view has the consequence that sensitivity is increased slightly, because we are gathering light from a larger area, but temporal resolution is decreased, because cells remain in the field of view for longer periods of time. This lower temporal resolution results in an ATP release profile that is slightly different in appearance than that reported in previous studies [17]. The emitted light is passed to the photomultiplier detector, which is connected to the microscope by a C mount as a part of the separate photo detection system (RatioMaster; Photon International Technology). The time of release of ATP is then obtained by taking advantage of the space–time equivalence in time-invariant flows in microfluidic channels. All experiments were performed at room temperature (25 °C) and inside a dark room.

4.2.6 Ca^{2+} measurement

The same microfluidic device used to measure ATP release was used to measure shear-induced Ca^{2+} influx. RBCs at 10% (v/v) were loaded with Fluo-4 by incubating the cells at 37 °C for 30 min in 5.0 μM Fluro-4 AM Dye (Life Technologies). Cells were then washed three times using a physiological salt solution and injected into the microfluidic device. Cells were excited at 488 nm with a monochromator light source (RatioMaster; Photon International Technology), and the emitted light intensity was measured with the photon detection system (RatioMaster; Photon International Technology) using a GFP filter. Images of cells stretched by fluid shear were taken with a digital charge-coupled device (CCD) (Hamamatsu ORCAR2; Hamamatsu). A 75-W Xenon Lamp (Leica) was used to excite the cells, and software exposure settings were kept the same throughout each experiment.

4.3 Results and discussion

4.3.1 Inhibition of Piezo1 impairs shear-induced ATP release and Ca^{2+} influx in human RBCs

We have developed a microfluidic strategy to investigate the effects of Piezo1 on shear-induced ATP release and Ca^{2+} influx in human RBCs. The principle of the strategy is similar to our previously shown approach [17]. Briefly, a microfluidic channel with a constriction (l_c = 800 μm; w_c = 20 μm) is used to control the magnitude and duration of increased shear stress in flow, and the dynamics of shear-induced ATP release from human RBCs are studied with millisecond resolution. In particular, healthy human RBCs treated with Piezo1 inhibitors (gadolinium (Gd^{3+}) [58], ruthenium red [58], or the peptide *Grammostola spatulata* mechanotoxin 4 (GsMTx4) [82, 89]) or loaded with a Ca^{2+}-sensitive fluorescence dye (Fluo-4) were injected into the microfluidic channel at a constant flow rate (3 μl/min) (Figure 4-3A). The flow rate is chosen such that RBCs flowing inside the constriction channel experience a physiological level of shear stress comparable with that in arterioles [90, 91] (i.e., calculated average shear stress is ∼4 Pa in the constriction channel) (Table 4-1). In addition, the flow velocity in the channel does not change with time, and thus, the flow in the channel is steady. Because space and time are interchangeable for a steady flow, we are able to apply increased shear and measure the release of ATP and Ca^{2+} influx with millisecond resolution. The average flow velocity in the constriction channel (v_c), for example, is ∼0.083 m s^{-1}; the duration (t_c) of increased shear is, thus, ∼9.6 ms ($t_c = l_c/v_c$). To measure the amount of released ATP, we used the Luciferase-ATP bioluminescent reaction and detected photon emission rate by using a photon-counting photomultiplier tube (PMT).

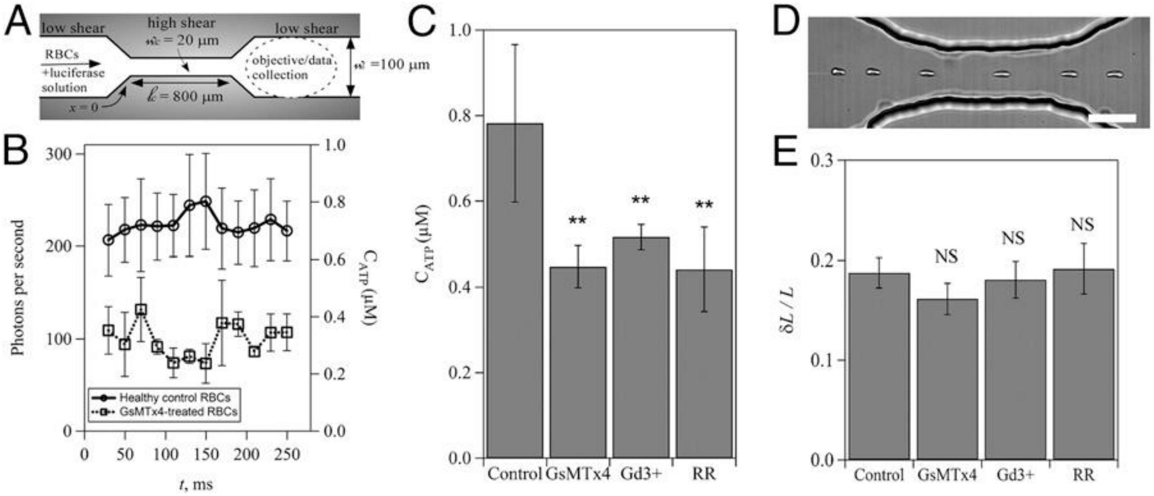

Figure 4-3. Inhibition of Piezo1 impairs shear-induced ATP release from human RBCs. (A) Schematic of the microfluidic setup for measuring shear-induced ATP release from RBCs (not to scale). Note that $x = 0$ indicates the onset of increased shear. (B) Representative measurements of the photon emission rate resulting from the reaction between luciferase/luciferin and ATP for healthy control and GsMTx4-treated RBCs; $t = 0$ ms corresponds to the position of $x = 0$ in A. Note that GsMTx4 is a peptide that has been used to inhibit mechanically activated Piezo1 channels. The error bars are reported as the SDs of the mean (n = 11 and 4 for control and treated RBCs, respectively). (C) Average concentration of released ATP from control and Piezo1 inhibitor-treated RBCs. **: $P < 0.01$. (D) Superimposed series of time-lapse images showing the deformation of an individual RBC passing through a short constriction ($l_c = 100$ μm; $w_c = 20$ μm). (Scale bar: 20 μm.) (E) Normalized change of RBC length (measured in the flow direction) for cells passing through the short constriction shown in D ($\delta L/L = L_{stretched} - L_{original} = L_{original}$). Data were averaged from more than 30 cells for each sample. NS, not significant; RR, ruthenium red.

Average concentration of released ATP was obtained based on an independently measured calibration curve. The magnitude of shear-induced Ca^{2+} influx (i.e., the fluorescence intensity of Fluo-4) was measured by using the PMT or a fluorescence camera. In addition, we used a high-speed camera to track the deformation of individual cells.

Table 4-1. Calculation of average shear stress in the constriction channe

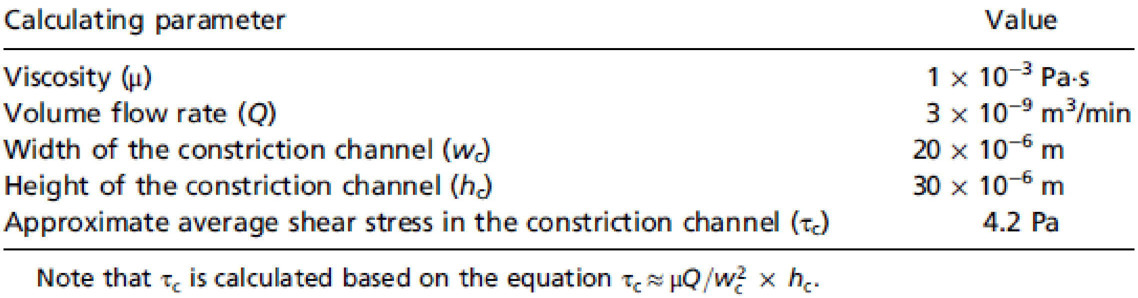

Calculating parameter	Value
Viscosity (μ)	1×10^{-3} Pa·s
Volume flow rate (Q)	3×10^{-9} m^3/min
Width of the constriction channel (w_c)	20×10^{-6} m
Height of the constriction channel (h_c)	30×10^{-6} m
Approximate average shear stress in the constriction channel (τ_c)	4.2 Pa

Note that τ_c is calculated based on the equation $\tau_c \approx \mu Q / w_c^2 \times h_c$.

We showed that the amount of released ATP from GsMTx4-treated RBCs (10% v/v) was approximately twofold lower than that from untreated, healthy control RBCs (Figure 4-3B). In addition, control RBCs showed a peak of maximum ATP release between 125 and 150 ms after the constriction, whereas treated RBCs had no such releasing pattern. Decreased ATP release was also observed when RBCs were treated with other Piezo1 inhibitors (i.e., Gd^{3+} and ruthenium red), strongly suggesting that Piezo1 channels are involved in the regulation of shear-induced ATP release from RBCs (Figure 4-3C). To rule out the possibility that decreased ATP release might arise from the impaired deformability of RBCs on the treatment of Piezo1 inhibitors, we performed a cell deformability study by flowing control and Piezo1 inhibitor-treated RBCs through a short constriction channel (l_c = 100 μm; w_c = 20 μm) (Figure 4-3D). By measuring the change of RBC length using a high-speed camera, we found that there was no significant difference between control RBCs and treated cells (Figure 4-3E), indicating that treatment with Piezo1 inhibitors does not affect RBC deformability.

Inhibition of Piezo1 channels reduces shear-induced Ca^{2+} influx in RBCs at both the single-cell and population levels. Images presented in Figure 4-4A show typical responses of single RBCs to a flow-induced stretch in terms of Ca^{2+} influx. In the experiment, RBCs were loaded with Fluo-4 and immobilized at the bottom surface of the microfluidic channel, where an average wall shear stress was estimated as 3.4 Pa. Shear-induced changes in fluorescence caused by Ca^{2+} influx were recorded using a fluorescence camera. The fluorescence intensity of control RBCs subjected to flow was significantly higher than that of RBCs treated with Piezo1 inhibitors (Figure 4-4B).

At the population level, we flowed Fluo-4–loaded RBCs (10% v/v) through the microfluidic constriction channel ($l_c = 800$ μm; $w_c = 20$ μm) and examined the fluorescence intensity of RBCs before and after the constriction using a photon-counting PMT. Again, a significant increase of fluorescence intensity was observed only when control RBCs were flowing through the constriction channel (Figure 4-4C). In addition, the increase of Ca^{2+} influx occurs right after the constriction and continuously increases along the channel, which is unlike the pattern that we observed for shear-induced ATP release, in which the maximum release of ATP occurs a period after the constriction.

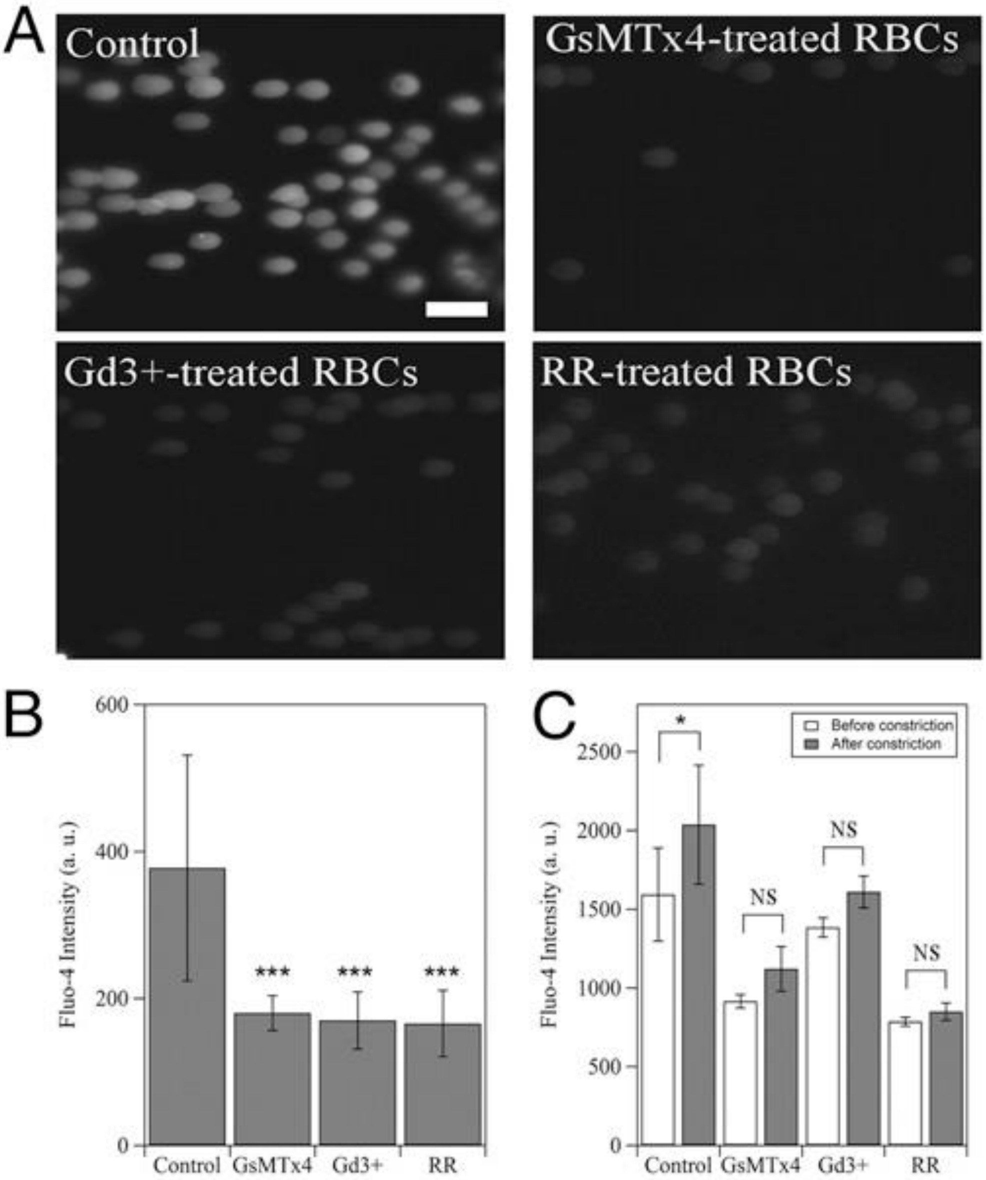

Figure 4-4. Inhibition of Piezo1 reduces shear-induced Ca^{2+} influx in human RBCs. (A) Fluorescence images of Fluo-4–loaded control and Piezo1 inhibitor-treated RBCs stretched by shear in a microfluidic device. Calculated average shear stress is ∼3.4 Pa. (Scale bar: 20 μm.) (B) Average fluorescence intensity of control and Piezo1 inhibitor-treated single RBCs. The error bars are reported as the SDs of the mean (n = 3). ***: $P < 0.001$. (C) Average fluorescence intensity of control and Piezo1 inhibitor-treated RBCs (10% v/v) flowing before and after the constriction channel. The error bars are reported as the SDs of the mean (n = 8 and 3 for normal RBCs and treated RBCs, respectively). NS, not significant; RR, ruthenium red. *: $P < 0.05$.

4.3.2 Shear-induced ATP release from human RBCs depends on Ca^{2+} influx and membrane-associated ATP pools

To identify whether Ca^{2+} influx in RBCs is necessary for shear-induced ATP release, we compared the amount of released ATP from RBCs that were prepared in different concentrations of extracellular Ca^{2+}. Tests on cells labeled with Fluo-4 revealed that the influx of calcium increased in proportion to the extracellular calcium concentration (Figure 4-5). In the absence of external Ca^{2+}, ATP release remained at baseline (Figure 4-6A). The average amount of released ATP remained almost unchanged (~0.34 μM), even when the extracellular Ca^{2+} concentration increased from 0 to 0.5 mM (Figure 4-6B). When the extracellular Ca^{2+} concentration was above 0.5 mM, however, the average amount of released ATP increased significantly and in proportion to the extracellular Ca^{2+} concentration (Figure 4-6B).

This observation indicates the existence of a threshold of extracellular Ca^{2+} concentration required for shear-induced ATP release. We further examined the correlation between shear-induced ATP release and Ca^{2+} influx by using RBCs from patients with HX, which is known to be associated with mutations of Piezo1 channels on RBCs [86-88]. Data in Figure 4-6C and D show that both the amount of released ATP and Ca^{2+} influx from HX RBCs decreased significantly, suggesting that mutant Piezo1 channels impair Ca^{2+} influx and consequently, reduce ATP release.

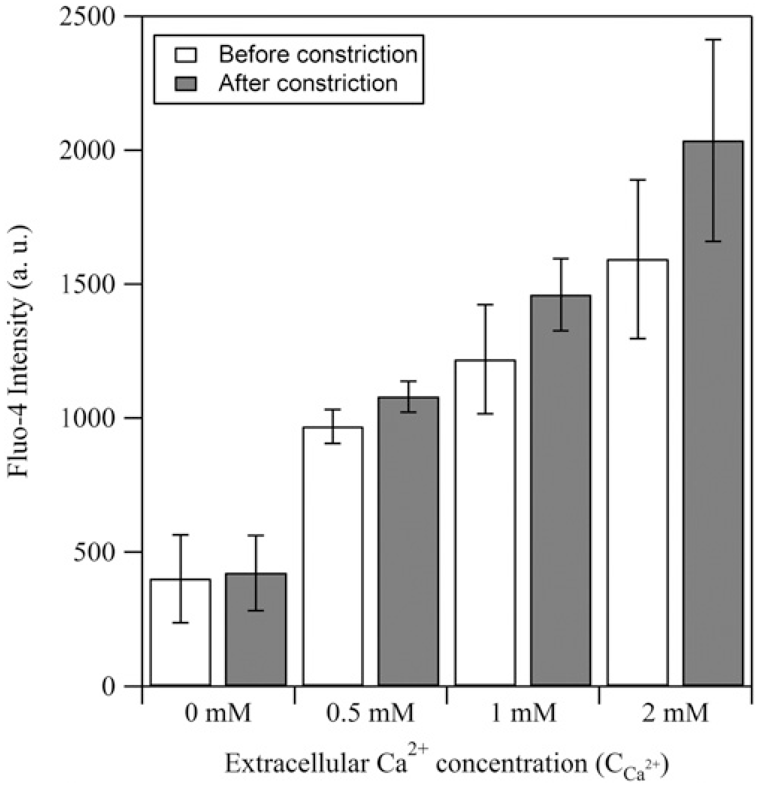

Figure 4-5. Effect of extracellular Ca^{2+} concentration on shear-induced Ca^{2+} influx in RBCs. The error bars are reported as the SDs of the mean (n = 6, 4, 3, and 8 for 0, 0.5, 1, and 2 mM, respectively).

Lastly, we investigated the roles of membrane-associated ATP pools and ATP-releasing channels in shear-induced ATP release from RBCs. Membrane-associated ATP pools in RBCs have been shown to be able to fuel RBC membrane cation pumps, including the Ca^{2+} pumps [92-94]. In particular, it has been suggested that membrane-associated ATP pools supply hypoxia-induced ATP release from RBCs [92].

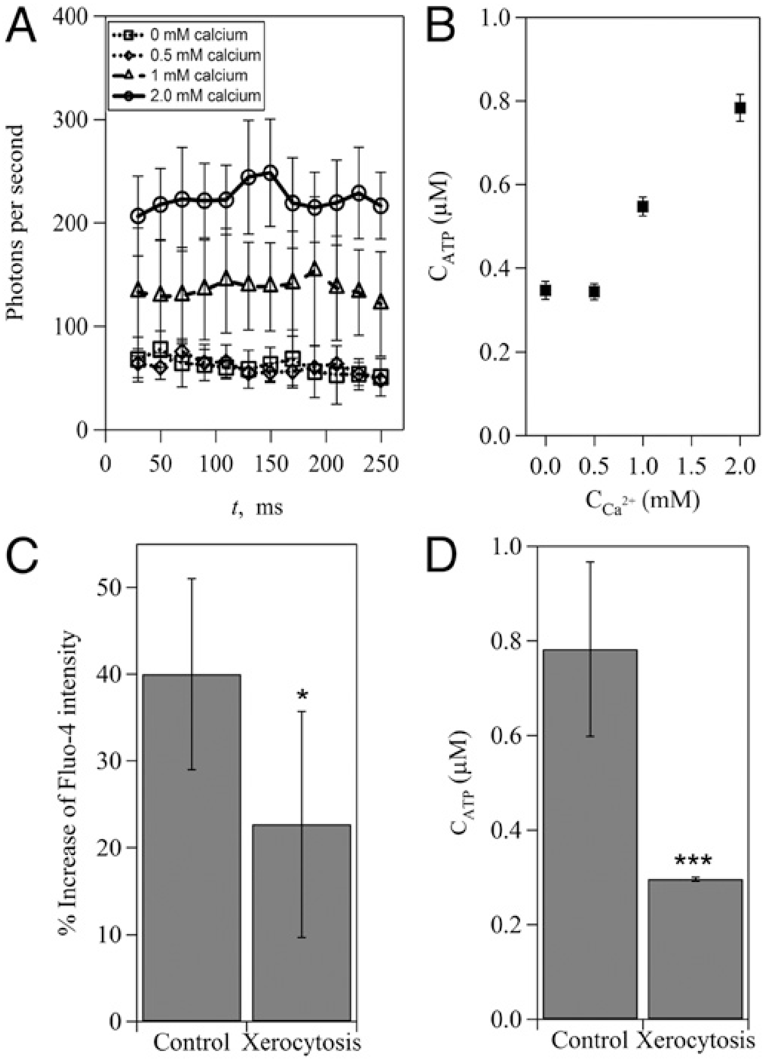

Figure 4-6. Ca^{2+} influx regulates shear-induced ATP release from human RBCs. (A) Measurements of the photon emission rate caused by shear-induced ATP release in solutions with different concentrations of Ca^{2+}. (B) Dependence of shear-induced ATP release on extracellular Ca^{2+} concentrations. (C) Ca^{2+} influx-induced increase of Fluo-4 intensity and (D) shear-induced ATP release from healthy control RBCs and RBCs from patients with xerocytosis. The error bars are reported as the SDs of the mean (n = 11 and 4 for control RBCs and RBCs from patients with xerocytosis, respectively). *: $P < 0.05$; ***: $P < 0.001$.

In our experiment, we measured the shear-induced ATP release from RBCs treated with ouabain, which is known to prevent bulk ATP from entering the ATP pools in RBC ghosts [93]. The results showed that ouabain-treated RBCs have a decreased amount of released ATP compared with control RBCs (Figure 4-7A), implying that limited access to bulk ATP reduces shear-induced ATP release. Meanwhile, the release of ATP from ouabain-treated RBCs reached its maximum at ~100 ms after the onset of increased shear, which is ~50 ms earlier than that of control RBCs. In addition, we performed experiments with the pannexin-1 inhibitor carbenoxolone and the CFTR inhibitor glibenclamide to explore their roles in shear-induced ATP release. The results showed that the amount of released ATP decreases significantly (approximately twofold) in treated RBCs (Figure 4-7B).

Notably, the amount of released ATP from RBCs treated with both carbenoxolone and glibenclamide was not significantly different from RBCs that were treated with either carbenoxolone or glibenclamide alone. These findings indicate that carbenoxolone and glibenclamide do not distinguish between different potential ATP transport pathways. Furthermore, to determine the role of pannexin-1 relative to Piezo1 in terms of ATP release, we treated RBCs with both carbenoxolone and Piezo1 inhibitor GsMTx4 and measured ATP release. The results showed an additional reduced release of ATP (0.29 ± 0.07 μM) (Figure 4-5B) compared with RBCs treated with either carbenoxolone (0.49 ± 0.14 μM) (Figure 4-5B) or GsMTx4 (0.45 ± 0.05 μM) (Figure 4-3C) alone.

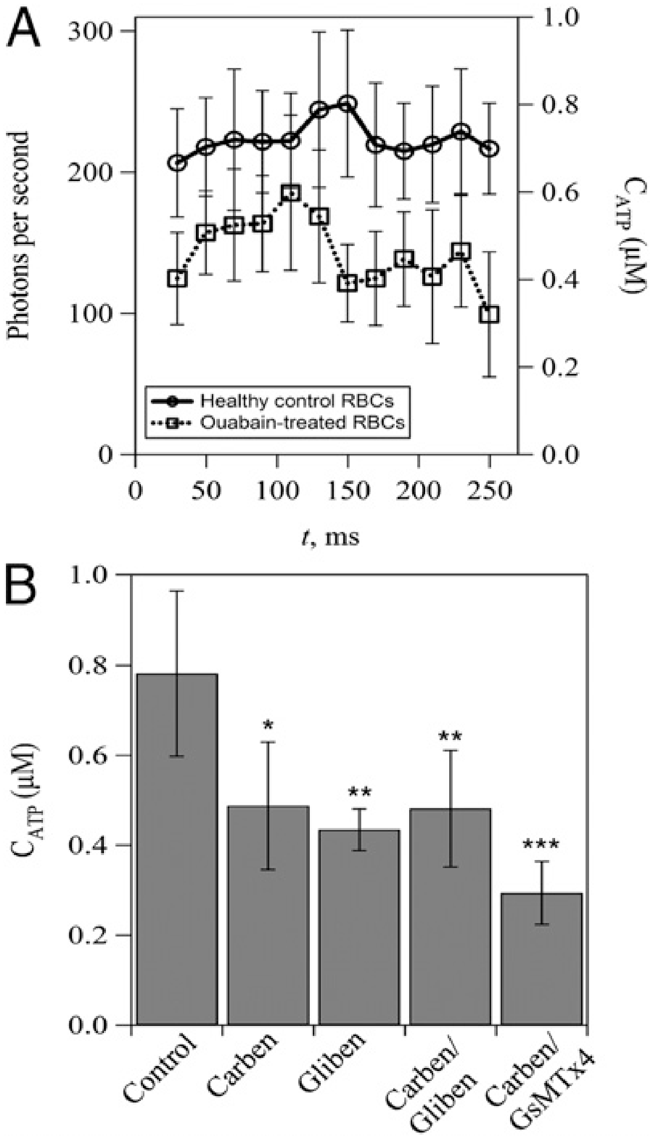

Figure 4-7. Effects of membrane-associated ATP pools and potential ATP-releasing channels on shear-induced ATP release from human RBCs. (A) Effect of ouabain treatment on shear-induced ATP release. Note that ouabain treatment is used to prevent bulk ATP from entering the membrane-associated ATP pools in RBCs. (B) Effect of inhibition of CFTR and/or pannexin-1 and Piezo1 channels on shear- induced ATP release. Carbenoxolone (Carben) and glibenclamide (Gliben) are used to inhibit pannexin-1 and CFTR, respectively. GsMTx4 is used to inhibit Piezo1 channels. The error bars are reported as the SDs of the mean (n = 4 for Carben and Carben/Glibentreated RBCs; n = 3 for Gliben-treated RBCs; and n = 4 for Carben/GsMTx4- treated RBCs). *: $P < 0.05$; **: $P < 0.01$; ***: $P < 0.001$.

4.3.3 Discussion

The main finding presented here is that the mechanosensing cation channel Piezo1 on RBCs regulates Ca^{2+} influx and participates in shear-induced ATP release. This finding is shown by measuring reduced ATP release and Ca^{2+} influx in RBCs that are treated with Piezo1 inhibitors. In addition, our data show that significant ATP release can be activated only when the extracellular Ca^{2+} concentration is above a threshold, suggesting a regulatory role of Ca^{2+} influx in ATP release. Thus, it is likely that shear-induced stretch of RBCs activates the mechanosensing cation channel Piezo1, which allows Ca^{2+} influx and consequently, induces ATP release from RBCs. A paper published after the initial submission of this report shows a role for Piezo1 in red cell volume regulation [95], but to the best of our knowledge, our study is the first to show a role of Piezo1 in the response of normal human RBCs to physiologically relevant fluid forces that could have relevance to the regulation of vascular tone.

We previously identified two distinct timescales associated with the mechano-transductive release of ATP from normal human RBCs [17] and showed that these were consistent with the physical processes described in a model of the process involving CFTR and actin [79]. In addition, we investigated the links between single-RBC dynamics and ATP release and concluded, based on the effects of different inhibitors that CFTR and pannexin-1 respond differently to shear [16]. Carbenoxolone is a pannexin-specific blocker and has been used to block specifically pannexin activity in a wide range of cell lines, including RBCs [80, 96-99]. In studies that appeared subsequent to our prior report, however, it was shown that glibenclamide can attenuate pannexin-1 channel currents [100, 101] and thus, is not specific to CFTR [102]. As a result, the decreased ATP release from

RBCs treated with both glibenclamide and carbenoxolone may reflect the reduced activity of pannexin-1 only. The role of CFTR in the process of ATP release is unclear [37, 103]. Early reports [76] implicated CFTR as a contributor to ATP release from RBCs based on inhibitor activity and different behaviors of red cells from cystic fibrosis patients. Subsequently, a direct role for CFTR in the release of ATP from RBCs was called into question for several reasons: first, the inability to detect CFTR in RBC membranes [104]; second, whether CFTR itself transports ATP remains controversial [105]; and third, the fact that inhibitors originally thought to act on CFTR preferentially also block ATP transport through pannexin-1 [100]. The most direct explanation for our results using carbenoxolone and glibenclamide is that ATP transport occurs primarily through pannexin-1. The different ATP transport behavior in cystic fibrosis patients could be explained by a modulatory effect of CFTR on transport through pannexin-1.

Our results here also show that ATP release correlates with Ca^{2+} influx and that the amount of released ATP and Ca^{2+} influx in HX RBCs is significantly lower than that in healthy control RBCs (Figure 4-6). HX is linked to mutations of Piezo1 channels on RBCs, and such mutations alter the kinetics of Piezo1 and lead to RBC dehydration and hemolytic anemia [87, 88]. The mutations result in two important differences in the kinetic behavior of the Piezo1 channels in HX cells: the rate of inactivation is slower (~200 ms), and the latency to activation is longer [87, 88]. The slower rate of inactivation would be expected to extend the open time of the channels and lead to larger Ca^{2+} influx, contrary to experimental findings. Thus, the more important effect is most likely the longer latency period before activation, because this latency should lead to lower Ca^{2+} influx, consistent with experimental findings. In healthy RBCs, activation of Piezo1 is fast (i.e., within a few milliseconds) [87]. In our experiment, the duration of increased shear (t_c) is ~9.6 ms, which is long enough to activate Piezo1 in healthy RBCs but much shorter than the latency for activation of mutant Piezo1 channels in HX RBCs. As a result, shear-induced Ca^{2+} influx in HX RBCs is significantly lower than that in healthy control RBCs in our experimental setup.

We also consider the possible contributions of membraneassociated ATP pools in RBCs to the shear-induced ATP release. An estimate of the number of ATP molecules released per cell in our experiments indicates that the membrane pool of ATP is not large enough to account for all of the ATP released. The approximate number of ATP molecules released from single RBCs calculated from our data is ~466,000 (Table 4-2).

Table 4-2. Calculation of ATP release from single RBCs.

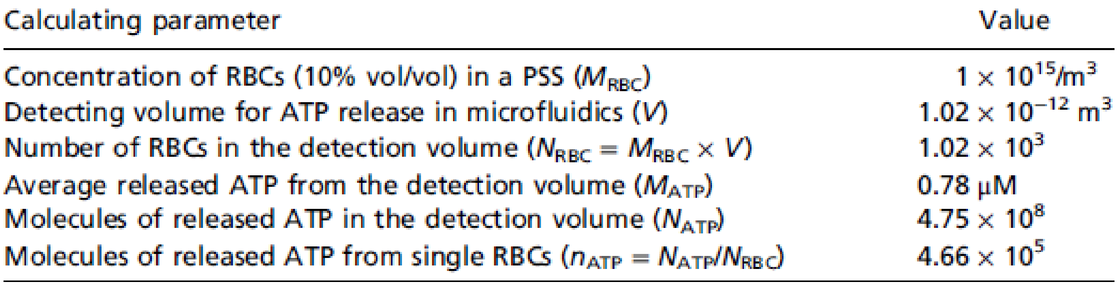

Calculating parameter	Value
Concentration of RBCs (10% vol/vol) in a PSS (M_{RBC})	$1 \times 10^{15}/m^3$
Detecting volume for ATP release in microfluidics (V)	1.02×10^{-12} m^3
Number of RBCs in the detection volume ($N_{RBC} = M_{RBC} \times V$)	1.02×10^3
Average released ATP from the detection volume (M_{ATP})	0.78 μM
Molecules of released ATP in the detection volume (N_{ATP})	4.75×10^8
Molecules of released ATP from single RBCs ($n_{ATP} = N_{ATP}/N_{RBC}$)	4.66×10^5

This value is about 20 times more than the pool ATP (e.g., ~27,000 molecules of ATP for a typical RBC) [94]. Thus, it is unlikely that all of the released ATP comes from the ATP pools, unless there is a much more rapid refilling of the pool from bulk ATP than has been previously established. If it is true, as Chu et al. [92] suggest, that the released ATP comes from the membrane pool, then constant, facile access to bulk ATP (possibly because of membrane deformation) is presumably required to maintain the pool ATP for release. This scenario is consistent with our observations of the inhibitory effects of ouabain that we have observed. Experiments on RBC ghosts have led to the conclusion that ouabain acts to prevent replenishment of the membrane pools from bulk ATP. This limited access of membrane-associated ATP pools to the bulk ATP because of ouabain treatment would result in a reduced amount of releasable ATP in the pools and consequently, a decreased ATP release, which we have observed. It should be noted, however, that ATP compartmentation in human RBCs was discovered in RBC ghosts, and direct evidence of the presence of ATP pools in intact RBCs remains elusive, although indirect arguments in favor of the presence of pools in intact cells have been made [93, 106].

Our results, however, raise the question of how Ca^{2+} influx in RBCs relates to ATP release. The dependence of ATP release on intracellular Ca^{2+} has been shown in various cell lines, including urothelial and endothelial cells [107, 108]. Indeed, functional roles of Piezo1 in stretch-evoked Ca^{2+} influx and ATP release in urothelial cell cultures have been shown recently [107]. In these cell types, however, a Ca^{2+}-regulated vesicular exocytosis is commonly involved in the process of ATP release. RBCs are lacking organelles, such as the Golgi complex, to form vesicles, and consequently, the Ca^{2+}-regulated vesicular exocytosis is not applicable to the observed relation between Ca^{2+} flux and ATP release from RBCs. However, it has been shown that locally increased Ca^{2+} levels near the RBC plasma membrane reduce the interactions between 4.1R and the spectrin-actin network [109] and increase the depolymerization of actin filaments [110]. Given that CFTR can be activated by membrane-associated actin molecules and induces ATP release [76, 79], it is possible that Ca^{2+} participates in the process of ATP release by modulating the interactions between actin and CFTR. Furthermore, because pannexin-1 channels can be activated by cytoplasmic Ca^{2+} [111], it is also possible that shear-induced Ca^{2+} influx activates pannexin-1 directly and triggers ATP release.

However, Piezo1 inhibitors do not block completely Ca^{2+} influx (Figure 4-4B), and thus, a basal ATP release is still observed (Figure 4-3C). This basal ATP release can be further reduced when both Piezo1 and ATP-releasing channel pannexin-1 are inhibited (Figure 4-7B, carbenoxolone and GsMTx4 treatment). In this case, the amount of released ATP (0.29 ± 0.07 μM) (Figure 4-5B) is comparable with that of ATP released in 0 mM extracellular Ca^{2+} solution (0.34 ± 0.02 μM) (Figure 5-6B), emphasizing the regulatory role of Ca^{2+} influx in ATP release. The fraction of released ATP inhibited by carbenoxolone (0.49 ± 0.14 μM) (Figure 5-7B), however, is approximately the same as that inhibited by Piezo1 inhibitor GsMTx4 (0.45 ± 0.05 μM) (Figure 4-3C).

Shear-induced Ca^{2+} influx can activate plasma membrane Ca^{2+} ATPase (PMCA) [112-114] that pumps extra Ca^{2+} out of the cell rapidly. As a result, intracellular Ca^{2+} decreases quickly, which may down-regulate the ATP release. Indeed, considering the kinetics of PMCA activity and the timeframe of ATP release, this mechanism seems feasible. The turnover rate of PMCA is 50–300 per second [115, 116], the number of pump units per cell is 400–700 [116], and the increased intracellular Ca^{2+} levels in RBCs caused by the mechanical deformation are 12–24 nM [114]. Combining these numbers, we estimate a timescale for PMCA to remove the extra Ca^{2+} of 30–100 ms, which is comparable with the duration of ATP release (∼100 ms).

Therefore, it seems likely that the parallel activities of PMCA and ATP release compete in Ca^{2+} use inside the cell and that the dynamic concentration of intracellular Ca^{2+}

determines the patterns of ATP release. When a slight increase of intracellular Ca^{2+} occurs because of shear-induced Ca^{2+} influx, for example, PMCA pumps the extra Ca^{2+} out of the cell, rapidly leaving a negligible amount of Ca^{2+} to trigger ATP release. When intracellular Ca^{2+} increases significantly, however, it will take a period for the PMCA to pump the extra Ca^{2+} out of the cell, and consequently, there will be a sufficient amount of intracellular Ca^{2+} to trigger ATP release. After extra intracellular Ca^{2+} ions are pumped out completely, ATP release stops. This process explains the existence of a threshold of extracellular Ca^{2+} concentration that triggers ATP release and the transient ATP release patterns that we observed in this study and previous studies. Collectively, we propose a model to account for the observed mechanotransductive release of ATP from RBCs (Figure 4-8).

It is important to note that our data indicate that Ca^{2+} influx is important for mechanically induced ATP release, but whether this observation results from modification of cytoskeletal stability or whether the release might be modulated by either PMCA activity or Ca^{2+} acting directly on ATP release channels remains to be determined. In addition, our data show that neither inhibitors nor mutation can block ATP release or Ca^{2+} entry completely. Instead, the decrease in ATP release and Ca^{2+} entry brought about by inhibitors or mutation is about one-half of the normal amount. Furthermore, basal ATP release can still occur when extracellular Ca^{2+} is 0 mM (Figure 4-6B) or both Piezo1 and pannexin-1 channels are inhibited (Figure 4-7B).

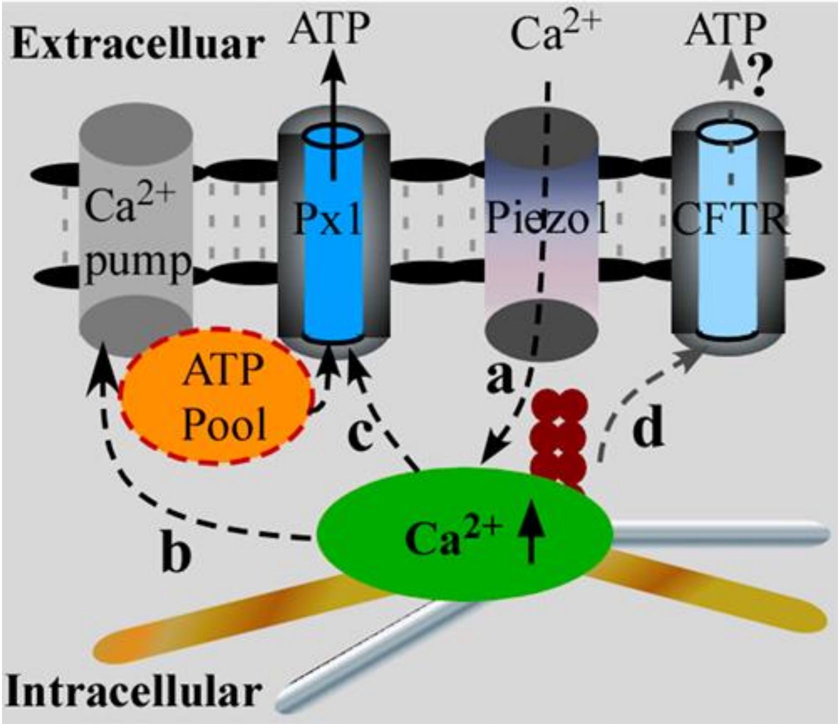

Figure 4-8. Schematic of the proposed mechanotransductive release of ATP from RBCs. (A) Shear-induced stretch of RBCs activates Piezo1 channels and induces an increased Ca^{2+} influx, which (B) activates Ca^{2+} pumps to remove extra Ca^{2+} rapidly. (C) Meanwhile, increased Ca^{2+} influx activates pannexin-1 channels (Px1) directly and triggers ATP release from the membrane-associated ATP pools. (D) It is also possible, although controversial, that increased Ca^{2+} influx depolymerizes actin filaments (brown spheres), which activates CFTR and induces the release of ATP. Regardless of the precise mechanism, our results show clearly that a critical concentration of intracellular Ca^{2+} caused by shear-induced Ca^{2+} influx is required for the mechanotransductive release of ATP

These results, thus, suggest that (i) Ca^{2+} influx is necessary only when a significant amount of ATP release is required and (ii) pathways other than Piezo1-regulated Ca^{2+} influx also participate in shear-induced Ca^{2+} entry and ATP release.

4.4 Conclusion

In summary, we illustrate for the first time, regulatory role of Piezo1 in shear-induced ATP release from human RBCs and provide evidence for a Ca^{2+}-triggered ATP release model. These results represent a substantial step forward in understanding the mechanotransductive release of ATP from RBCs, which will be critical to the development of improved therapeutic strategies for red cell dysfunction and vascular disease. After such strategies become available, for example, in diseases that are associated with impaired ATP release from RBCs, pharmacologic regulation of the calcium influx in RBCs could be used to achieve enhanced ATP release. Conversely, when less ATP release is needed (for example, to store RBCs or in the case of handling blood using mechanical devices), the calcium influx could be decreased. Decreasing activity of Piezo1 is likely to be sufficient for this purpose. Thus, important advances in the therapy of diseases and complications that are associated with the release of ATP from RBCs are expected. In addition, because of the high spatiotemporal resolution of the developed microfluidic approach, we anticipate that the experimental procedure developed here will be useful for elucidating the dynamics of Piezo1 channels at the whole-cell level, which has been known to be critical and much needed for extrapolation of patch recordings results to functionality [117].

5. CONCLUSION

RBC is the major cell type in the body, and they are responsible for oxygen exchange in the body. There is no nucleus in RBCs and due to the structure and its surface-to-volume ratio, they are deformable and play an important role in microcirculation. In our work, we illustrated that RBCs can sense oxygen level and modify their membrane in blood flow. It was found that RBC membrane became more stretchable under hypoxia, which made it smoother for them to pass through the capillaries. To better understand the mechanism of RBC membrane modification under hypoxia, we studied the interactions between protein membrane, band 3, ankyrin, and deoxyHb. It was shown in both *ex vivo* and *in vivo* experiments that during deoxygenation, deoxyHb-band 3 interaction increased while band 3-ankyrin interaction decreases. As a result, the association between cell membrane and cytoskeleton was compromised, which lead to a more deformable membrane and eventually facilitated the blood flow in capillaries. Additionally, we studied the RBC function in flow condition where they experienced shear stress. It was known that the mechanosensitive channel, Piezo1, on cell membrane was activated which triggered shear-induced Ca^{2+} influx. From our work, we concluded that shear-induced Ca^{2+} influx through Piezo1 channel was critical to RBC ATP release. Summarily, our work built the connection of the dynamic roles of RBCs in different conditions. With the more in depth understanding, we could have more knowledge about different disease models that are linked with blood flow dysfunction, such as Alzheimer's disease, sepsis, sick cell disease and so on. Through our work, we may have potential development of therapeutic strategies for the diseases.

6. APPENDIX

❖ MICROFLUIDIC ASSAY OF THE DEFORMABILITY OF PRIMITIVE ERYTHROBLASTS

Primitive erythroblasts (precursors of RBCs) enter vascular circulation during the embryonic period and mature while circulating, hereby experiencing significant hemodynamic shear stress. Shear-induced deformation of primitive erythroblasts, however, is poorly studied. In this work, we examined the deformability of primitive erythroblasts at physiologically relevant flow conditions in microfluidic channels and identified the regulatory roles of the maturation stage of these erythroblasts and cytoskeletal protein 4.1 R on shear-induced cell deformation. The results showed that the maturation stage affected the deformability of primitive erythroblasts significantly, that at later maturational stages exhibit an improved deformability due to the matured cytoskeletal structure in the cell membrane.

Reproduced from [118], with the permission of AIP Publishing

6.1 Introduction

Primitive erythroblasts are precursors of erythrocytes and essential to the regeneration of erythrocytes and fetal development. They carry both embryonic and adult hemoglobin while “definitive” cells only accumulate adult hemoglobin [3, 5, 6, 10]. Similar to the process in mouse, nucleated primitive erythroblasts join the yolk-sac circulation from the fourth to fifth week of gestation [5] in humans. As shown in Figure 6-1, definitive cells rapidly dominate the cell population at around E14.5 and E15.5. Also, it is confirmed that primitive red cells have significant bigger size than definitive cells. Primitive erythroblasts can be further identified in the embryo after 6 weeks [3]. Starting from the eighth week, definitive cells from the liver are observed while primitive erythroblasts are still the majority [3]. Due to the similar maturation process of primitive erythroblasts in humans and mouse, many studies of primitive erythroblasts are conducted in mouse embryos.

In mouse embryo, primitive erythroblasts mature as a semi-synchronous cohort over the next several days as they circulate in the bloodstream. Primitive erythroblasts transit from pro-erythroblasts at E9.5 to orthochromatic erythroblasts at E12.5 and then enucleate over the subsequent 4 days of gestation [5, 7] to produce mature erythrocytes. The circulation of primitive erythroblasts also contributes to the formation and remodeling of blood vessels in the yolk sac. Without the presence of such circulation, for example, regular development of the embryo such as vessel remodeling and maturation is impaired [119-121].

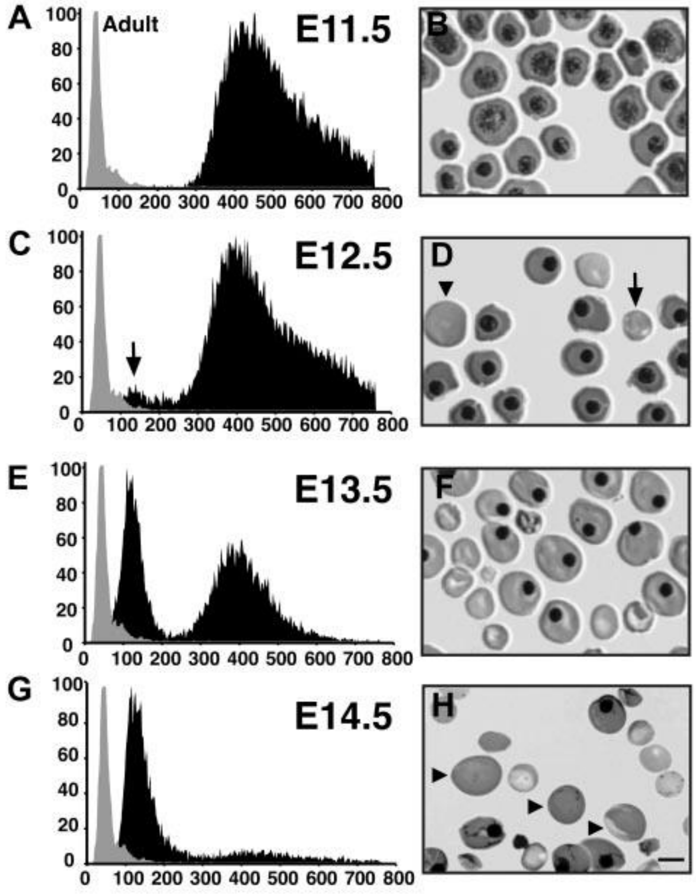

Figure 6-1. Changes in cellular composition of blood from E11.5 to E14.5 of mouse gestation. In A, C, E and G, gray area shows the cell size distribution of circulating blood cells, while black area indicates a sample of adult murine red cells. The y-axis indicates the relative cell number and x-axis represents cell volume. B, D, F and H represent the pictures of cells with nuclei and after enucleation.

Primitive erythroblasts experience shear stresses in the fetal bloodstream and have to move throughout the embryonic microvasculature that has a diameter from 4 µm to 60 µm [11]. Because the size of primitive erythroblasts with maturation stages from E8.5 to E12.5 varies from 17 µm to 13 µm [122], flexibility and elasticity that allow the primitive erythroid cells to move through the embryonic microvasculature are crucially important. Although the structure and composition of the cytoskeletal network in adult erythrocytes, as well as their deformability, are well established, the deformability of maturing erythroblast precursors is less understood. One of the possible reasons is that protein composition in the cytoskeleton of primitive erythroblasts changes with the maturation stage. Decreases in surface area (about a 35% loss), volume (50% loss), and sphericity (6% loss) along maturation have been observed and can be attributed to the membrane and cytoskeleton protein remodeling (Figure 6-2) [123]. Remodeling also leads to a reduced stiffness of the cell membrane [123]. In addition, as primitive erythroblasts mature, shear stress activates intracellular kinases to remodel the membrane and cytoskeletal compositions [120]. Without the correct protein components that make up the cytoskeleton network such as actin, spectrin, and protein 4.1R [124], erythroid cells will have a less deformable cytoskeleton network that could potentially lead to hemolytic anemia [125].

While the structural remodeling of the membrane and cytoskeleton of primitive erythroblasts has been investigated, flow-induced deformation of primitive erythroblasts at different maturation stages is less studied. In addition, although defects of protein 4.1 R are tightly linked to hereditary elliptocytosis [126], characterized by morphologically abnormal and mechanically unstable erythrocytes [127-133], the regulatory role of protein 4.1 R in erythroblast deformation remains unknown.

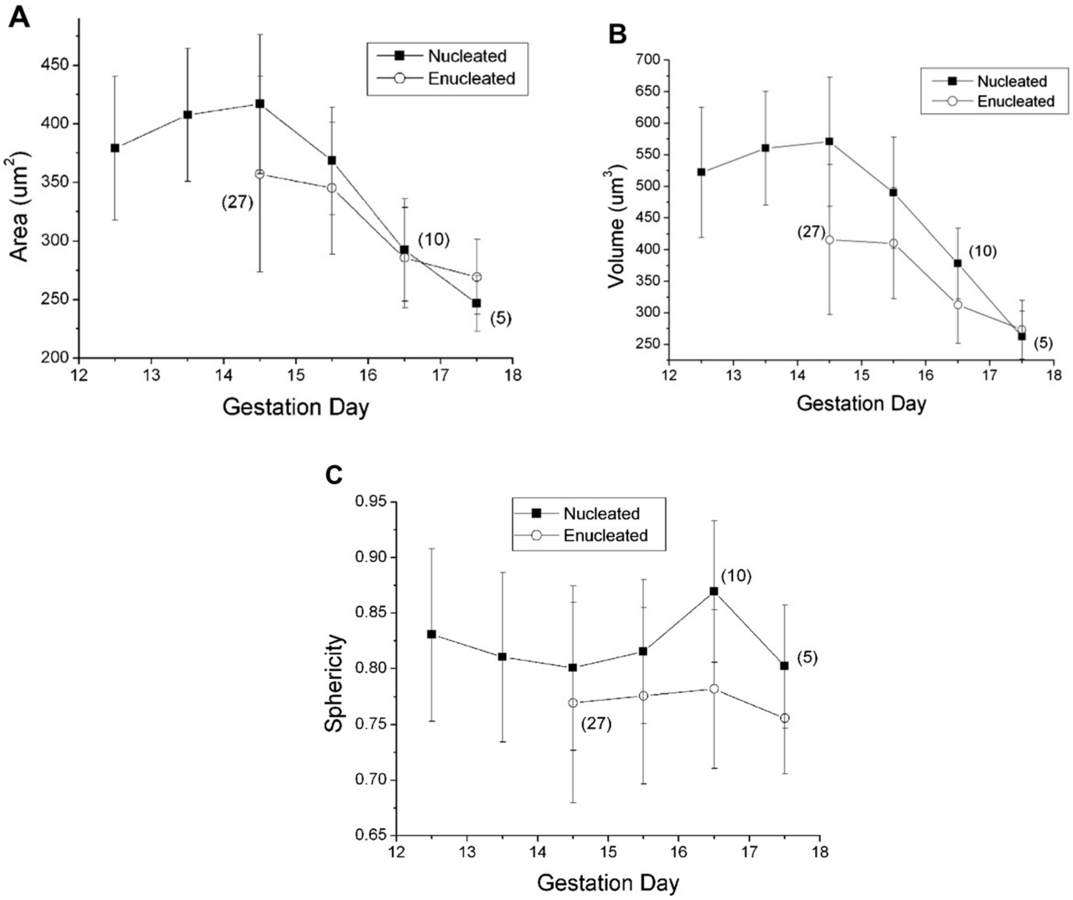

Figure 6-2. Changes in cell dimensions within gestational age. Between E12.5 and E14.5, the change in cell surface and volume is not noticeable. Decreases in surface area, volume, and sphericity can be observed after E14.5.

Although studies of deformability-induced red cell migration have been conducted in small capillaries under a bulk suspension [134, 135], we here developed microfluidic approaches to study the deformability of single primitive erythroblasts under physiologically relevant flow conditions. We determined the effect of maturation stage on the deformability of primitive erythroblasts and unveiled the regulatory roles of protein 4.1 R in cell deformation. Lastly, we investigated the deformability of primitive erythroblasts when squeezing through a narrow constriction channel mimicking the size of the capillary.

6.2 Experimental methods

6.2.1 Mice and collection of embryonic peripheral blood

All animal experiments were approved by the University of Rochester Committee on Animal Resources (UCAR). *Epb4.1*$^{+/+}$ and *Epb4.1*$^{-/-}$ mice [126] were provided by Dr. John Conboy (Life Sciences Division, Lawrence Berkeley National Laboratory, Berkeley, CA).

Outbred ICR (Taconic Biosciences, Germantown, NY) and *Epb4.1*$^{+/-}$ mice were mated overnight, and vaginal plugs were checked the following morning (embryonic day 0.3; E0.3). At defined gestational ages, mice were sacrificed by CO_2 narcosis and the embryos were dissected in PB2 [136, 137] containing 12.5 μg/ml of heparin. E10.5 and E12.5 embryos were bled in PB2 and the embryonic peripheral blood was collected from the bottom of the dishes. Total cell numbers and viability were determined by trypan blue staining (Sigma-Aldrich). Embryos from *Epb4.1*$^{+/-}$ mouse mating were genotyped using the AccuStart^{TM} II Mouse Genotyping Kit (Quanta Biosciences) with primer pairs as follows: neo (neo-f, 5’-GATGGATTGCACGCAGGT-3’; neo-r, 5’-GGCAGGAGCAAGGTGAGA-3’; 318 bp) [138]; *Epb 4.1* exon 4 (Epb4.1E4-f, 5’-GCTCAGGAAGAACACAGAGAGG-3’; Epb4.1E4-r, 5’-CATTCGTAGACCGTGTCATCC-3’; 197 bp) [138].

6.2.2 Microfluidic fabrication and experimental setup

PDMS chips were fabricated using standard soft photolithography techniques. The channel inside of the PDMS chip has a uniform length of 100 μm (l_c = 100 μm) and a width of 20 µm (w_c = 20 µm) at a constriction section, and a width of 100 µm for the rest of the channel. The height of the channel is 30 µm (h = 30 µm) everywhere. To test the deformability in a narrow microfluidic channel, we fabricated a microfluidic channel with l_c = 170 µm, w_c = 5 µm, and h = 7 µm, which mimics the size of capillaries [11]. Using a 1mL syringe and needle (Med Lab Supply), the suspension of primitive erythroblasts collected from mouse embryos (2 v/v % in PBS) was transferred to polyethylene tubing [Scientific Commodities Inc, 0.015” (0.38 mm) I.D.× 0.043” (1.09 mm) O.D.], which was then inserted into the microchannel after removing air bubbles. The primitive cells in the microfluidic channel were visualized using a Leica microscope (Leica Microsystems, DMI 6000) with a 63× oil-immersion objective. A syringe pump (KD Scientific) was introduced to maintain the flow rate of 0.75 µl/min, 1.5 µl/min, or 3 µl/min.

Videos of the primitive cells flowing through the microchannel were recorded using a high-speed camera (Sample rate: 1900 pps, Phantom) coupled to the Leica microscope. Phantom Camera Control software (PCC) from Vision Research Inc. was used to analyze the elongation of the cell D_l/D_w, where D_l and D_w are the length and width of the cell, respectively. The position of the entrance of the constriction channel is defined as t = 0 ms. The time frame of cells on corresponding positions was calculated based on the time interval between each frame (526 µs).

6.2.3 Preparation of primitive erythroid cell lysates

E12.5 primitive erythroblasts were washed 3 times with phosphate-buffered saline (PBS, 300 mOsm/kg), and then resuspended in RIPA buffer [139, 140] (50mM Tris [tris(hydroxymethyl)aminomethane], 150mM NaCl, 1% Nonidet P-40 or 1% Igepal CA-

630, Sigma-Aldrich; 0.1% SDS, 0.5% sodium deoxycholate, 1mM EDTA [ethylenediaminetetraacetic acid], 1mM DTT [Dithiothreitol], pH 8.0) in the presence of complete protease inhibitor cocktails (Roche), 25 µg/ml PMSF, and 1mM Na_3VO_4, and incubated on ice for 30 min. Nuclei and debris were separated by centrifugation at 500 g for 10 min at 4 ˚C. Samples were stored at -80 ˚C until analysis.

6.2.4 Immunoblotting analysis

Erythroid cell lysates from 5×10^{31} cells were separated by 4%–20% SDS-PAGE (Bio-Rad) and transferred to PVDF membranes (EMD Millipore). The membranes were blotted with antibody in 5% (w/v) nonfat dry milk (Bio-Rad) in TBST (50mM Tris, 150mM NaCl; 0.1% [v/v] Tween-20) and washed in TBST. The signal was detected using the Pierce ECL Plus Western Blotting Substrate (Thermo Scientific) and developed on a BioMax XAR film (Carestream). Anti-protein 4.1 R antibody (NY Blood Center, NY) [123], anti-*β*-actin antibody (Sigma-Aldrich), and HRP-conjugated secondary antibodies (Bio-Rad) were used in immunoblotting analysis.

6.2.5 Cell Stain

E10.5 erythroblasts were suspended in 10% Normal Rat Serum (NRS; Invitrogen) and block on ice for 15 min. To stain the cell membrane, 1:100 Alexa Fluor 488-Ter119

(BioLegend) was added on ice for 20 min, followed by one-time wash using PB2. Cells were then resuspended in PB2 and stained on ice using DRAQ5 (eBioscience) for another 5 minutes, after which the cells were ready for imaging [141].

6.3 Results and discussion

We investigated the deformability of primitive erythroblasts by flowing them through a constriction channel (w_c = 20 µm, h = 30 µm, and l_c = 100 µm) embedded in a microfluidic device (Figure 6-3A). Because the estimated thoracic aortic shear stress in the embryonic circulation of mouse embryo is about 3.8 Pa [142], the volumetric flow rates used in the current study were 0.75 µl/min, 1.5 µl/min, and 3 µl/min, which provided approximately shear stresses of 1.05 Pa, 2.1 Pa, and 4.2 Pa, respectively. In Figure 6-3B, t = 0 ms was assigned to the time at which the primitive erythroblast entered the constriction channel. An increase of D_l/D_w was observed before t = 526 µs, and then D_l/D_w decreased, indicating that the cell elongated upon entering the channel and recovered while exiting the constriction channel (Figure 6-3B). The results were consistent with the deformation of mature red blood cells flowing through constriction channels [43] and suggested that primitive erythroblasts were deformable at E12.5.

We then studied the effect of flow rate (or shear stress) on the deformation of primitive erythroblasts at two different maturation stages, i.e., E10.5 and E12.5. The results showed that E12.5 cells did not deform significantly when the flow rate was increased from 0.75 µl/min to 1.5 µl/min. The maximum elongation index, however, increased significantly ($p < 0.0001$) when the flow rate was increased to 3 µl/min.

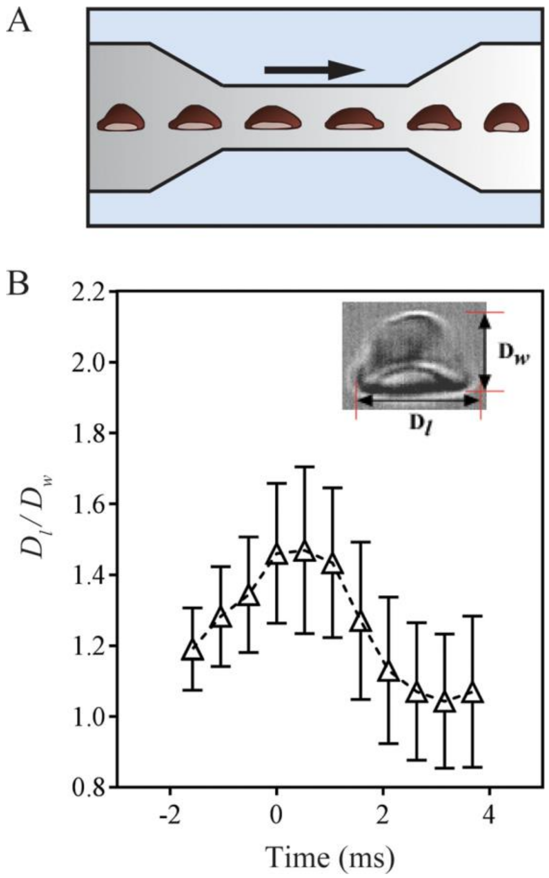

Figure 6-3. Experimental setup of the microfluidic assay of the deformability of primitive erythroblasts. (A) Schematic of the microfluidic approach to examine the deformation of primitive erythroblasts. The length (l_c) and width (w_c) of the constriction channel are 100 µm and 20 µm, respectively. The height of the channel is 30 µm. The arrow indicates the direction of flow. (B) Change of the elongation index (D_l/D_w) of primitive erythroblasts at E12.5 passing through the constriction channel. Flow rate = 1.5 µl/min. Time = 0 ms corresponds to the position of the entrance of the constriction channel. The inset is an image of a primitive erythroblast at E12.5 and the definition of D_l and D_w (n = 39).

Because shear stress at the flow rate of 3 µl/min is approximately 4.2 Pa, close to the estimated shear stress in the embryonic circulation of mouse embryo, the increased elongation index at the flow rate of 3 µl/min demonstrates that E12.5 cells will deform significantly in physiologically relevant flow conditions. As to E10.5 cells (Figure 6-4B), the elongation index did not show a significant difference when the flow rate increased from 0.75 µl/min to 1.5 µl/min. The elongation index started to increase when the flow rate was 3 µl/min. To compare the deformability of E12.5 and E10.5 under the same flow rate, we examined the change of the maximum elongation index of both cells. The results showed that E12.5 cells always had a significantly higher elongation index than that of E10.5 cells ($p < 0.0001$) (Figure 6-4C), indicating that cells at E12.5 were more stretchable than the ones at E10.5. The lack of significant increase of the elongation index with increased shear stress indicated the finite stretchability of E10.5 cells, which might arise from the immature cytoskeletal network or the lack of excess of membrane materials for the given cytoplasmic volume that consequently constrains the deformability of erythroblast cells.

We have shown recently an increased expression of 4.1 R transcripts as erythroblast cells transit from E10.5 to E12.5 and that an erythroid-specific isoform switch occurs between E10.5 and E11.5 [141]. Because 4.1 R can form a ternary complex with actin and spectrin and plays important roles in maintaining the integration of the cytoskeletal network of mature erythrocytes [143], it is likely that protein 4.1R in the cytoskeletal composition between E10.5 and E12.5 is, in part, responsible for the observed phenomena in erythroblast cells.

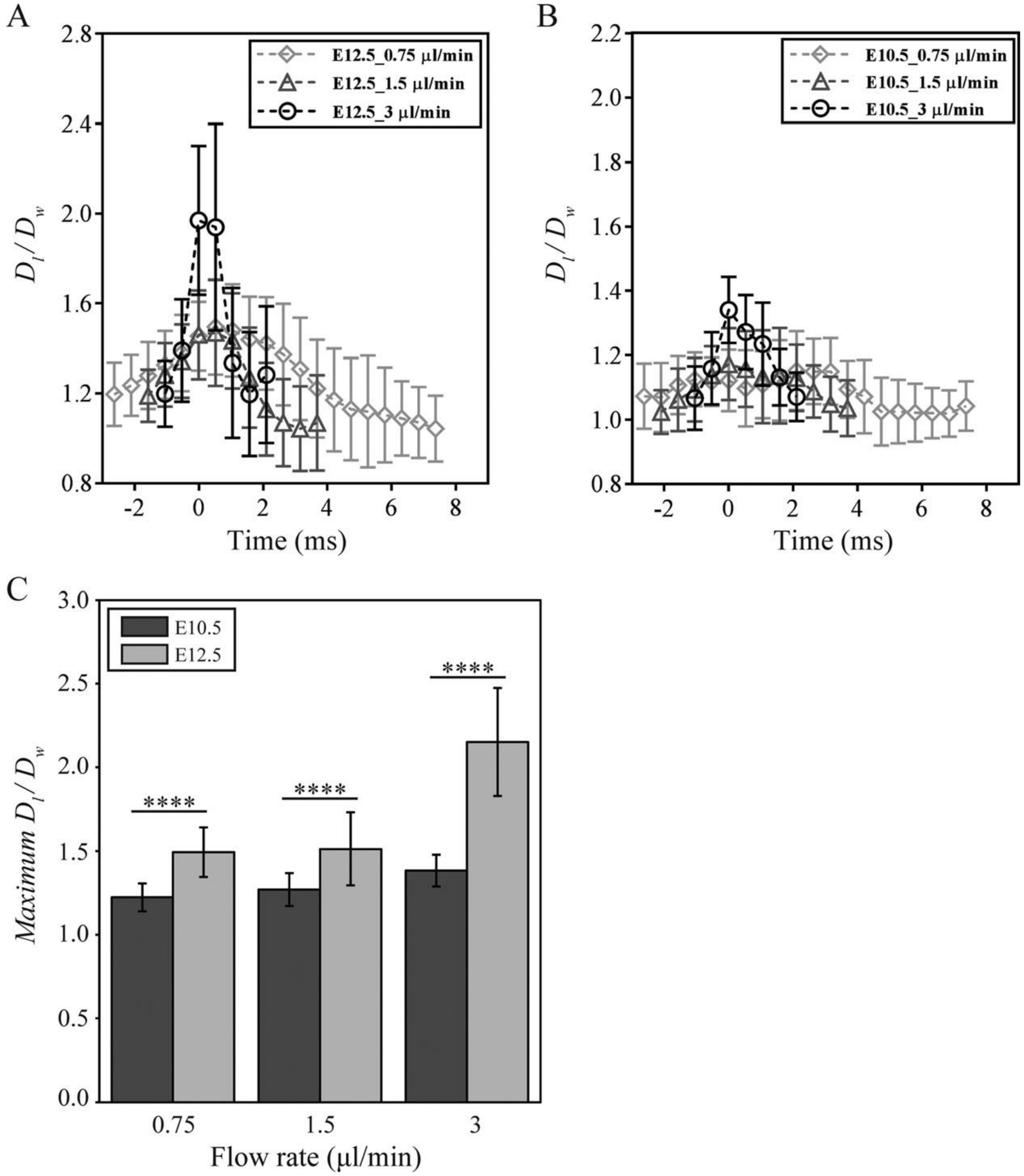

Figure 6-4. Effect of flow rates on the change of elongation index of primitive erythroblasts at (A) E12.5 (n = 173) and (B) E10.5 (n = 68). (C) Effect of flow rates on the change of maximum elongation index (D_l/D_w) of primitive erythroblasts when passing through the constriction channel. The Student's t-test showed significant difference between E10.5 and E12.5 cells when applying the same flow rate (****: $p < 0.0001$).

To confirm the role of 4.1R in erythroblast deformability, we tested the shear-induced deformation of primitive erythroblasts from *Epb4.1* knockout (KO) mice. As shown in the Western Blot analysis depicted in Figure 6-5A, control samples with *Epb4.1*$^{+/+}$ showed the presence of protein 4.1 R, wherease primitive erythroblasts from *Epb4.1* KO mice lacked the protein 4.1R. Actin was used as the control to demonstrate that actin was well expressed for both non-KO and KO cells and was detectable. When the deformatibilty of primitive erythroblasts at E12.5 from Epb4.1 KO mice was studied in the same flow conditions as described above, the elongation index decreased compared to the wild type (Figures 6-3B and 6-4A). With the increase of flow rates, the deformation of protein 4.1 KO cells did not change significantly. The E12.5 protein 4.1 KO primitive erythroblasts, in fact, showed similar patterns with E10.5 primitive erythroblasts under the same flow rates (Figure 6-4B), suggesting that protein 4.1 KO E12.5 cells have the similar deformability as wild type E10.5 primitive erythroblasts. However, when the flow rate increased to 3 µl/min, there was no obvious change in protein 4.1 KO E12.5 cells, while the E10.5 cells can be stretched more under higher shear stress. Because protein 4.1R is critical to the formation of nodal junctions (with actin and spectrin) of the membrane-skeletal network [143] and the maximum local extension of the cell membrane depends on the difference between the average separation of the junctions and the contour length of the spectrin tetramers [144], the lack of 4.1R in the membrane of erythroblasts likely impairs the connections between spectrin and/or the spectrin dimer-tetramer equilibrium. It attributes to the failure of forming the functional membrane skeleton network [141]. A recent study shows that due to the absence of 4.1 R, E12.5 primitive cells cannot transform from spherical to partially concave in shape, leading to a relatively small surface-to-volume ratio [141], which consequently results in decreased cell deformability [145, 146].

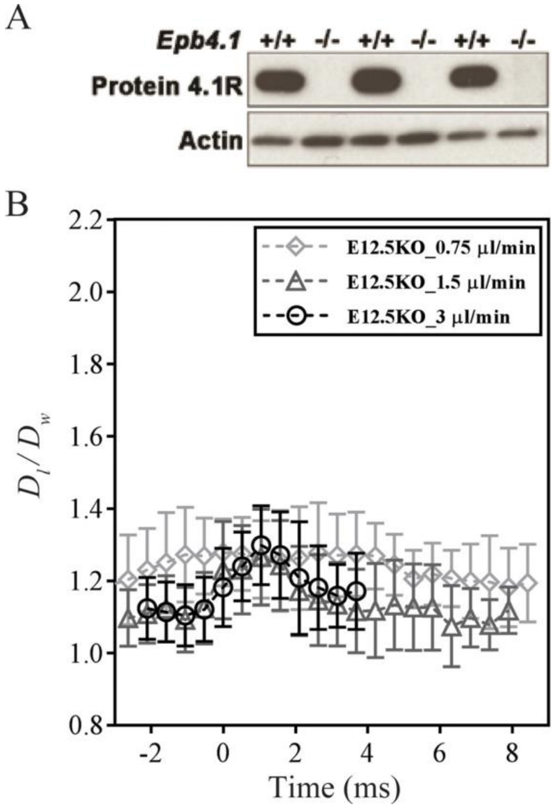

Figure 6-5. Effect of 4.1R on the deformability of primitive erythroblasts. (A) Expressions of cytoskeletal proteins (4.1R and actin) in knockout (KO) and non-KO E12.5 cells. (B) Effect of flow rates on the elongation index of primitive erythroblasts at E12.5 from *Epb4.1* KO mice (n = 135).

Last, to examine the erythroblast deformability in capillaries where cells have to squeeze through the narrow capillary, we flew erythroblasts through a microfluidic device with a much narrower constriction channel that has dimensions of w_c = 5 µm, l_c = 170 µm, and h = 7 µm. In this case, both the membrane and nucleus of the cells are expected to be deformed (Figure 6-6). The results showed that, when individual primitive erythroblasts flew through the constriction channel at a constant flow rate (0.5 µl/min), cells at E12.5 could squeeze through the constriction without compromising the integrity of the cell and elongate to almost twice their original length. After exiting the constriction channel, the E12.5 primitive erythroblasts were able to recover their original morphology with a slightly plastic deformation (Figure 6-6A).

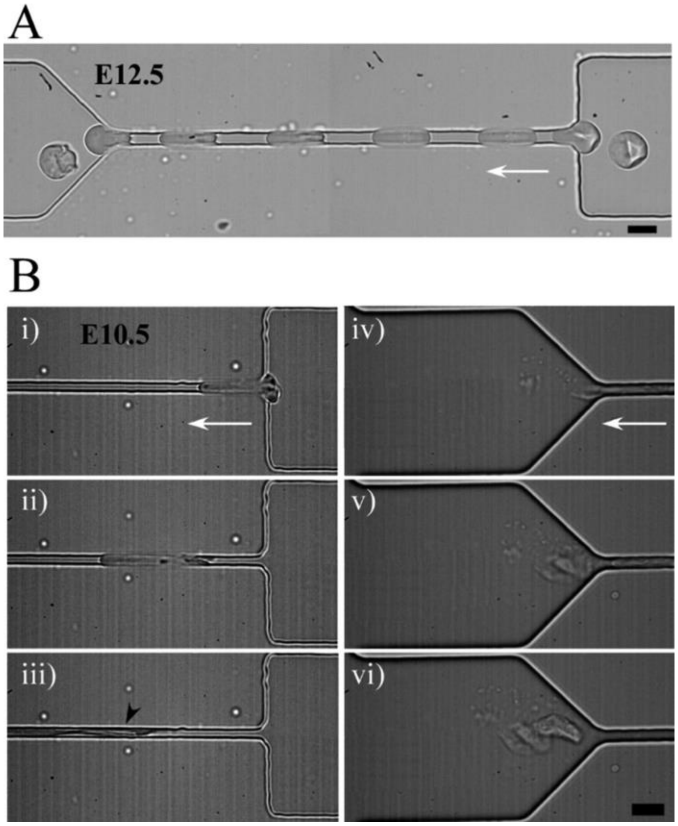

Figure 6-6. Deformation of primitive erythroblasts flowing through a narrow microfluidic channel (l_c = 170 µm, w_c = 5 µm, and h_c = 7 µm). The white arrows indicate the flow direction. (A) Superimposed series of time-lapse images showing the deformation of an individual primitive erythroblast at E12.5 passing through a narrow constriction. (B) A sequence of images of primitive erythroblasts at E10.5 flowing through the narrow constriction. Note that the black arrow (iii) indicates the place where cell starts to lyse, and the white arrow indicates the direction of flow. (Scale bar 10 µm).

In contrast, when primitive erythroblasts at E10.5 were pushed through the constriction channel, the cells lysed before exiting (Figure 6-6B). The results showed that in the conditions of high shear stress and signficant deformation, E12.5 cells were more deformable than those of E10.5. It should be noted, however, that the results did not suggest that the nucleus of E12.5 was more deformable than that of E10.5. Although most of the nuclei of E10.5 primitive erythroblasts are lysed while being squeezed inside the constriction channel, (Figure 6-7A and B), there are still some nuclei that are intact after going through the constriction (Figure 6-7C).

In addition, it was known that at the late stage of maturation (E12.5-E16.5), interactions between cytoplasmic proteins and the nucleus in primitive erythroblasts are attenuated or lost in preparation for enucleation [1, 124, 147, 148]. It is thus possible that the shear force experienced by the membrane of E12.5 cells was not transmitted to the nucleus when passing through the narrow constriction. More importantly, the diameter of primitive erythroblasts decreased from ~15 µm to 13 µm when cells transited from E10.5 to E12.5 during embryonic development [122]. At the same time, the size of nuclei was reduced from ~10 µm for cells at E10.5 to ~5 µm for cells at E12.5 due to nuclear condensation [122]. With the comparable size of the channel with the size of the nucleus and the deformable membrane of E12.5 primitive cells, the shear force experienced by the E12.5 cells may not be transmitted to the nucleus. Thus, the observed lysis of E10.5 primitive erythroblasts may be due to the decreased membrane deformability and the large size and tethering of the nucleus.

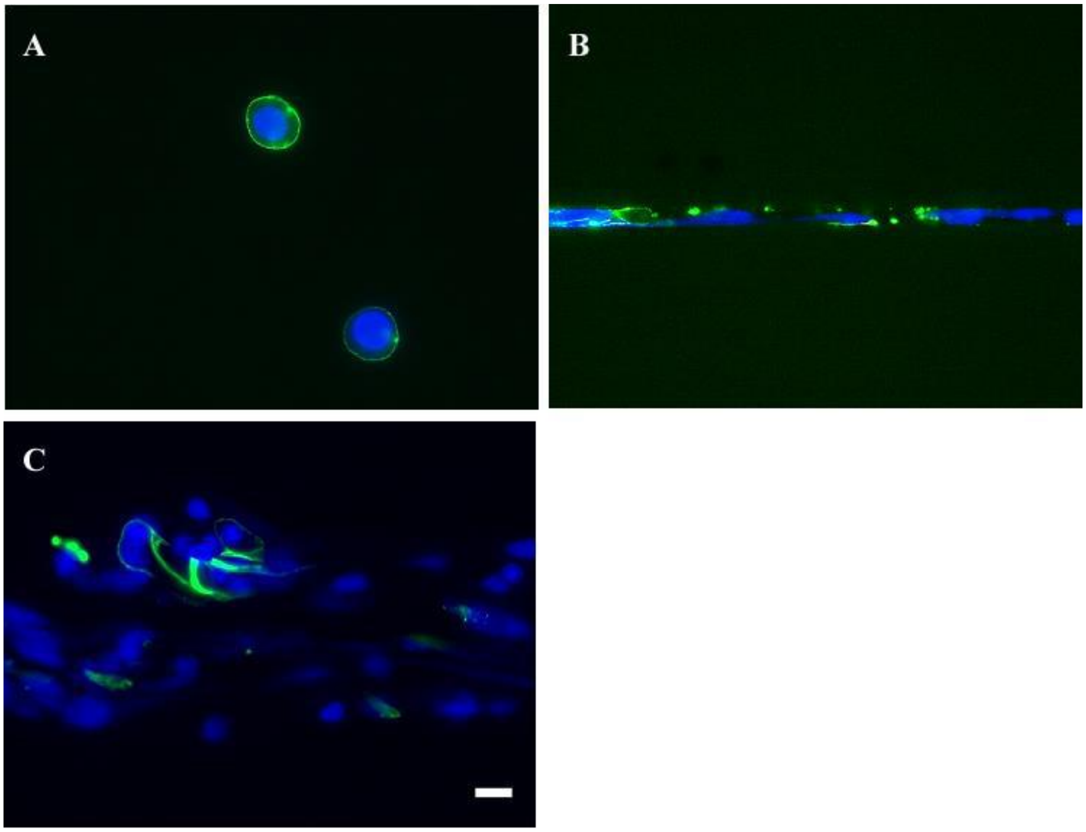

Figure 6-7. Microscopic images showing E10.5 cells before flow (A), inside constriction channel (B) and in the downstream channel after going through the constriction (C). Cell membrane was stained by Ter119 (green) while the nuclei were stained using DRAQ5 (blue). After being squeezed in the constriction channel, cell membrane and a portion of nuclei were lysed. Note that some of the nuclei remained intact after experiencing such shear stress. (Scale bar: 10 μm)

6.4 Conclusion

In summary, by mimicking the physiologically relevant flow conditions using microfluidics, we observed that E12.5 erythroblasts were more deformable than E10.5 erythroblasts under different shear conditions and could recover to their original shape after shear-induced deformation. Thus, the deformability of primitive erythroblasts changes during maturation and primitive erythroblasts at late maturational stages are more deformable. This is likely due to the integration of a critical cytoskeletal protein such as protein 4.1 R in the membrane at the late maturational stage of primitive erythroblasts. In addition, we demonstrated that the deformatibility at E12.5 was higher than that at E10.5 when transpassing narrow constrictions with a similar size of capillaries, further supporting the notion that the maturation of primitive erythroblasts plays a key role in cell deformation. The findings here provide new insights into the deformation of primitive erythroblasts under flow conditions and are important for understanding the evolution of microcirculation in fetus and how it facilitates the oxygen and nutrition transportation providing the necessary physiological environment.

7. REFERENCE

1. Palis, J., *Primitive and definitive erythropoiesis in mammals.* Frontiers in physiology, 2014. **5**: p. 3.
2. Hillman, R.S. and C.A. Finch, *Red cell manual*. 1996: FA Davis Philadelphia.
3. Palis, J. and M.C. Yoder, *Yolk-sac hematopoiesis: the first blood cells of mouse and man.* Experimental hematology, 2001. **29**(8): p. 927-936.
4. McGrath, K.E., et al., *Circulation is established in a stepwise pattern in the mammalian embryo.* Blood, 2003. **101**(5): p. 1669-1675.
5. Kingsley, P.D., et al., *Yolk sac–derived primitive erythroblasts enucleate during mammalian embryogenesis.* Blood, 2004. **104**(1): p. 19-25.
6. McGrath, K.E., et al., *Enucleation of primitive erythroid cells generates a transient population of "pyrenocytes" in the mammalian fetus.* Blood, 2008. **111**(4): p. 2409-2417.
7. Malik, J., et al., *Erythropoietin critically regulates the terminal maturation of murine and human primitive erythroblasts.* Haematologica, 2013: p. haematol. 2013.087361.
8. Tober, J., et al., *The megakaryocyte lineage originates from hemangioblast precursors and is an integral component both of primitive and of definitive hematopoiesis.* Blood, 2007. **109**(4): p. 1433-1441.
9. Zhang, Z.W., et al., *Red blood cell extrudes nucleus and mitochondria against oxidative stress.* IUBMB life, 2011. **63**(7): p. 560-565.
10. Ingram, V.M., *Embryonic red blood cell formation.* Nature, 1972. **235**(5337): p. 338.
11. Lehr, H.-A., et al., *Dorsal skinfold chamber technique for intravital microscopy in nude mice.* The American journal of pathology, 1993. **143**(4): p. 1055.
12. Gallagher, P., *The red blood cell membrane and its disorders: hereditary spherocytosis, elliptocytosis, and related diseases.* William's hematology. 8th ed. New York: McGraw Hill, 2010: p. 617-46.
13. Vertessy, B.G. and T.L. Steck, *Elasticity of the human red cell membrane skeleton. Effects of temperature and denaturants.* Biophysical journal, 1989. **55**(2): p. 255-262.
14. White, F.M., *Fluid mechanics. 5th.* Boston: McGraw-Hill Book Company, 2003.
15. Cho, Y.I. and K.R. Kensey, *Effects of the non-Newtonian viscosity of blood on flows in a diseased arterial vessel. Part 1: Steady flows.* Biorheology, 1991. **28**(3-4): p. 241-262.
16. Forsyth, A.M., et al., *Multiscale approach to link red blood cell dynamics, shear viscosity, and ATP release.* Proceedings of the National Academy of Sciences, 2011. **108**(27): p. 10986-10991.
17. Wan, J., W.D. Ristenpart, and H.A. Stone, *Dynamics of shear-induced ATP release from red blood cells.* Proceedings of the National Academy of Sciences, 2008. **105**(43): p. 16432-16437.
18. Fischer, T.M., M. Stohr-Lissen, and H. Schmid-Schonbein, *The red cell as a fluid droplet: tank tread-like motion of the human erythrocyte membrane in shear flow.* Science, 1978. **202**(4370): p. 894-896.
19. N.N. Barvitenko, N.C. Adragna, and R.E. Weber, *Erythrocyte signal transduction pathways, their oxygenation dependence and functional significance.* Cell. Physiol. Biochem., , 2015. **15**: p. 1-18.
20. G.R. Bergfeld and T. Forrester, *Release of ATP from human erythrocytes in response to a brief period of hypoxia and hypercapnia.* Cardiovasc. Res., , 1992. **26**: p. 40-47.
21. Chu H, et al., *Reversible binding of hemoglobin to band 3 constitutes the molecular switch that mediates O2 regulation of erythrocyte properties.* Blood. , 2016. **128**: p. 2708-2716.

22. Ellsworth, M.L., et al., *The erythrocyte as a regulator of vascular tone.* American Journal of Physiology-Heart and Circulatory Physiology, 1995. **269**(6): p. H2155-H2161.
23. Sprague, R.S., et al., *ATP: the red blood cell link to NO and local control of the pulmonary circulation.* American Journal of Physiology-Heart and Circulatory Physiology, 1996. **271**(6): p. H2717-H2722.
24. Iadecola, C. and M. Nedergaard, *Glial regulation of the cerebral microvasculature.* Nature neuroscience, 2007. **10**(11): p. 1369.
25. Kleinfeld, D., et al., *A guide to delineate the logic of neurovascular signaling in the brain.* Frontiers in neuroenergetics, 2011. **3**: p. 1.
26. Girouard, H. and C. Iadecola, *Neurovascular coupling in the normal brain and in hypertension, stroke, and Alzheimer disease.* Journal of applied physiology, 2006. **100**(1): p. 328-335.
27. Devor, A., et al., *"Overshoot" of O2 is required to maintain baseline tissue oxygenation at locations distal to blood vessels.* Journal of Neuroscience, 2011. **31**(38): p. 13676-13681.
28. Lecoq, J., et al., *Simultaneous two-photon imaging of oxygen and blood flow in deep cerebral vessels.* Nature medicine, 2011. **17**(7): p. 893.
29. Parpaleix, A., Y.G. Houssen, and S. Charpak, *Imaging local neuronal activity by monitoring PO 2 transients in capillaries.* Nature medicine, 2013. **19**(2): p. 241.
30. Wei, H.S., et al., *Erythrocytes are oxygen-sensing regulators of the cerebral microcirculation.* Neuron, 2016. **91**(4): p. 851-862.
31. Bekar, L., et al., *Adenosine is crucial for deep brain stimulation–mediated attenuation of tremor.* Nature medicine, 2008. **14**(1): p. 75.
32. Ding, F., et al., *α1-Adrenergic receptors mediate coordinated Ca2+ signaling of cortical astrocytes in awake, behaving mice.* Cell calcium, 2013. **54**(6): p. 387-394.
33. Wang, X., et al., *Astrocytic Ca 2+ signaling evoked by sensory stimulation in vivo.* Nature neuroscience, 2006. **9**(6): p. 816.
34. Xie, L., et al., *Sleep drives metabolite clearance from the adult brain.* science, 2013. **342**(6156): p. 373-377.
35. Bekar, L.K., H.S. Wei, and M. Nedergaard, *The locus coeruleus-norepinephrine network optimizes coupling of cerebral blood volume with oxygen demand.* Journal of Cerebral Blood Flow & Metabolism, 2012. **32**(12): p. 2135-2145.
36. Duffy, D.C., et al., *Rapid prototyping of microfluidic systems in poly (dimethylsiloxane).* Analytical chemistry, 1998. **70**(23): p. 4974-4984.
37. Wan, J., A.M. Forsyth, and H.A. Stone, *Red blood cell dynamics: from cell deformation to ATP release.* Integrative Biology, 2011. **3**(10): p. 972-981.
38. Frostig, R.D., et al., *Cortical functional architecture and local coupling between neuronal activity and the microcirculation revealed by in vivo high-resolution optical imaging of intrinsic signals.* Proceedings of the National Academy of Sciences, 1990. **87**(16): p. 6082-6086.
39. Takano, T., et al., *Astrocyte-mediated control of cerebral blood flow.* Nature neuroscience, 2006. **9**(2): p. 260.
40. Kim, T.N., et al., *Line-scanning particle image velocimetry: an optical approach for quantifying a wide range of blood flow speeds in live animals.* PloS one, 2012. **7**(6): p. e38590.
41. Hall, C.N., et al., *Capillary pericytes regulate cerebral blood flow in health and disease.* Nature, 2014. **508**(7494): p. 55.
42. Abkarian, M., M. Faivre, and H.A. Stone, *High-speed microfluidic differential manometer for cellular-scale hydrodynamics.* Proceedings of the National Academy of Sciences, 2006. **103**(3): p. 538-542.
43. Cinar, E., et al., *Piezo1 regulates mechanotransductive release of ATP from human RBCs.* Proceedings of the National Academy of Sciences, 2015. **112**(38): p. 11783-11788.

44. Chaigneau, E., et al., *Two-photon imaging of capillary blood flow in olfactory bulb glomeruli.* Proceedings of the National Academy of Sciences, 2003. **100**(22): p. 13081-13086.
45. Jaeger, M., M. Soehle, and J. Meixensberger, *Brain tissue oxygen (P ti O 2): a clinical comparison of two monitoring devices*, in *Intracranial Pressure and Brain Monitoring XII.* 2005, Springer. p. 79-81.
46. Zhou, S., et al., *Oxygen tension–mediated erythrocyte membrane interactions regulate cerebral capillary hyperemia.* Science Advances, 2019. **5**(5): p. eaaw4466.
47. Raichle, M.E., *Behind the scenes of functional brain imaging: a historical and physiological perspective.* Proceedings of the National Academy of Sciences, 1998. **95**(3): p. 765-772.
48. Vanzetta, I. and A. Grinvald, *Increased cortical oxidative metabolism due to sensory stimulation: implications for functional brain imaging.* Science, 1999. **286**(5444): p. 1555-1558.
49. I. Messana, et al., *Human erythrocyte metabolism is modulated by the O2-linked transition of hemoglobin.* FEBS Lett., , 1996. **390**: p. 25-28.
50. Lewis IA, et al., *Role of band 3 in regulating metabolic flux of red blood cells.* Proc Natl Acad Sci U S A. , 2009. **106**: p. 18515-20.
51. Stefanovic M, et al., *Oxygen regulates the band 3-ankyrin bridge in the human erythrocyte membrane.* Biochem J. , 2013. **449**: p. 143-50.
52. Sega MF, et al., *Fluorescence assay of the interaction between hemoglobin and the cytoplasmic domain of erythrocyte membrane band 3.* Blood Cells Mol Dis. , 2015. **55**: p. 266-71.
53. Chu H, et al., *Characterization of the deoxyhemoglobin binding site on human erythrocyte band 3: implications for O2 regulation of erythrocyte properties.* Blood, 2008. **111**: p. 932-8.
54. Sega MF, et al., *Interaction of deoxyhemoglobin with the cytoplasmic domain of murine erythrocyte band 3.* Biochemistry., 2012. **51**: p. 3264-72.
55. Zhang D, et al., *Crystallographic structure and functional interpretation of the cytoplasmic domain of erythrocyte membrane band 3.* Blood. , 2000. **96**: p. 2925-33.
56. Walder JA, et al., *The interaction of hemoglobin with the cytoplasmic domain of band 3 of the human erythrocyte membrane.* J Biol Chem. , 1984. **259**: p. 10238-46.
57. Kimura, H., et al., *Circulation of red blood cells having high levels of 2, 3-bisphosphoglycerate protects rat brain from ischemic metabolic changes during hemodilution.* Stroke, 1995. **26**(8): p. 1431-1437.
58. Coste, B., et al., *Piezo1 and Piezo2 are essential components of distinct mechanically activated cation channels.* Science, 2010. **330**(6000): p. 55-60.
59. Bunn, H.F. and R.W. Briehl, *The interaction of 2, 3-diphosphoglycerate with various human hemoglobins.* The Journal of clinical investigation, 1970. **49**(6): p. 1088-1095.
60. Zappulla, D., *Environmental stress, erythrocyte dysfunctions, inflammation, and the metabolic syndrome: adaptations to CO2 increases?* Journal of the cardiometabolic syndrome, 2008. **3**(1): p. 30-34.
61. Brewer, G.J., *2, 3-DPG and erythrocyte oxygen affinity.* Annual review of medicine, 1974. **25**(1): p. 29-38.
62. Bordin, L., et al., *Functional link between phosphorylation state of membrane proteins and morphological changes of human erythrocytes.* Biochemical and biophysical research communications, 1995. **213**(1): p. 249-257.
63. Sega, M.F., et al., *Interaction of deoxyhemoglobin with the cytoplasmic domain of murine erythrocyte band 3.* Biochemistry, 2012. **51**(15): p. 3264-3272.
64. Wei, H.S., et al., *Erythrocytes Are Oxygen-Sensing Regulators of the Cerebral Microcirculation.* Neuron, 2016. **91**(4): p. 851-862.

65. Hall, C.N., et al., *Capillary pericytes regulate cerebral blood flow in health and disease.* Nature (London, U. K.), 2014. **508**(Copyright (C) 2017 American Chemical Society (ACS). All Rights Reserved.): p. 55-60.
66. Ho, J., W.J. Sibbald, and I.H. Chin-Yee, *Effects of storage on efficacy of red cell transfusion: when is it not safe?* Critical care medicine, 2003. **31**(12): p. S687-S697.
67. Schmid-Schönbein, H. and R. Wells, *Fluid drop-like transition of erythrocytes under shear.* Science, 1969. **165**(3890): p. 288-291.
68. Vague, P. and I. Juhan, *Red cell deformability, platelet aggregation, and insulin action.* Diabetes, 1983. **32**(Supplement 2): p. 88-91.
69. van der Heyde, H.C., et al., *A unified hypothesis for the genesis of cerebral malaria: sequestration, inflammation and hemostasis leading to microcirculatory dysfunction.* Trends in parasitology, 2006. **22**(11): p. 503-508.
70. Fischer, D.J., et al., *Determination of erythrocyte deformability and its correlation to cellular ATP release using microbore tubing with diameters that approximate resistance vessels in vivo.* Analyst, 2003. **128**(9): p. 1163-1168.
71. Price, A.K., et al., *Deformation-induced release of ATP from erythrocytes in a poly (dimethylsiloxane)-based microchip with channels that mimic resistance vessels.* Analytical chemistry, 2004. **76**(16): p. 4849-4855.
72. Price, A.K., R.S. Martin, and D.M. Spence, *Monitoring erythrocytes in a microchip channel that narrows uniformly: Towards an improved microfluidic-based mimic of the microcirculation.* Journal of Chromatography A, 2006. **1111**(2): p. 220-227.
73. Sprung, R., R. Sprague, and D. Spence, *Determination of ATP release from erythrocytes using microbore tubing as a model of resistance vessels in vivo.* Analytical chemistry, 2002. **74**(10): p. 2274-2278.
74. Janigro, D., et al., *Physiological properties of ATP-activated cation channels in rat brain microvascular endothelial cells.* American Journal of Physiology-Heart and Circulatory Physiology, 1996. **270**(4): p. H1423-H1434.
75. Sprague, R.S., A.H. Stephenson, and M.L. Ellsworth, *Red not dead: signaling in and from erythrocytes.* Trends in Endocrinology & Metabolism, 2007. **18**(9): p. 350-355.
76. Sprague, R.S., et al., *Deformation-induced ATP release from red blood cells requires CFTR activity.* American Journal of Physiology-Heart and Circulatory Physiology, 1998. **275**(5): p. H1726-H1732.
77. Subasinghe, W. and D.M. Spence, *Simultaneous determination of cell aging and ATP release from erythrocytes and its implications in type 2 diabetes.* Analytica chimica acta, 2008. **618**(2): p. 227-233.
78. Moehlenbrock, M.J., A.K. Price, and R.S. Martin, *Use of microchip-based hydrodynamic focusing to measure the deformation-induced release of ATP from erythrocytes.* Analyst, 2006. **131**(8): p. 930-937.
79. Gov, N. and S. Safran, *Red blood cell membrane fluctuations and shape controlled by ATP-induced cytoskeletal defects.* Biophysical journal, 2005. **88**(3): p. 1859-1874.
80. Locovei, S., L. Bao, and G. Dahl, *Pannexin 1 in erythrocytes: function without a gap.* Proceedings of the National Academy of Sciences, 2006. **103**(20): p. 7655-7659.
81. Coste, B., et al., *Piezo proteins are pore-forming subunits of mechanically activated channels.* Nature, 2012. **483**(7388): p. 176.
82. Gottlieb, P.A. and F. Sachs, *Piezo1: properties of a cation selective mechanical channel.* Channels, 2012. **6**(4): p. 214-219.
83. Ranade, S.S., et al., *Piezo1, a mechanically activated ion channel, is required for vascular development in mice.* Proceedings of the National Academy of Sciences, 2014. **111**(28): p. 10347-10352.
84. Li, J., et al., *Piezo1 integration of vascular architecture with physiological force.* Nature, 2014. **515**(7526): p. 279.

85. Pathak, M.M., et al., *Stretch-activated ion channel Piezo1 directs lineage choice in human neural stem cells.* Proceedings of the National Academy of Sciences, 2014. **111**(45): p. 16148-16153.
86. Zarychanski, R., et al., *Mutations in the mechanotransduction protein PIEZO1 are associated with hereditary xerocytosis.* Blood, 2012: p. blood-2012-04-422253.
87. Bae, C., et al., *Xerocytosis is caused by mutations that alter the kinetics of the mechanosensitive channel PIEZO1.* Proceedings of the National Academy of Sciences, 2013: p. 201219777.
88. Albuisson, J., et al., *Dehydrated hereditary stomatocytosis linked to gain-of-function mutations in mechanically activated PIEZO1 ion channels.* Nature communications, 2013. **4**: p. 1884.
89. Bae, C., F. Sachs, and P.A. Gottlieb, *The mechanosensitive ion channel Piezo1 is inhibited by the peptide GsMTx4.* Biochemistry, 2011. **50**(29): p. 6295-6300.
90. Tangelder, G., et al., *Wall shear rate in arterioles in vivo: least estimates from platelet velocity profiles.* American Journal of Physiology-Heart and Circulatory Physiology, 1988. **254**(6): p. H1059-H1064.
91. Pries, A.R. and T.W. Secomb, *Blood flow in microvascular networks*, in *Microcirculation*. 2008, Elsevier. p. 3-36.
92. Chu, H., et al., *Identification of cytoskeletal elements enclosing the ATP pools that fuel human red blood cell membrane cation pumps.* Proceedings of the National Academy of Sciences, 2012. **109**(31): p. 12794-12799.
93. Hoffman, J.F., A. Dodson, and F. Proverbio, *On the functional use of the membrane compartmentalized pool of ATP by the Na+ and Ca++ pumps in human red blood cell ghosts.* The Journal of general physiology, 2009. **134**(4): p. 351-361.
94. Proverbio, F. and J.F. Hoffman, *Membrane compartmentalized ATP and its preferential use by the Na, K-ATPase of human red cell ghosts.* The Journal of General Physiology, 1977. **69**(5): p. 605.
95. Cahalan, S.M., et al., *Piezo1 links mechanical forces to red blood cell volume.* Elife, 2015. **4**: p. e07370.
96. Silverman, W.R., et al., *The pannexin 1 channel activates the inflammasome in neurons and astrocytes.* Journal of Biological Chemistry, 2009: p. jbc. M109. 004804.
97. Kim, J.-E. and T.-C. Kang, *The P2X7 receptor–pannexin-1 complex decreases muscarinic acetylcholine receptor–mediated seizure susceptibility in mice.* The Journal of clinical investigation, 2011. **121**(5): p. 2037-2047.
98. Poornima, V., et al., *P2X7 receptor–pannexin 1 hemichannel association: effect of extracellular calcium on membrane permeabilization.* Journal of Molecular Neuroscience, 2012. **46**(3): p. 585-594.
99. Chekeni, F.B., et al., *Pannexin 1 channels mediate 'find-me'signal release and membrane permeability during apoptosis.* Nature, 2010. **467**(7317): p. 863.
100. Dahl, G. and R.W. Keane, *Pannexin: from discovery to bedside in 11±4 years?* Brain research, 2012. **1487**: p. 150-159.
101. Qiu, F., et al., *Two non-vesicular ATP release pathways in the mouse erythrocyte membrane.* FEBS letters, 2011. **585**(21): p. 3430-3435.
102. Rabe, A., J. Disser, and E. Frömter, *Cl− channel inhibition by glibenclamide is not specific for the CFTR-type Cl− channel.* Pflügers Archiv, 1995. **429**(5): p. 659-662.
103. Schwiebert, E.M., *ABC transporter-facilitated ATP conductive transport.* American Journal of Physiology-Cell Physiology, 1999. **276**(1): p. C1-C8.
104. Hoffman, J.F., et al., *Tetrodotoxin-sensitive Na+ channels and muscarinic and purinergic receptors identified in human erythroid progenitor cells and red blood cell ghosts.* Proceedings of the National Academy of Sciences, 2004. **101**(33): p. 12370-12374.

105. Abraham, E.H., et al., *Cystic fibrosis transmembrane conductance regulator and adenosine triphosphate.* Science, 1997. **275**(5304): p. 1324-1326.
106. Hoffman, J.F., *ATP compartmentation in human erythrocytes.* Current opinion in hematology, 1997. **4**(2): p. 112-115.
107. Miyamoto, T., et al., *Functional role for Piezo1 in stretch-evoked Ca 2+ influx and ATP release in urothelial cell cultures.* Journal of Biological Chemistry, 2014: p. jbc. M113. 528638.
108. Yamamoto, K., et al., *Visualization of flow-induced ATP release and triggering of Ca2+ waves at caveolae in vascular endothelial cells.* J Cell Sci, 2011. **124**(20): p. 3477-3483.
109. Bogdanova, A., et al., *Calcium in red blood cells—a perilous balance.* International journal of molecular sciences, 2013. **14**(5): p. 9848-9872.
110. Kuhlman, P.A., et al., *A new function for adducin calcium/calmodulin-regulated capping of the barbed ends of actin filaments.* Journal of Biological Chemistry, 1996. **271**(14): p. 7986-7991.
111. Locovei, S., J. Wang, and G. Dahl, *Activation of pannexin 1 channels by ATP through P2Y receptors and by cytoplasmic calcium.* FEBS letters, 2006. **580**(1): p. 239-244.
112. Schatzmann, H., *Dependence on calcium concentration and stoichiometry of the calcium pump in human red cells.* The Journal of physiology, 1973. **235**(2): p. 551-569.
113. Johnson, R.M., *Membrane stress increases cation permeability in red cells.* Biophysical journal, 1994. **67**(5): p. 1876-1881.
114. Larsen, F.L., et al., *Physiological shear stresses enhance the Ca2+ permeability of human erythrocytes.* Nature, 1981. **294**(5842): p. 667.
115. Romero, P.J. and E.A. Romero, *Differences in Ca2+ pumping activity between sub-populations of human red cells.* Cell calcium, 1997. **21**(5): p. 353-358.
116. Carafoli, E., *Calcium pump of the plasma membrane.* Physiological Reviews, 1991. **71**(1): p. 129-153.
117. Gottlieb, P.A., C. Bae, and F. Sachs, *Gating the mechanical channel Piezo1: a comparison between whole-cell and patch recording.* Channels, 2012. **6**(4): p. 282-289.
118. Zhou, S., et al., *Microfluidic assay of the deformability of primitive erythroblasts.* Biomicrofluidics, 2017. **11**(5): p. 054112.
119. McGrath, K.E., et al., *A transient definitive erythroid lineage with unique regulation of the beta-globin locus in the mammalian embryo.* Blood, 2011: p. blood-2010-12-325357.
120. Lucitti, J.L., et al., *Vascular remodeling of the mouse yolk sac requires hemodynamic force.* Development, 2007. **134**(18): p. 3317-3326.
121. Weinstein, B.M., *What guides early embryonic blood vessel formation?* Developmental dynamics: an official publication of the American Association of Anatomists, 1999. **215**(1): p. 2-11.
122. Fraser, S.T., J. Isern, and M.H. Baron, *Maturation and enucleation of primitive erythroblasts during mouse embryogenesis is accompanied by changes in cell-surface antigen expression.* Blood, 2007. **109**(1): p. 343-352.
123. Waugh, R.E., et al., *Development of membrane mechanical function during terminal stages of primitive erythropoiesis in mice.* Experimental hematology, 2013. **41**(4): p. 398-408. e2.
124. Lee, J.C.-M., et al., *Mechanism of protein sorting during erythroblast enucleation: role of cytoskeletal connectivity.* Blood, 2004. **103**(5): p. 1912-1919.
125. Kalfa, T.A., et al., *Rac GTPases regulate the morphology and deformability of the erythrocyte cytoskeleton.* Blood, 2006. **108**(12): p. 3637-3645.
126. Hoover, K.B. and P.J. Bryant, *The genetics of the protein 4.1 family: organizers of the membrane and cytoskeleton.* Current opinion in cell biology, 2000. **12**(2): p. 229-234.
127. Tchernia, G., N. Mohandas, and S. Shohet, *Deficiency of skeletal membrane protein band 4.1 in homozygous hereditary elliptocytosis. Implications for erythrocyte membrane stability.* The Journal of clinical investigation, 1981. **68**(2): p. 454-460.

128. Conboy, J., et al., *Molecular cloning of protein 4.1, a major structural element of the human erythrocyte membrane skeleton.* Proceedings of the National Academy of Sciences, 1986. **83**(24): p. 9512-9516.
129. Conboy, J., et al., *Molecular basis of hereditary elliptocytosis due to protein 4.1 deficiency.* New England Journal of Medicine, 1986. **315**(11): p. 680-685.
130. Takakuwa, Y., et al., *Restoration of normal membrane stability to unstable protein 4.1-deficient erythrocyte membranes by incorporation of purified protein 4.1.* The Journal of clinical investigation, 1986. **78**(1): p. 80-85.
131. Chasis, J.A. and N. Mohandas, *Erythrocyte membrane deformability and stability: two distinct membrane properties that are independently regulated by skeletal protein associations.* The Journal of cell biology, 1986. **103**(2): p. 343-350.
132. Gallagher, P.G., *Hereditary elliptocytosis: spectrin and protein 4.1R.* Seminars in Hematology, 2004. **41**(2): p. 142-164.
133. Mohandas, N., et al., *A technique to detect reduced mechanical stability of red cell membranes: relevance to elliptocytic disorders.* Blood, 1982. **59**(4): p. 768-774.
134. Zhou, R., et al., *Role of erythrocyte deformability during capillary wetting.* Biotechnology and bioengineering, 2006. **93**(2): p. 201-211.
135. Zhou, R. and H.-C. Chang, *Capillary penetration failure of blood suspensions.* Journal of colloid and interface science, 2005. **287**(2): p. 647-656.
136. Palis, J. and A. Koniski, *Analysis of hematopoietic progenitors in the mouse embryo*, in *Developmental Hematopoiesis*. 2005, Springer. p. 289-301.
137. Kingsley, P.D., et al., *Ontogeny of erythroid gene expression.* Blood, 2012: p. blood-2012-04-422394.
138. Shi, Z.-T., et al., *Protein 4.1 R–deficient mice are viable but have erythroid membrane skeleton abnormalities.* The Journal of clinical investigation, 1999. **103**(3): p. 331-340.
139. Harlow, E., D. Lane, and E. Harlow, *Using antibodies: a laboratory manual.* 1999.
140. Chen, K., et al., *Resolving the distinct stages in erythroid differentiation based on dynamic changes in membrane protein expression during erythropoiesis.* Proceedings of the National Academy of Sciences, 2009. **106**(41): p. 17413-17418.
141. Huang, Y.-S., et al., *Circulating primitive erythroblasts establish a functional, protein 4.1 R-dependent cytoskeletal network prior to enucleating.* Scientific reports, 2017. **7**(1): p. 5164.
142. Langille, B.L., *Remodeling of developing and mature arteries: endothelium, smooth muscle, and matrix.* Journal of cardiovascular pharmacology, 1993. **21**: p. S11-7.
143. Salomao, M., et al., *Protein 4.1 R-dependent multiprotein complex: new insights into the structural organization of the red blood cell membrane.* Proceedings of the National Academy of Sciences, 2008. **105**(23): p. 8026-8031.
144. Shotton, D.M., B.E. Burke, and D. Branton, *The molecular structure of human erythrocyte spectrin: biophysical and electron microscopic studies.* Journal of molecular biology, 1979. **131**(2): p. 303-329.
145. Zhu, Q. and R.J. Asaro, *Spectrin folding versus unfolding reactions and RBC membrane stiffness.* Biophysical journal, 2008. **94**(7): p. 2529-2545.
146. An, X., et al., *Shear-response of the spectrin dimer-tetramer equilibrium in the red blood cell membrane.* Journal of Biological Chemistry, 2002. **277**(35): p. 31796-31800.
147. Chasis, J.A., et al., *Membrane assembly and remodeling during reticulocyte maturation.* Blood, 1989. **74**(3): p. 1112-1120.
148. Migliaccio, A.R., *Erythroblast enucleation*. 2010, Haematologica.